UNIVERSITÀ DEGLI STUDI DI TRIESTE

XVIII CICLO DEL DOTTORATO DI RICERCA IN NANOTECNOLOGIE

Graphene-based low dimensional systems: growth processes and characterization

Settore scientifico-disciplinare: FIS/03

DOTTORANDO
Luca OMICIUOLO

COORDINATORE
Prof.ssa Lucia PASQUATO

SUPERVISORE
Prof. Alessandro BARALDI

CO-SUPERVISORE
Dr. Silvano LIZZIT

Anno Accademico 2014 / 2015

Sommario

Negli ultimi dieci anni la comunità scientifica ha mostrato un sempre crescente interesse per lo studio e la funzionalizzazione di sistemi a bassa dimensionalità, grazie alla varietà di proprietà esotiche che tali sistemi hanno saputo esibire. In quest'ambito il materiale che per primo si è imposto all'attenzione scientifica è sicuramente il grafene, un singolo strato di atomi di carbonio disposti secondo una precisa struttura esagonale a nido d'ape perfettamente 2-dimensionale. Fin dal suo primo isolamento nel 2004, ad opera di A. Geim e K. Novoselov che sono in seguito stati insigniti del premio Nobel per tale scoperta, il grafene è stato considerato una sorta di materiale delle meraviglie. Basti pensare, ad esempio, alla sua particolare struttura elettronica che si riflette in proprietà di trasporto elettronico uniche, o ancora alle eccezionali proprietà meccaniche e termiche. L'isolamento del grafene ha inoltre aperto la strada per la scoperta di diverse famiglie di materiali 2-dimensionali, come ad esempio il nitruro di boro esagonale o i dicalcogenuri di metalli di transizione, ognuno con caratteristiche e potenzialità specifiche, tanto da ipotizzare la possibilità di combinare diversi di questi materiali per applicazioni tecnologiche di nuova generazione o, addirittura, per la produzione di nuovi meta-materiali con caratteristiche programmabili.

Questo lavoro di tesi, e più in generale il mio lavoro di ricerca durante il dottorato, si inserisce nell'ambito della ricerca sul grafene e sulle interfacce a bassa dimensionalità. In una prima parte dell'attività di ricerca mi sono concentrato sulla caratterizzazione dei processi di sintesi di grafene su superfici di metalli di transizione e sullo studio dei meccanismi di interazione tra il grafene e il substrato metallico. Ad oggi vi sono infatti ancora diversi problemi aperti a riguardo, che limitano la scalabilità dei processi di sintesi e la produzione su larga scala di grafene di alta qualità strutturale.

Nella seconda parte mi sono invece dedicato allo studio di interfacce grafene/ossido, che rappresentano uno dei tasselli fondamentali per l'integrazione del grafene in dispositivi elettronici di nuova generazione. In particolare mi sono occupato dello sviluppo di un metodo innovativo per la produzione di interfacce grafene/allumina di alta qualità. Il nostro approccio, a differenza dei metodi comunemente utilizzati per la produzione di tali interfacce, non necessita di processi di trasferimento ed etching chimico che spesso introducono difetti ed impurità nel grafene, a scapito delle proprietà di trasporto elettronico. D'altro canto mi sono anche occupato dello studio di processi per il gating

chimico del grafene mediante la formazione di un ossido ultra-sottile al di sotto del reticolo di carbonio e di uno strato di ossigeno chemisorbito all'interfaccia ossido-substrato.

Nell'ultima parte del mio lavoro di ricerca mi sono altresí interessato ad altri materiali 2-dimensionali. Nello specifico mi sono occupato della caratterizzazione del complesso processo di deidrogenizzazione di molecole di coronene adsorbite su una superificie di Ir(111) fino alla produzione di nano-isole di grafene. Lo studio di tale processo dissociativo apre la strada alla possibilità di ottenere nano-isole di grafene funzionalizzate mediante l'incapsulamento di atomi o molecole. Inoltre mi sono dedicato allo studio di una procedura di sintesi per ottenere strati estesi di nitruro di boro esagonale su Ir(111), orientati secondo un unico dominio cristallino.

Infine, parallelamente all'attività di ricerca, sono stato coinvolto nella progettazione e nello sviluppo di una sorgente di cluster selezionati in massa che è attualmente in costruzione presso il laboratorio di Scienza delle Superfici dell'Universtità degli Studi di Trieste. Tale macchina, una volta completata, rappresentarà uno strumento unico nel panorama della ricerca italiana sui cluster. Una volta accoppiata alla sorgente di luce Elettra, fornirà la possibilità di studiare le proprietà dei cluster al variare della loro dimensione con le più moderne tecniche di analisi basate su luce di sincrotrone. L'ultimo capitolo di questo lavoro di tesi è dunque dedicato alla descrizione dell'attività svolta con tale strumento.

Abstract

In the last decade, the scientific community has shown remarkable interest for the characterization and functionalization of low dimensional systems, due to the number of exotic properties that such systems exhibit. Among the 2D family, the most investigated system is certainly graphene, a single layer of carbon atoms arranged in a perfectly 2-dimensional honeycomb hexagonal lattice. Since its first isolation in 2004, by A. Geim and K. Novoselov who were later awarded with the Nobel prize for the discovery, graphene has been considered a sort of wonder material. This is easily justified, for example, by taking into consideration its peculiar electronic structure giving rise to its unique electronic transport properties, or its outstanding mechanical and thermal properties. The isolation of graphene have then paved the way for the synthesis of other 2-dimensional materials, such as hexagonal boron nitride and transition metal dichalcogenides, each with specific characteristics that make them viable for a new-generation of technological applications, or for the production of novel meta-materials with engineered properties.

My research activity during the three years of PhD has focused on graphene and low-dimensional systems. The first part was devoted to the characterization of the growth processes of graphene on transition metal surfaces and to the study of the interaction mechanism between graphene and the metal substrates. In fact, there are still plenty open issues that are limiting the scalability of the growth processes and the large scale synthesis of high structural quality graphene.

The second part is instead focused on the study of graphene/oxide interfaces, which can be seen as a fundamental step towards the integration of graphene in next generation electronic devices. Specifically, I was involved in the development of a novel method for production of graphene/alumina interfaces. Our method does not require the use of etching and transfer processes that are widely used for the production of such interfaces and that can introduce defects and contaminants in the carbon network, with possible detrimental effects on graphene electronic transport properties. Moreover, I was interested in the possibility of chemically gating graphene, through the formation of an ultrathin oxide film underneath graphene and of a chemisorbed oxygen buffer layer at the oxide/metal interface.

The last part of my research activity was dedicated to the investigation of other 2-dimensional materials. In particular, I worked on the characterization

of the complex dehydrogenation path of coronene on Ir(111), up to the formation of well defined graphene nanoflakes. The study of this dissociation process paves the way to the possibility of obtaining functionalized nano-graphene flakes by the encapsulation of atoms or small molecules. Finally, I also studied the possibility to obtain singly oriented large domains of hexagonal boron nitride on Ir(111).

Parallel to the research activity, I was also involved in the design and setup of a mass selected cluster source that is currently under development at the Surface Science Laboratory of the University of Trieste. Such machine, once completed, will represent a unique instrument in the Italian landscape of material's science. Moreover, once coupled with the Elettra light source, it will open unprecedented possibilities for the characterization of cluster properties with a precise control over their size by means of state of the art synchrotron light based experimental techniques. The last chapter of this thesis work is therefore devoted to the description of the activity carried out with such instrument.

Contents

1 Introduction

Graphene (Gr), a two dimensional carbon atoms lattice arranged in a planar honeycomb configuration, has emerged as a revolutionary material in nanotechnology in the last decade. Since its first isolation in 2004 [1], which earned Geim and Novoselov the Nobel Prize in Physics in 2010, Gr has focused the attention of the scientific community, due to a number of exotic properties that make it a unique material. Gr is, in fact, strictly two dimensional[1], has a high crystallographic quality, and is very stable under ambient conditions. In its free-standing form, both the conduction (π) and valence (π^*) bands present a cone-like energy dispersion at the high symmetry points of the first Brillouin zone, namely the Dirac points, which are also the crossing points of the two bands [3, 4]. The Fermi level lies at these crossing points, implying that Gr is as a zero energy-gap material. Close to the Dirac points, the energy dispersion for small values of the $\mathbf{k}$ wavevector is given by $E(\mathbf{k}) = \pm\hbar v_f|\mathbf{k}| = \pm v_f|\mathbf{p}|$, where $\mathbf{p} = \hbar\mathbf{k}$ is the momentum and v_f, which is the linear coefficient, is the Fermi velocity, of the order of c/300, c being the speed of light. According to the special theory of relativity, the energy of a relativistic particle is given by $E = \sqrt{m^2c^4 + c^2|\mathbf{p}|^2}$, which reduces to $E = c|\mathbf{p}|$ for massless particles. So, near the Dirac points, electrons behave like relativistic massless fermions and are described by the Dirac equation instead of the canonical Schrödinger equation, with the only difference that the speed of light is replaced by the Fermi velocity.

Because of the linear dispersion close to the Fermi level, Gr is characterized by an anomalous behavior with respect to standard metals and semiconductors (which normally display a quasi-parabolic dispersion), showing an anomalous quantum Hall effect [5, 6], and balistic charge carrier mobility [7, 8]. In addition, Gr shows excellent thermal conductivity, high thermal stability [9], and outstanding mechanical properties [10]. For all these reasons, Gr is an appealing material for a number of potential applications including touch screens, ultracapacitors [11, 12], spintronic devices [13], fuel cells [14], single-molecule

[1] Apart from a small, long range buckling [2].

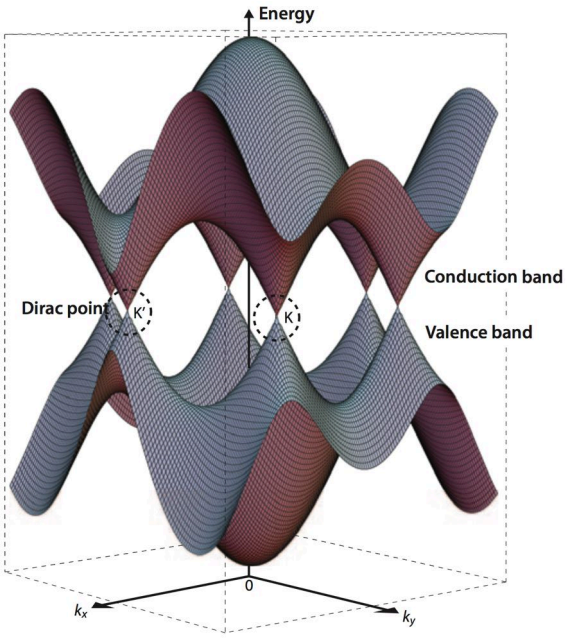

Figure 1.1: Energy bands near the Fermi level in Gr. The conduction and valence bands cross at the Dirac points K and K'. Adapted from [4].

sensors [15], transparent conductive films [16, 17], high-frequency transistors [18, 19], and flexible electronics [20]. Moreover, being chemically inert, Gr can be used to passivate and protect surfaces [21, 22] and is the ideal substrate for nanoparticles and biomolecules deposition and characterization [23, 24, 25, 26].

One of the main bottleneck to the diffusion of Gr-based technology is given by the large scale synthesis of high-quality, large area Gr monolayers. The original method of mechanical exfoliation is, indeed, not suitable for technological applications due to the limited size and non-uniformity of the flakes produced using this approach. Moreover, exfoliation is a complicate and expensive process, and, therefore, not competitive from a technological point of view. High quality Gr layers can be epitaxially grown on transition metal (TM) surfaces by means of Chemical Vapor Deposition (CVD) of carbon-containing molecules [23, 27]. Hydrocarbons are especially suitable for this procedure. State of the art large scale Gr synthesis is industrially achieved by high temperature CVD growth on Copper foils [28], which are then chemically etched in order to obtain free standing Gr flakes.

The other fundamental limit to Gr-based technology arises from the absence of an electronic band gap, which does not make this material suitable

for applications in the field of semiconductors and sensors. To overcome this limitation several strategies were developed. The first solution comes from the interaction between epitaxial Gr and TM substrates, which, in some cases, can cause the opening of an energy gap at the Fermi level [23, 27]. However, with this approach the energy gap, besides being hardly controllable, is not an intrinsic properties of the Gr layer: as soon as the interaction with the substrate changes the energy gap evolves as well. Functionalization of Gr with light atoms, like hydrogen, has also proved successful in this respect [29]. An energy gap can be also obtained introducing substitutional impurities in the carbon lattice, such as Boron and Nitrogen [23, 30, 31], which induce a tunable doping in Gr. Another fascinating alternative to induce a band gap in Gr is provided by Gr nanoribbons. Due to the loss of translational symmetry, Gr nanoribbons exhibit a band gap as a function of their dimension and termination [32, 33, 34]. However, the energy gap in nanoribbons is limited to few hundreds of meV.

My doctoral research activity was primarily focused on the growth and characterization of Gr-based low dimensional interfaces. The first part of this PhD thesis will be devoted to the characterization of the growth mechanism and properties of epitaxial Gr on TM surfaces. In fact, the details of CVD Gr growth on TM surfaces are not yet fully understood at the atomic level. Little is known about the atomistic processes involved in the conversion of the initial hydrocarbon feedstock into carbon for graphene growth. To this purpose, we performed a combined experimental and theoretical experiment aimed to identify all the intermediate reactions steps of the complicated chemical reaction occurring at the Ir(111) surface during thermal decomposition of ethylene, up to Gr formation. Fast and high-resolution C 1s photoemission spectra were acquired as a function of the temperature, following the thermal decomposition of ethylene on Ir(111). The correct assignment of the multiple components observed in the photoemission spectra was achieved by comparing the results of our experiments to those obtained by collaborating groups of theoretician at King's College London, Imperial College London, and University College London. With this approach we were able to reconstruct the complete dissociation path from adsorbed ethylene to atomic C formation and, eventually, Gr.

Another important part of my research activity was aimed to the characterization of Gr interaction with TM substrates. It is well known that, because of the lattice mismatch with the substrate, Gr can form large periodicity superstructures, called moiré pattern [27, 35, 36]. Moreover, the interaction with the substrate can cause corrugations, with weakly interacting regions of Gr far

from the surface, and strongly interacting regions close to the surface [23, 37]. To investigate both the chemical and geometrical contribution to Gr-substrate interaction, and therefore Gr corrugation, we grew Gr on two different TM substrates, Ir(111) and Ru(0001), on which Gr is known to be, on average, weakly [38] and strongly [39] interacting respectively. Subsequently, we intercalated a monolayer of different TMs below Gr, in order to change the surface chemical composition while preserving its geometry [2]. In this way we were able to probe independently the effect of the chemical and geometrical configuration of the substrate on Gr corrugation. Our experimental findings were complemented by a set of theoretical simulations carried by the group of Prof. D. Alfé at the University College London.

The second part of this thesis work is aimed to explore the coupling of Gr with other materials for device integration. In particular we focused our attention on Gr-oxide interfaces, which are fundamental for the development of new electronics, such as Gr-based transistors [18, 40]. The commonly exploited method to produce such interfaces, *i.e.* CVD growth on TM substrates, like Copper, and subsequent transfer onto insulating materials, come with a series of issues, and often results in defective Gr layers, with detrimental effect on the electronic transport properties. Here I describe an alternative method we have developed for the direct synthesis of high quality Gr-alumina[3] interfaces. Our method, which consists of CVD growth on a bimetallic surface alloy and subsequent selective oxidation of the interfacial Al atoms below Gr, could open new possibilities for the Gr-alumina interfaces integration in new generation electronic devices.

A method for the chemical gating of epitaxial Gr is also presented. Starting from previous findings of our research group [41], we show how it is possible to achieve a controllable gating of epitaxial Gr, grown on Ir(111), by exploiting the electrostatic polarization of ultrathin SiO_2 layers synthesized below it. Our system behaves like a gated plane capacitor with the in situ grown SiO_2 layer acting as a dielectric spacer, whose high capacity allows the Fermi level of graphene to be shifted by a few hundreds of meV. We show how the hole doping can be finely tuned by controlling the amount of oxygen in the interfacial buffer layer, as well as by adjusting the thickness of the oxide layer.

The first isolation of Gr, opened the route to several other 2D systems. As outlined before, Gr nanoribbons and nanoislands have proved to be an effective method for overcoming some of Gr limitations, like the absence of an energy

[2] The intercalated TMs were observed to form, in our case, an epitaxial layer with the same geometry of the substrate.

[3] Being aluminum oxide, or alumina, a widely used dielectric in electronics.

band gap. On the other hand, other Gr-like 2D materials were synthesized, starting from bulk materials which exhibit a strong in-plane covalent bond and a weak out-of-plane van der Waals interaction between atomic planes. The two most famous example in this regard are hexagonal Boron Nitride (*h*-BN) and Molybdenum Disulfide (MoS_2). The former has the same lattice configuration of Gr, but the C atoms in the unit cell are replaced with Boron and Nitrogen atoms respectively. The latter, instead, consist of three layer planar honeycomb configuration, with the two Sulfur atoms occupying the outer layers. Most importantly, *h*-BN is wide gap insulator, while MoS_2 is a semiconductor. These materials, together with Gr, are the ideal bricks to construct stacked heterostrcuctures with tailored properties [42].

In this respect part of my research activity was devoted to the investigation of other Gr-related 2D materials. Two different results are presented in the third part of this work. The first result concerns the characterization of a single domain *h*-BN monolayer grown on Ir(111) by means of high temperature borazine ($B_3N_3H_6$) CVD. The second experiment, on the other hand, is a combined experimental and theoretical study of the temperature induced dehydrogenation mechanism of coronene ($C_{24}H_{12}$) on Ir(111). Starting from absorbed molecules on the surface we studied the full reaction pathway up to the formation of dome-shaped Gr nanoislands which, at higher temperature, eventually nucleate to form a single Gr layer. A detailed understanding of this complex reaction path, involving molecular lifting, twisting, and curling, was achieved by comparing the experimental findings to a complete set of theoretical simulations. The importance of this study relies both on the fact that this is a novel reaction mechanism and on the possibility of creating controlled arrangements of Gr nanoislands and functionalizing them by encapsulating adatoms below the C domes.

The final part of this thesis is devoted to a parallel activity carried out during the three years of PhD, *i.e.* the set up of a mass selected cluster source. Metallic clusters have earned a great interest from the scientific community during the last years because, when reduced to few tens of atoms, the electronic and geometrical properties of matter dramatically depend on the precise number of atoms. The best example in this respect is given by Au nanoclusters which are, by far, the most investigated in the cluster family [43, 44, 45]. A precise control over the number of atoms, or, in other words, of the cluster mass of a specific element of the periodic table is therefore needed in order to properly characterize the cluster properties using synchrotron radiation-based spectroscopic techniques which provide space-integrated information. On the other

hand, epitaxial Gr, as well as others 2D materials like *h*-BN, on TM surfaces represent the ideal substrate for cluster growth and characterization due to the chemical passivity and, is some case, of the moiré corrugation, which could be used as a template for patterned growth. For this reason I actively contributed to the design and development of a mass selected cluster source, based on charge to mass ratio discrimination of charged clusters, which is described in detail in the final chapter of this thesis.

Bibliography

[1] K. S. Novoselov, A. K. Geim, S. V. Morozov, D. Jiang, Y. Zhang, S. V. Dubonos, , I. V. Grigorieva, and A. A. Firsov. Electric field effect in atomically thin carbon films. *Science*, **306**(5696):666–669, 2004.

[2] A. Fasolino, J. H. Los, and M. I. Katsnelson. Intrinsic ripples in graphene. *Nature Materials*, **6**(11):858–861, 2007.

[3] K. S. Novoselov, A. K. Geim, S. V. Morozov, D. Jiang, M. I. Katsnelson, I. V. Grigorieva, S. V. Dubonos, and A. A. Firsov. Two-dimensional gas of massless Dirac fermions in graphene. *Nature*, **438**(7065):197–200, 2005.

[4] T. Ando. The electronic properties of graphene and carbon nanotubes. *NPG Asia Materials*, **1**(1):17–21, 2009.

[5] V. P. Gusynin and S. G. Sharapov. Unconventional integer quantum Hall effect in graphene. *Physical Review Letters*, **95**(14):146801, 2005.

[6] Y. Zhang, Y. W. Tan, H. L. Stormer, and Ph. Kim. Experimental observation of the quantum Hall effect and Berry's phase in graphene. *Nature*, **438**(7065):201–204, 2005.

[7] A. S. Mayorov, R. V. Gorbachev, S. V. Morozov, L. Britnell, R. Jalil, L. A. Ponomarenko, P. Blake, K. S. Novoselov, K. Watanabe, T. Taniguchi, and A. K. Geim. Micrometer-scale ballistic transport in encapsulated graphene at room temperature. *Nano Letters*, **11**(6):2396–2399, 2011.

[8] X. Du, I. Skachko, A. Barker, and E. Y. Andrei. Approaching ballistic transport in suspended graphene. *Nature Nanotechnology*, **3**(8):491–495, 2008.

[9] A. A. Balandin, S. Ghosh, W. Bao, I. Calizo, D. Teweldebrhan, F. Miao, and C. N. Lau. Superior thermal conductivity of single-layer graphene. *Nano Letters*, **8**(3):902–907, 2008.

[10] C. Lee, X. Wei, J. W. Kysar, and J. Hone. Measurement of the elastic properties and intrinsic strength of monolayer graphene. *Science*, **321**(5887):385–388, 2008.

[11] M. Zhi, C. Xiang, J. Li, M. Li, and N. Wu. Nanostructured carbon–metal oxide composite electrodes for supercapacitors: a review. *Nanoscale*, **5**(1):72–88, 2013.

[12] J. J. Yoo, K. Balakrishnan, J. Huang, V. Meunier, B. G. Sumpter, A. Srivastava, M. Conway, A. L. Mohana Reddy, J. Yu, R. Vajtai, and M. A. Pulickel. Ultrathin planar graphene supercapacitors. *Nano Letters*, **11**(4):1423–1427, 2011.

[13] W. Han, R. K. Kawakami, M. Gmitra, and J. Fabian. Graphene spintronics. *Nature Nanotechnology*, **9**(10):794–807, 2014.

[14] L. Qu, Y. Liu, J. B. Baek, and L. Dai. Nitrogen-doped graphene as efficient metal-free electrocatalyst for oxygen reduction in fuel cells. *ACS Nano*, **4**(3):1321–1326, 2010.

[15] F. Schedin, A. K. Geim, S. V. Morozov, E. W. Hill, P. Blake, M. I. Katsnelson, and K. S. Novoselov. Detection of individual gas molecules adsorbed on graphene. *Nature Materials*, **6**(9):652–655, 2007.

[16] X. Li, Y. Zhu, W. Cai, M. Borysiak, B. Han, D. Chen, R. D. Piner, L. Colombo, and R. S. Ruoff. Transfer of large-area graphene films for high-performance transparent conductive electrodes. *Nano Letters*, **9**(12):4359–4363, 2009.

[17] S. Bae, H. Kim, Y. Lee, X. Xu, J. S. Park, Y. Zheng, J. Balakrishnan, T. Lei, H. R. Kim, Y. II Song, Y. J. Kim, K. S. Kim, B. Ozyilmaz, J. H. Ahn, B. H. Hong, and S. Iijima. Roll-to-roll production of 30-inch graphene films for transparent electrodes. *Nature Nanotechnology*, **5**(8):574–578, 2010.

[18] F. Schwierz. Graphene transistors. *Nature Nanotechnology*, **5**(7):487–496, 2010.

[19] Y. Wu, Y. M. Lin, A. A. Bol, K. A. Jenkins, F. Xia, D. B. Farmer, Y. Zhu, and Ph. Avouris. High-frequency, scaled graphene transistors on diamond-like carbon. *Nature*, **472**(7341):74–78, 2011.

[20] K. S. Kim, Y. Zhao, H. Jang, S. Y. Lee, J. M. Kim, K. S. Kim, J. H. Ahn, Ph. Kim, J. Y. Choi, and B. H. Hong. Large-scale pattern growth of graphene films for stretchable transparent electrodes. *Nature*, **457**(7230):706–710, 2009.

[21] M. Topsakal, H. Şahin, and S. Ciraci. Graphene coatings: An efficient protection from oxidation. *Physical Review B*, **85**(15):155445, 2012.

[22] Y. Zhao, Y. Xie, Y. Y. Hui, L. Tang, W. Jie, Y. Jiang, L. Xu, S. P. Lau, and Y. Chai. Highly impermeable and transparent graphene as an ultra-

thin protection barrier for Ag thin films. *Journal of Materials Chemistry C*, **1**(32):4956–4961, 2013.

[23] M. Batzill. The surface science of graphene: Metal interfaces, CVD synthesis, nanoribbons, chemical modifications, and defects. *Surface Science Reports*, **67**(3):83–115, 2012.

[24] S. N'Diaye, A. T. Bleikamp, P. J. Feibelman, and T. Michely. Two-dimensional Ir cluster lattice on a graphene moiré on Ir(111). *Physical Review Letters*, **97**(21):215501, 2006.

[25] S. Myung, A. Solanki, C. Kim, J. Park, K. S. Kim, and K. B. Lee. Graphene-encapsulated nanoparticle-based biosensor for the selective detection of cancer biomarkers. *Advanced Materials*, **23**(19):2221–2225, 2011.

[26] Y. Wang, Z. Li, J. Wang, J. Li, and Y. Lin. Graphene and graphene oxide: biofunctionalization and applications in biotechnology. *Trends in Biotechnology*, **29**(5):205–212, 2011.

[27] J. Wintterlin and M. L. Bocquet. Graphene on metal surfaces. *Surface Science*, **603**(10):1841–1852, 2009.

[28] X. Li, W. Cai, J. An, S. Kim, J. Nah, D. Yang, R. Piner, A. Velamakanni, I. Jung, E. Tutuc, S. K. Banerjee, L. Colombo, and R. S. Ruoff. Large-area synthesis of high-quality and uniform graphene films on copper foils. *Science*, **324**(5932):1312–1314, 2009.

[29] R. Balog, B. Jørgensen, L. Nilsson, M. Andersen, E. Rienks, M. Bianchi, M. Fanetti, E. Lægsgaard, A. Baraldi, S. Lizzit, Z. Sljivancanin, F. Besenbacher, B. Hammer, T. G. Pedersen, Ph. Hofmann, and L. Hornekær. Bandgap opening in graphene induced by patterned hydrogen adsorption. *Nature Materials*, **9**(4):315–319, 2010.

[30] L. S. Panchakarla, K. S. Subrahmanyam, S. K. Saha, A. Govindaraj, H. R. Krishnamurthy, U. V. Waghmare, and C. N. R. Rao. Synthesis, structure, and properties of boron-and nitrogen-doped graphene. *Advanced Materials*, **21**(46):4726–4730, 2009.

[31] D. Wei, Y. Liu, Y. Wang, H. Zhang, L. Huang, and G. Yu. Synthesis of N-doped graphene by chemical vapor deposition and its electrical properties. *Nano Letters*, **9**(5):1752–1758, 2009.

[32] M. Y. Han, B. Özyilmaz, Y. Zhang, and Ph. Kim. Energy band-gap engineering of graphene nanoribbons. *Physical Review Letters*, **98**(20):206805, 2007.

[33] L. Yang, C. H. Park, Y. W. Son, M. L. Cohen, and S. G. Louie. Quasiparticle energies and band gaps in graphene nanoribbons. *Physical Review Letters*, **99**(18):186801, 2007.

[34] Y. W. Son, M. L. Cohen, and S. G. Louie. Energy gaps in graphene nanoribbons. *Physical Review Letters*, **97**(21):216803, 2006.

[35] P. W. Sutter, J. I. Flege, and E. A. Sutter. Epitaxial graphene on ruthenium. *Nature Materials*, **7**(5):406–411, 2008.

[36] C. Busse, P. Lazić, R. Djemour, J. Coraux, T. Gerber, N. Atodiresei, V. Caciuc, R. Brako, A. T. N'Diaye, S. Blügel, J. Zegenhagen, and T. Michely. Graphene on Ir(111): physisorption with chemical modulation. *Physical Review Letters*, **107**(3):036101, 2011.

[37] A. B. Preobrajenski, M. L. Ng, A. S. Vinogradov, and N. Mårtensson. Controlling graphene corrugation on lattice-mismatched substrates. *Physical Review B*, **78**(7):073401, 2008.

[38] I. Pletikosić, M. Kralj, P. Pervan, R. Brako, J. Coraux, A. T. N'Diaye, C. Busse, and T. Michely. Dirac cones and minigaps for graphene on Ir(111). *Physical Review Letters*, **102**(5):056808, 2009.

[39] P. W. Sutter, J. I. Flege, and E. A. Sutter. Epitaxial graphene on ruthenium. *Nature Materials*, **7**(5):406–411, 2008.

[40] Y. M. Lin, C. Dimitrakopoulos, K. A. Jenkins, D. B. Farmer, H. Y. Chiu, A. Grill, and Ph. Avouris. 100-GHz transistors from wafer-scale epitaxial graphene. *Science*, **327**(5966):662–662, 2010.

[41] S. Lizzit, R. Larciprete, P. Lacovig, M. Dalmiglio, F. Orlando, A. Baraldi, L. Gammelgaard, L. Barreto, M. Bianchi, E. Perkins, and Ph. Hofmann. Transfer-free electrical insulation of epitaxial graphene from its metal substrate. *Nano Letters*, **12**(9):4503–4507, 2012.

[42] A. K. Geim and I. V. Grigorieva. Van der Waals heterostructures. *Nature*, **499**(7459):419–425, 2013.

[43] M. Haruta. Size-and support-dependency in the catalysis of gold. *Catalysis Today*, **36**(1):153–166, 1997.

[44] A. Sanchez, S. Abbet, U. Heiz, W. D. Schneider, H. Häkkinen, R. N. Barnett, and Z. Landman. When gold is not noble: nanoscale gold catalysts. *The Journal of Physical Chemistry A*, **103**(48):9573–9578, 1999.

[45] Z. Y. Li, N. P. Young, M. Di Vece, S. Palomba, R. E. Palmer, A. L. Bleloch, B. C. Curley, R. L. Johnston, J. Jiang, and J. Yuan. Three-dimensional atomic-scale structure of size-selected gold nanoclusters. *Nature*, **451**(7174):46–48, 2008.

2 Experimental Techniques and Setup

This chapter is meant to provide a background of the experimental techniques used during my doctoral research activity, along with a brief description of the experimental facilities and instrumentations used to acquire the data presented. All the experiments were performed in Ultra High Vacuum (UHV) conditions, with a base pressure of the order of $10^{-10} - 10^{-11}$mbar. The need for UHV conditions, which are a common framework in surface sciences, comes from two different motivations. Assuming that the sticking probability of contaminants in a vacuum environment is 1, in a background pressure of $1 \cdot 10^{-6}$ mbar the sample would get completely covered by contaminants in few seconds[1], thus preventing any accurate measurement of the actual surface. Moreover, good pressure conditions are needed when working with low energy electrons[2] based techniques, in order to minimize scattering effects with residual gas molecules. To obtain such vacuum conditions, beside a good pumping systems, a bake out procedure is needed, in order to induce the desorption of water, along with other contaminants, from the inner walls of the vacuum chamber. Before the experiments all the vacuum components (including instrumentations, evaporators, sample holder, etc..) have to be carefully cleaned in vacuum by means of annealing cycles optimized to properly outgass the residual contaminants. Moreover, before each measurement, the samples were cleaned via a suitable cleaning procedure. For the metallic surfaces which I used throughout this work it generally consisted of sputtering cycles, followed by annealing to high temperature and, in some cases, chemical treatments with specific gaseous reactants. In the first part the sample surface is bombarded by a collimated flux of energetic Ar ions in such a way to remove the contaminants from the surface by ion impact, resulting in a rough and disordered surface. In order to restore the surface long range order, thus obtaining large terraces[3], sputtering is followed by annealing cycles to high temperatures. The

[1] According to the Hertz-Knudsen formula [1].
[2] Typically from 40 to 300 eV.
[3] For most metal surfaces, typically hundreds of Å.

data presented in this thesis work were acquired in different UHV chambers, each equipped with standard vacuum instrumentation needed to clean and prepare the samples: a sputtering ion gun, a gas-line used to dose gases in the vacuum chamber and a quadrupole mass spectrometer (QMS) to monitor the residual gas composition.

To fully characterize the systems presented in this work, several different aspects had to be addressed. For example, a complete characterization of the electronic structure of adsorbates, including core levels and valence states, allowed the fine investigation of their chemical interaction with the substrate. On the other hand, energy dispersion measurements near the Fermi level were essential to discriminate between the flat, non dispersing, molecular levels of adsorbates and the band structure of metallic substrates, or for calculating the doping level of graphene-based systems. Moreover, a detailed knowledge of both the local and long range surface order were required to access the structural quality of the systems, and to discriminate between different possible adsorption geometries. Therefore, a variety of different experimental techniques were employed. Core level and valence band photoelectron spectroscopy, together with absorption spectroscopy, and angle resolved photoemission spectroscopy, were used to investigate the chemistry of the systems, by probing their electronic configuration. On the other hand, electron based diffraction and microscopy techniques allowed us to access their geometrical configurations. Finally, due to the complexity of the investigated systems, the experiments were often paralleled by complementary theoretical calculations, particularly Density Functional Theory (DFT) simulations. In the following sections, a brief introduction to the main experimental techniques used in this work is given.

2.1 Photoelectron Spectroscopy

The photoelectric effect takes place when a photon with a sufficient energy interacts with matter, causing the removal of one electron from an electronic state, such as an atomic core level, a molecular orbital or a band, and its promotion above the vacuum level. The process, firstly observed at the end of the 19^{th} century, was only rationalized in 1905 by Albert Einstein by postulating the quantum nature of the electromagnetic field, for which he was awarded with the Nobel Prize 16 years later. According to Einstein hypothesis, light is composed of discrete *quanta*, or photons. When a photon interact with an electron, it can transfer its energy to the electron itself, so that, if the energy is greater than the work function of the material, the electron may leave the surface in a process

called photoemission. This process can be described with a three step model [1] consisting of:

1. optical excitation
2. migration to the surface
3. transition to the vacuum level[4]

Given a N electrons atom, the photemission process due to the absorption of photon with energy $h\nu$ can be described as follow:

$$\Psi^i(N), E^i(N) \rightarrow \Psi^f(N-1) + \Phi(k), E^f(N-1) + E_k \tag{2.1}$$

where $\Psi^i(N)$ and $\Psi^f(N-1)$ are the initial and final states with N and $N-1$ atoms respectively, $\Phi(k)$ is the wave function of the free photoelectron, $E^i(N)$ and $E^f(N-1)$ are the energy eigenvalues of the the initial and final states, and E_k is the kinetic energy of the photoelectron. Imposing the total energy conservation implies that

$$E^i(N) + h\nu = E^f(N-1) + E_k \tag{2.2}$$

The binding energy (BE) of the photoemitted electron, referred to the vacuum level, can be expressed as

$$E_b = h\nu - E_k = E^f(N-1) - E^i(N) \tag{2.3}$$

implying that the BE is given by the difference between the total energy of the final and initial states. The zeroth order approximation, *i.e.* the Koopmans' theorem, leads to

$$E_b = -\epsilon_k \tag{2.4}$$

where ϵ_k represents the Hartree-Fock eigenvalue corresponding to the selected state, *i.e.* the ionization energy. In photoemission experiments, the photoelectron kinetic energy is recorded and then the binding energy is calculated. This requires fixing a proper energy reference. The commonly accepted procedure consists of referencing the binding energy to the Fermi level. Fig. 2.1 illustrates how, since they are grounded together, the Fermi level of the sample and that of the electron analyzer are aligned. Therefore, equation 2.3 reduces to

$$E_b^{FL} = h\nu - E_k^{meas} - \Phi_{sample} + (\Phi_{sample} - \Phi_{analyzer}) = h\nu - E_k^{meas} - \Phi_{analyzer} \tag{2.5}$$

[4] In a more detailed and rigorous approach, the photoemission process is described as a single step quantum mechanism [2, 3].

where E_k^{meas} is the kinetic energy measured by the analyzer, E_b^{FL} is the binding energy referenced to the Fermi level, and Φ_{sample} and $\Phi_{analyzer}$ are the work function of the sample and of the analyzer respectively. Therefore, in order to properly reference the binding energy scale to the Fermi level, it is sufficient to know the the work function of the electron analyzer.

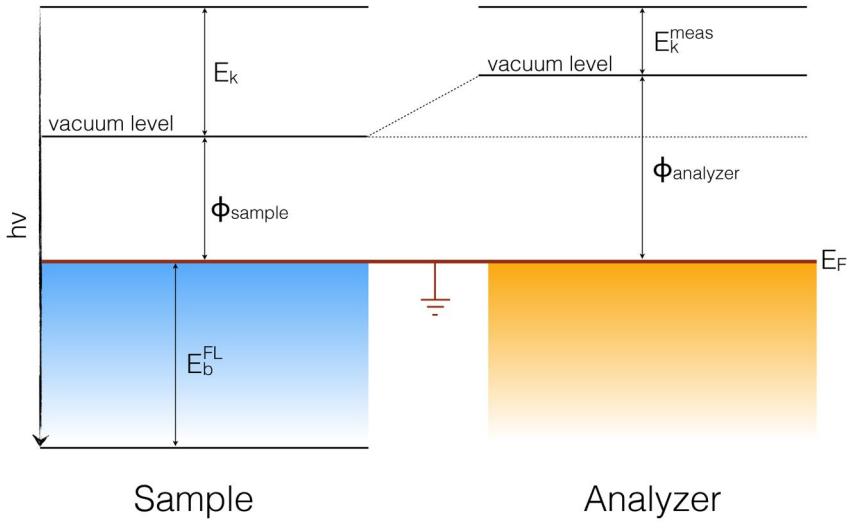

Figure 2.1: Energy diagram of a typical photoemission experiment.

Since E_b^{FL} is characteristic of each element, photoelectron spectroscopy is an ideal tool for the chemical analysis of materials. Different chemical bonds are reflected in the so called chemical shifts [4], *i.e.* the deviation of the photolectron binding energy from the free atom case. These core level shifts (CLS) lead to the possible identifications of atoms or molecules in different chemical or structural environments. For instance, these shifts allow to discriminate between non equivalent atoms inside a molecule, or, for solid samples, between surface and bulk atoms, due to the different coordination. In the latter case, the specific chemical shifts are referred as surface core level shifts (SCLS).

Another remarkable property of photoelectron spectroscopy, *i.e.* the surface sensitivity, is related to the inelastic mean free path (IMFP) of electrons in solids. As reported in fig. 2.2, the universal curve that is used to describe the IMFP of electrons in metals shows a clear minimum between 50 and 100 eV kinetic energy. More specifically, between about 20 to 500 eV, the IMFP is less than 10 Å, so that only the photoelectrons emitted from the first few layers of the sample will escape the surface, the others being screened by the topmost layers. At lower energies, electron-hole pair formation and electron-

phonon scattering become more important, and the distance between inelastic collisions increases. At higher energies, instead, the rise of the IMFP is mainly due to a decrease of the cross-section for plasmon excitations.

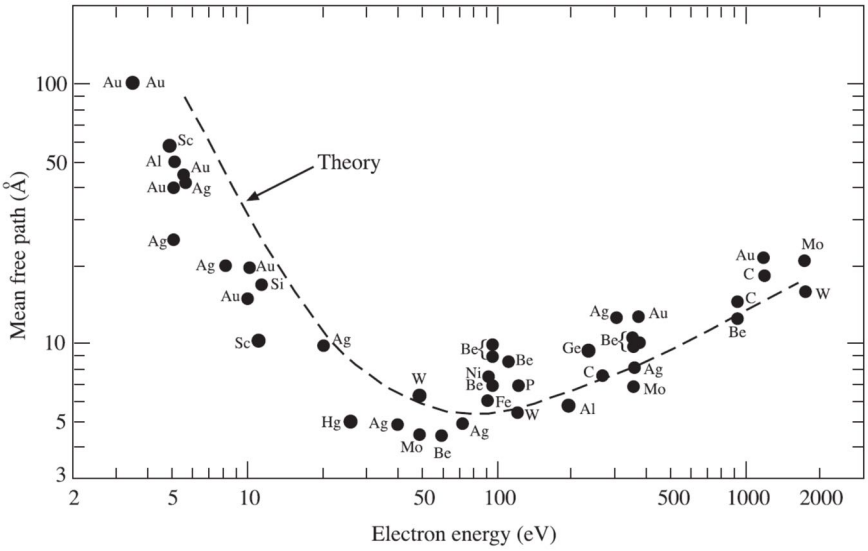

Figure 2.2: Universal curve of electron inelastic mean free path.

From a theoretical point of view, the photoemission process is generally described with a semiclassical approximation, in which the electromagnetic field is treated classically. In a minimal coupling approach, the hamiltonian operator for a single electron of charge $-e$ and mass m in an electromagnetic field, is given by:

$$\hat{H} = \frac{1}{2m}\left(\hat{\mathbf{p}} + \frac{e}{c}\hat{\mathbf{A}}\right)^2 - e\Phi \tag{2.6}$$

where Φ and $\mathbf{A}$ are the electromagnetic scalar and vector potential respectively. By using the Coulomb gauge, *i.e.* $\nabla \cdot \mathbf{A} = 0$, the time evolution of the system can be written as

$$i\hbar\frac{\partial}{\partial t}\Psi(\mathbf{r},t) = \left[\frac{\hat{\mathbf{p}}^2}{2m} - \frac{e}{mc}\hat{\mathbf{A}}\cdot\hat{\mathbf{p}} + \hat{U}\right]\Psi(\mathbf{r},t) \tag{2.7}$$

in which the second order $\hat{\mathbf{A}}^2$ has been neglected, being usually much smaller than the linear one[5], and we have used the fact that, in the Coulomb gauge, the momentum operator and the vector potential commutes, *i.e.* $[\hat{\mathbf{A}}, \hat{\mathbf{p}}] = 0$. In a first order perturbation framework, the Hamiltonian can be split in two:

[5]This is essentially equivalent to assuming a one photon absorption process, and its strictly valid only for the weak field case.

the unperturbed Hamiltonian ($\hat{H}_0$) containing the kinematic term and the inner potential[6], and a perturbative term $\hat{H}'$

$$\hat{H} = \hat{H}_0 + \hat{H}' \tag{2.8}$$

where

$$\hat{H}' = -\frac{e}{mc}\hat{\mathbf{A}} \cdot \hat{\mathbf{p}} \tag{2.9}$$

The time dependent perturbation theory allows us to express the transition rate between the initial state Ψ_i, and the final state Ψ_f via the Fermi golden rule:

$$\frac{d\omega}{dt} \propto \frac{2\pi}{\hbar} |\langle \Psi_f | \hat{H}' | \Psi_i \rangle|^2 \delta(E_f - E_i - h\nu) \tag{2.10}$$

where E_i and E_f are the initial and finale state eigenvalue of the unperturbed Hamiltonian respectively, and $h\nu$ is the photon energy. To account for the finite time scale of real interactions, the Dirac delta should be replaced by the density of state ρ_f in the final state:

$$\frac{d\omega}{dt} \propto \frac{2\pi}{\hbar} |\langle \Psi_f | \hat{H}' | \Psi_i \rangle|^2 \rho_f \tag{2.11}$$

The vector potential can be written as a plane electromagnetic wave with wave vector $\mathbf{k}$, and angular frequency ω:

$$\mathbf{A} = \mathbf{A}_0 e^{i(\mathbf{k}\cdot\mathbf{r} - \omega t)} \tag{2.12}$$

In general, the wavelength of the electromagnetic radiation which induces transitions between different atomic energy levels is much larger than the typical size of an atom. Thus,

$$exp(i\mathbf{k} \cdot \mathbf{r}) = 1 + (i\mathbf{k} \cdot \mathbf{r}) + \frac{1}{2}(i\mathbf{k} \cdot \mathbf{r})^2 + .. \approx 1 \tag{2.13}$$

can be approximated by its first term[7]. With these approximations, it can be demonstrated that the integrated absorption cross-section becomes:

$$\sigma_{fi} = \frac{4\pi^2 e^2}{3\hbar c}\omega |\langle \Psi_f | \mathbf{r} | \Psi_i \rangle|^2 \tag{2.14}$$

Fig 2.3 shows, as an example, the variation of the photoionization cross section for some of the core level analyzed in this thesis work, as a function of the incident photon energy. This figure points out of the main advantages of using synchrotron radiation, *i.e.* the photon energy tunability. Indeed, this offers the possibility to maximize (or minimize) the sensitivity to a specific core level under investigation, by simply tuning the photon energy.

[6] Which accounts for the Coulomb interaction with the nucleus, the Coulomb repulsions between electrons, and spin orbit interaction.

[7] This approach is commonly referred to as the dipole approximation.

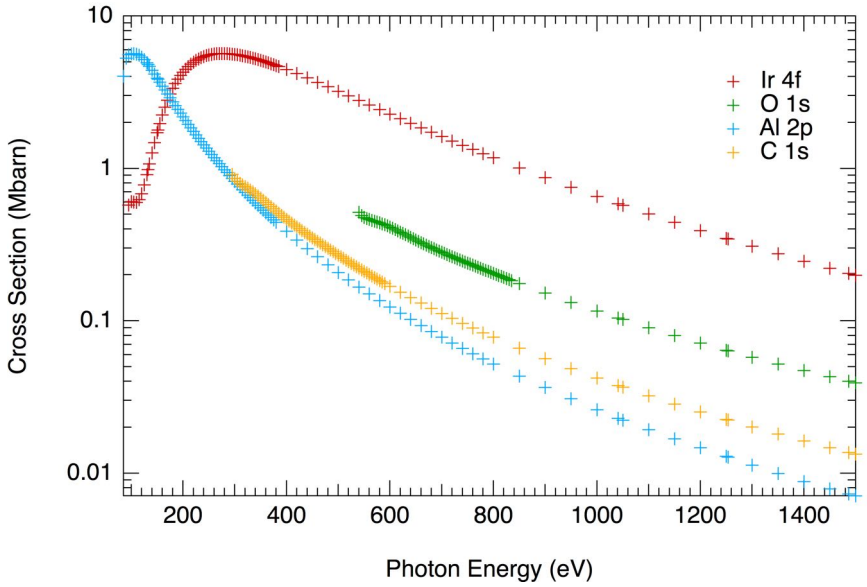

Figure 2.3: Photoemission cross-section for the C 1s, Al 2p, Ir 4f, and O 1s core levels ad a function of the incoming photon energy.

Photoemission experiments can be classified according to the photon energy and, consequently, to the electronic structure region of investigation. Soft X-Rays in the 100-2000 eV range are typically used to probe core levels, and, in this case, photoelectron spectroscopy is usually referred to as X-Ray Photoelectron Spectroscopy (XPS). For valence band measurements, in order to maximize the cross-section, the optimal photon energy range is the ultraviolet (3-100 eV), so that, in this case, we talk about Ultraviolet Photoelectron Spectroscopy (UPS). Moreover, when the UPS spectra are collected as a function of the polar and azimuthal sample angles, which can be mapped to the in plane component of the electron wavevector k_x and k_y, the technique is called Angle Resolved Photoemission Spectroscopy (ARPES), and probes the electron band structure of the sample.

2.1.1 XPS Spectra Line Shape

In order to extract quantitative information and to isolate the single components from XPS spectra, a proper theoretical model to fit the data to is needed. One of the most commonly exploited formalism is the semi-empirical model formulated by Doniach, S. and Šunjić, M. (D-S) [5]. Given the finite core-hole lifetime (τ), and assuming an exponential decay probability for the core-hole relaxation ($\propto exp(-t/\tau)$), the spectral function will have a Lorentzian lineshape, charac-

terized by a Full Width Half Maximum (FWHM) Γ:

$$I_L(E) = \frac{I_0}{\pi} \frac{\Gamma/2}{(E - E_b)^2 + \Gamma^2/4} \tag{2.15}$$

where Γ and τ are related by the Heinsenberg indetermination principle: $\Gamma\tau \geq \hbar$. To account for electron-hole pair excitations at the Fermi level, resulting in a lower kinetic energy of the photoelectron, and, therefore, in an asymmetric tail at high BEs in the photoemission spectra, Doniach and Šunjić developed a modified Lorentzian, in which the asymmetry is introduced through a parameter α:

$$I_{DS}(E) = I_0 \frac{\Gamma_E(1-\alpha)}{[(E - E_b)^2 + \Gamma^2/4]^{(1-\alpha)/2}} \zeta(E) \tag{2.16}$$

where Γ_E is the Euler gamma function, and

$$\zeta(E) = \cos\left[\frac{\pi\alpha}{2} + (1-\alpha)\arctan\left(\frac{E - E_b}{\Gamma/2}\right)\right] \tag{2.17}$$

Besides the Lorentzian broadening, photoemission spectra are also affected by a Gaussian broadening, which basically contains the resolution and the vibrational contributions. The first effect is due to the non perfect monochromaticity of the photon beam and to the limited resolving power of the electron energy analyzer, which pose an upper bound to the overall experimental energy resolution. The vibrational broadening is produced by the excitation of low energy vibrational modes both in the initial and in the final state. Moreover, an inhomogeneous broadening may originate from the presence of unresolved core level shifted components in the spectrum. The Gaussian contribution to the experimentally observed broadening can be expressed as:

$$I_G(E) = \frac{I_0}{\sigma\sqrt{2}} exp\left(-\frac{(E - E_b)^2}{2\sigma^2}\right) \tag{2.18}$$

All the XPS spectra presented in this thesis work were analyzed by the sum of D-S functions convoluted with Gaussians, corresponding to the number of distinct components in the spectra, as described in [6]. The BEs were referenced to the Fermi level, which was measured together with the corresponding core level spectrum. The background was assumed to be either Shirley type or linear, depending on the specific spectrum. For Shirley type background we referred to the formalism described in [7], where the background-subtracted spectrum is iteratively calculated as follows:

$$S_i(E) \propto \int_E^\infty \mathrm{d}E'(I(E') - S_{i-1}(E')) \tag{2.19}$$

where $I(E)$ is the experimental photoemission intensity, $S_i(E)$ is the Shirley net intensity at the *i-th* iterations, and $S_0(E)$ is the initial background choice, which

is set to a constant. The calculation usually converges after 4-5 iterations. The background parameters were included in the fitting procedure.

2.1.2 Photoelectron Diffraction

After the photoionization process, the photoelectron can be elastically scattered by the surrounding atoms. The interference between the photoelectron primary wave, which propagates towards the electron analyzer without undergoing any scattering event, and the diffused wave, originating from the elastic scattering of the primary wave with the surrounding atoms close to the primary emitter, produces strong modulation in the observed photoemission intensity, which depend on the photoelectron kinetic energy and the direction of propagation $\mathbf{k}$. This mechanism, schematically shown in fig. 2.4, is at the base of the X-Ray Photoelectron Diffraction (XPD) technique.

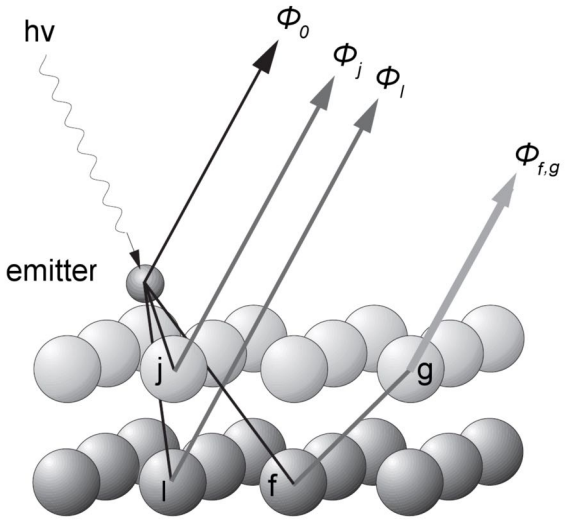

Figure 2.4: Schematic illustration of the photoelectron diffraction process.

From a practical point of view, XPD experiments are performed collecting photoemission spectra as a function of the azimuthal and polar angles of the sample (angular scan), or scanning the photoelectron kinetic energy (energy scan). The modulations contained in the XPD pattern provide a large amount of structural information about the local geometry around the emitting atom. This is primarily due to the rapid decrease of the photoelectron wave amplitude that allows to probe only the emitter's nearest neighbours configuration[8].

[8] In first approximation, the scattered wavefront is spherical, thus its intensity decrease as $1/r$.

When the scatterer is placed in line along the path between the emitter and the analyzer we have a *forward scattering* event. This is the prevalent scattering mechanism for kinetic energies above 150 eV. For lower photoelectron kinetic energies, the so called *backward scattering* becomes important, meaning that the electrons are elastically scattered by atoms behind the emitters. By relying on the chemical sensitivity intrinsic to photoemission spectroscopy, and by properly selecting the photoelectron kinetic energy, in order to maximize (or minimize) one of the two scattering mechanisms, XPD is the ideal tool to probe the short range order with chemical specificity.

From a theoretical point of view, photoelectron diffraction can be described in a multiple scattering framework. One of the most popular methods to perform multiple scattering calculations is based on the separable representation of the Green's function matrix, first developed by Rehr and Albers [8]. Theoretical simulations can be compared to the measured interference patterns to extract a very detailed quantitative information on the short-range structure around the emitting atom. In this thesis work we have used the Electron Diffraction in Atomic Cluster (EDAC) package [9]. The working principle of this code is based on the implementation of an atomic cluster and the use of multiple scattering theory to model the XPD pattern at a specific electron kinetic energy.

2.1.3 Absorption Spectroscopy

Besides photoelectron spectroscopy (or diffraction), other experimental techniques take advantage of the tunability of X-ray synchrotron radiation. This is the case of X-ray Absorption Spectroscopy (XAS). In a XAS experiment the radiation absorbed by the sample is measured as a function of the photon energy. Generally, an absorption spectra is characterized by several peaks corresponding to different resonances occurring when an electron is excited from one specific shell to an unoccupied valence state or to the continuum. These resonances are referred as K,L,M,.. absorption thresholds depending on atomic shell from which the electron is excited. It is worth noting that the K threshold consists of a single edge, because it corresponds to excitation of 1s electrons, while higher absorption thresholds are a superposition of edges. For instance, the L-edge is associated to excitations from $2s$, $2p_{1/2}$ and $2p_{3/2}$ levels, resulting in L1, L2 and L3 edges.

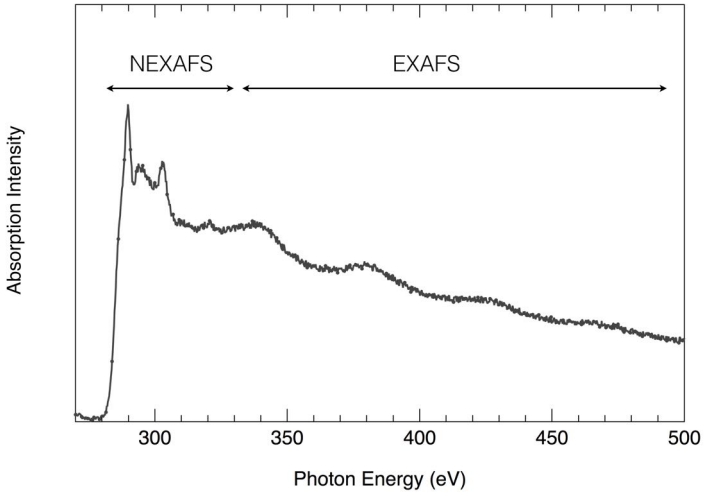

Figure 2.5: Schematic of a typical absorption spectrum.

A typical XAS spectrum, shown in fig. 2.5, presents two interesting regions. The first one, extending from about 50 eV up to few hundreds of eV beyond the absorption edge is referred as Extended X-ray Absorption Fine Structure (EXAFS). The second one, on the contrary, is called Near Edge X-ray Absorption Fine Structure (NEXAFS), or X-Ray Absorption Fine Structure (XANES), and extends up to about 50 eV beyond the threshold. In this section, we will focus on this latter part of the spectrum.

NEXAFS technique was developed in the 1980s [10] mainly in order to resolve the structure of molecules bonded to surfaces. It probes intramolecular transitions from a deep core shell (usually the K shell) into unoccupied molecular orbitals close to the vacuum level. The origin of NEXAFS resonances is schematically illustrated in fig. 2.6, where the case of a diatomic molecule is shown. Around the ionization threshold, resonant transitions are superimposed on the step-like shape. Such transitions occur if the energy of the incoming photons matches exactly the energy difference between the initial state and an unoccupied (molecular) state.

In addition to the informations on the electronic structure of molecules, NEXAFS can also probe their orientation. For this purpose, the polarization characteristics of synchrotron radiation are exploited. In the dipole approximation, as described in the previous sections, the photo-absorption cross section can be written as:

$$\sigma \propto |\langle \Psi_f | \epsilon \cdot \nabla | \Psi_i \rangle|^2 \rho_f(E) \tag{2.20}$$

where ϵ is the polarization vector of the incoming radiation. Assuming that

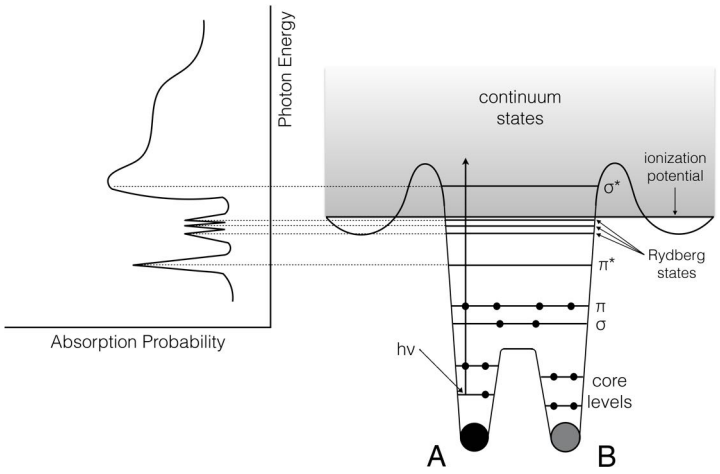

Figure 2.6: Schematic of the K-edge absorption spectrum (left) and potential (right) for a diatomic (A,B) molecule. π^* and σ^* resonances arise from the excitation of atomic 1s core level electrons to empty molecular orbital. The other resonances are due to transitions to Rydberg final states. Adapted from [11].

the radiation is linearly polarized (as in our case), the above equation can be furthermore simplified to:

$$\sigma \propto |\epsilon \cdot \langle \Psi_f | \nabla | \Psi_i \rangle|^2 \rho_f(E) \tag{2.21}$$

Finally, for a 1s initial state and a directional orbital final state, the matrix elements $\langle \Psi_f | \nabla | \Psi_{1s} \rangle$ points in the direction $\mathbf{\Omega}$ of the final state orbital [11], and the absorption cross section becomes:

$$\sigma \propto |\epsilon \cdot \langle \Psi_f | \nabla | \Psi_{1s} \rangle|^2 \propto |\epsilon \cdot \mathbf{\Omega}|^2 \propto \cos^2 \delta \tag{2.22}$$

where δ is the angle between ϵ and $\mathbf{\Omega}$.

For example, graphene is characterized by unoccupied in plane σ^* bonds, and, perpendicular to them, out of plane π^* bonds. From equation 2.23 it is clear that the modulation of the σ^* and π^* resonances induced by a linearly polarized light, is therefore opposite. When the impinging electric field polarization is in plane, the $1s \rightarrow \sigma^*$ resonance intensity is maximum, while the $1s \rightarrow \pi^*$ transition is inhibited. Viceversa, when the electric field polarization is perpendicular to the plane, only π^* resonances are measured.

Since in NEXAFS measurements we are probing transitions from the inner core level to unoccupied states near the vacuum level, the primary electrons cannot be directly measured. The solution comes by measuring one of the de-excitation channels products. During a NEXAFS measurements, the sample is

irradiated with monochromatic X-rays, the photon energy being varied around the ionization edge. When a photon is absorbed it can promote the excitation of one electron to an unoccupied state, leaving behind a core hole. The hole is subsequently filled by an electron either radiatively, with the emission of a fluorescent photon, or non-radiatively by the emission of an Auger electron. Both these channels are a direct measure of the presence of a core hole, as a result of the photoabsorption process. In principle, both channels can be detected, however, the Auger Electron Yield (AEY) is much higher than the fluorescence yield (FY) for low-Z molecules [12, 13]. Moreover, electron detection provides a higher surface sensitivity. The NEXAFS measurements presented in this thesis work were acquired using the AEY approach.

The Elettra Synchrotron Radiation Facility

Elettra is a third generation synchrotron radiation facility located in Basovizza (Trieste - Italy), which is optimized for the VUV and soft X-ray range. By synchrotron radiation we mean the light generated by relativistic electrons when they are accelerated on a curved trajectory and thus emit a highly collimated photon beam in the tangential direction [14]. The electron bunches are generated by thermoionic emission from a ceramic disc and first accelerated through a straight section (linear accelerator or LINAC) by two radio-frequency structures. The particles are subsequently injected into a booster ring where they are accelerated to the operating energy (2 or 2.4 GeV) and transported into the storage ring through a transfer line consisting of a series of deflection and focusing magnets. Inside the ring, the electrons are forced to follow a curvilinear orbit by different types of magnets (bending magnets, quadrupoles, sextupoles and steering magnets), while the energy they lose by emission of synchrotron radiation is reintegrated by four radio-frequency cavities. The storage ring includes also some straight sections which usually host insertion devices. These are the primary sources of high brightness X-Ray beams. An example of insertion device is an undulator, which consists of two periodic arrays of magnetic poles that force the incoming electrons to follow a wiggling trajectory, in such a way to irradiate. The reasons why synchrotron radiation is preferable to a conventional X-ray source are manifold: first of all, synchrotron radiation is tunable, in that a wide range of photon energies is accessible by properly adjusting the undulator gap; moreover synchrotron radiation yields a high brilliance (*i.e.* a low divergence high photon flux within a narrow bandwidth) and a high degree of polarization of the photon beam.

The SuperESCA beamline at Elettra

SuperESCA, the first beamline operating at Elettra since 1993 [15], is optimized for photoelectron spectroscopy measurements with soft X-rays. The radiation source is a two-sections 46 mm-period high brilliance undulator with 98 periods, that produces linearly polarized photons in the energy range 90-1500 eV. The light beam produced by the undulator is first pre-focused in the sagittal plane into the entrance slit, then monochromatized and, eventually, re-focused by an ellipsoidal mirror into the center of the experimental chamber. The resolving power ($E/\Delta E$) of the monochromator is of the order of 10^4 for hν<500 eV.

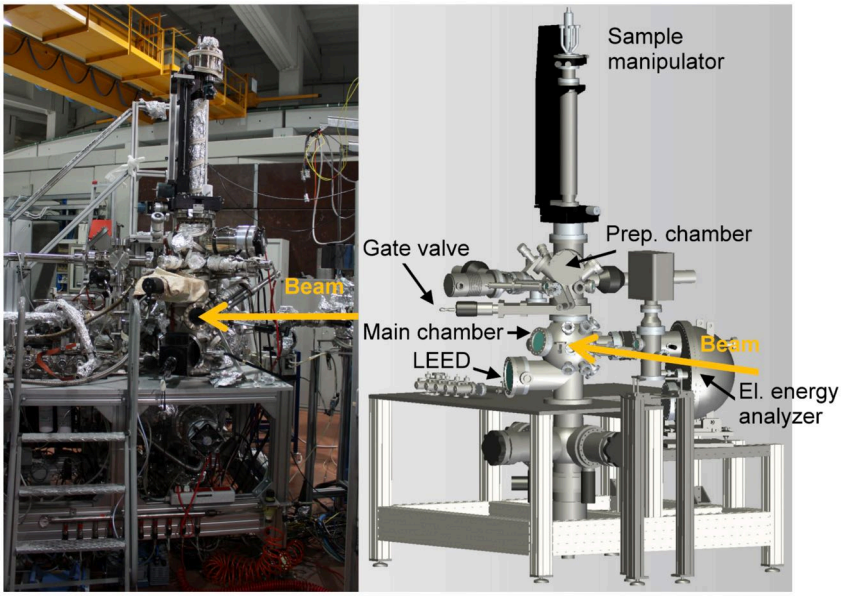

Figure 2.7: The end station of the SuperESCA beamline at Elettra.

The experimental station consists of two UHV chambers placed vertically and separated by a gate valve. A first stainless steel chamber is used for sample cleaning and preparation. The second chamber, instead, is made of μ-metal[9] and is devoted to the experimental measurements. A picture of the experimental setup is shown in fig. 2.7. Two different manipulators were used during experiments. The first one is a four degrees of freedom (corresponding to the x, y, and z axes, and to the polar angle Θ) manipulator with a liquid He cryostat which allows to vary the sample temperature in the 20-1500 K range. The second one, on the other hand, is a modified CTPO manipulator with 5

[9]This alloy is used to screen external magnetic field due to its high magnetic permeability.

degrees of freedom: 3 translational (x, y, and z) and 2 rotational (polar (Θ) and azimuthal (Φ)) axis. This manipulator is equipped with a liquid N_2 cryostat and an electron bombardment heating system which allows a sample temperature in the 120-1250 K range. Thanks to its fully motorized rotational movements, this manipulator is specifically designed for XPD investigations where the photoemission intensity is measured as a function of the emission angle. The chamber is further equipped with a series of evaporators for layer growth or cluster deposition, a quadrupole mass spectrometer, a LEED system, and a SPECS Phoibos electron analyzer with a mean radius of 150 mm, equipped with a custom made delay line detector [16].

An hemispherical electron analyzer consists of two hemispherical electrodes (of radius R_1 and R_2 respectively) held at a proper voltage (see fig. 2.8). The potential difference (V_2 - V_1) between the two hemispheres is given by:

$$V_2 - V_1 = V_0 \left(\frac{R_2}{R_1} - \frac{R_1}{R_2} \right) \tag{2.23}$$

This equation can be used to calculate the potentials to be applied to the hemispheres in order to select electrons with energy $E_0 = |e|V_0$, the so called pass energy. In fact, only the electrons impinging normal to the entrance slit of the analyzer and with energy E_0 follow a trajectory of radius $R_0 = (R_2 + R_1)/2$, which allows them to reach the exit slit and thus to be revealed by the detector. The instrumental energy resolution of the device depends on the geometrical parameters of the analyzer, on the angular divergence of the electron beam, and on the selected pass energy:

$$\Delta E = E_0 \left(\frac{\omega}{R_0} + \frac{\alpha^2}{4} \right) \tag{2.24}$$

where ω is the width of the slit, and α is the impinging angle of the electron beam at the entrance slit. Though the resolution improves with increasing R_0, technical problems related to the dimensions of the analyzer set an upper bound to the values of R_0 which are actually attainable. The electrostatic lenses in front of the analyzer absolve a double function: they collect the incoming photoelectrons from a large solid angle and focus them into the entrance slit of the analyzer and, at the same time, they slow down the electrons to the required kinetic energy E_0, in such a way to improve the resolution. Anyhow, the electron transmission probability of the system is damped at low pass energy, so that a compromise is actually required between a high energy resolution and a good signal to noise ratio.

At the SuperESCA beamline, the electrons that reach the exit slit are collected by a microchannel plate based detection system. When acquiring spec-

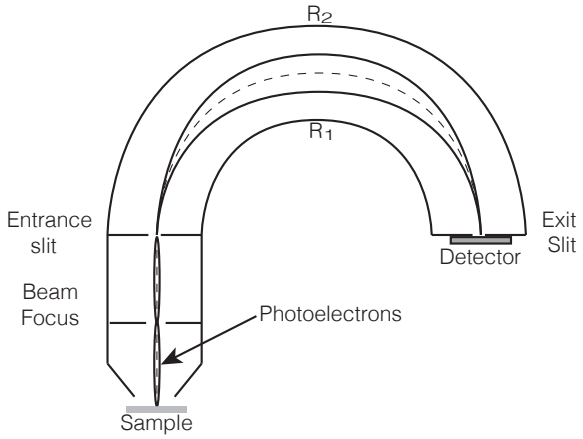

Figure 2.8: Illustration of a typical hemispherical electron analyzer.

tra in *sweep* (or scanning) mode, the voltages of the two hemispheres V_1 and V_2, and hence the pass energy, are held fixed; at the same time, the voltage applied to the electrostatic lenses is swept in such a way that each channel counts electrons with the selected kinetic energy for an interval equal to the given time window. In order to drastically reduce the acquisition time per spectrum, the so called *snapshot* (or fixed) mode is widely applied at the SuperESCA beamline. This procedure exploits the relation between the kinetic energy of a photoelectron and its position inside the detector. If the energy range covered by the detector is wide enough, and if the photoemission signal collected by a large number of channels is sufficiently strong (so that the spectral features can be clearly resolved), it is possible to acquire a detector image, thus obtaining the photoemission spectrum in one single shot, with an aquisition time of about 100 ms per spectrum.

The BaDElPh beamline at Elettra

The BaDElPh beamline is an undulator-based normal incidence monochromator instrument which provides photons in the energy range 4.6-40 eV with high flux, high energy resolution, and horizontal-vertical linear polarization. The beamline is specifically designed to perform high-resolution ARPES experiments from solids in the low photon energy regime.

The beamline end station consists of three UHV chambers: the heater chamber, the preparation chamber, and the analysis chamber. The manipulator used in this was 5 degrees of freedom fully motorized manipulator, equipped with a liquid He cryostat.

The photoelctron collection system consists of a SPECS Phoibos 150 mm equipped with a 2D-CCD detector. The electron detector is made up by a set of multichannel plates used to amplify the signal. After this amplification stage, the electrons are collected by a phosphorous screen. The image generated on the screen is recorded by a high resolution CCD camera. The use of a 2D detector offers the possibility of simultaneous acquisition of the energy as well as the angular distributions of the photoelectrons. This is achieved by probing both the dispersive plane and the non dispersive plane of the analyzer (see fig. 2.9). In the dispersion plane of the analyzer, that is the plane containing the focusing lenses and the detector, the electron energy can be detected in the range given by the pass energy. On the other hand, in the orthogonal plane the polar angle dispersion is detected, with a maximum angular acceptance of about 26°. With this setup, the overall angular resolution is about 0.1°, while the maximum energy resolution is about 5 meV.

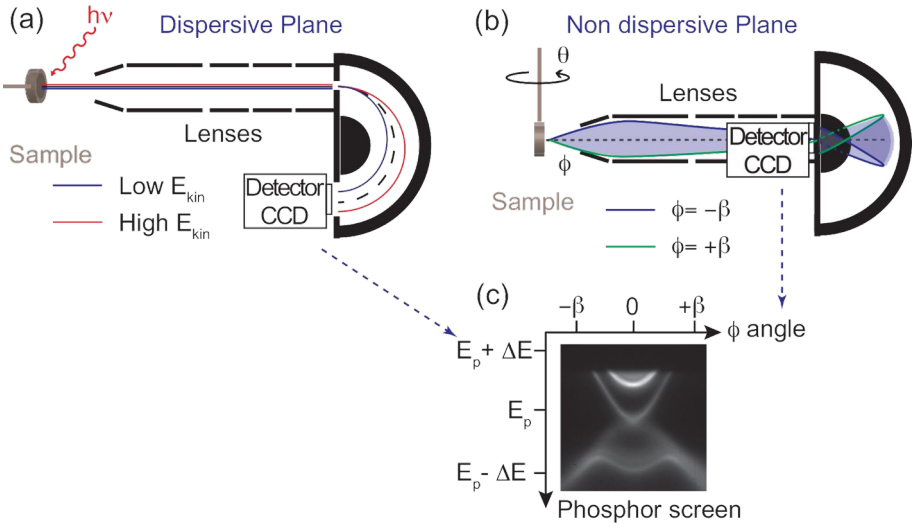

Figure 2.9: Scheme of the detection planes of an hemispherical electron analyzer. (a) Definition of the dispersive plane of the analyzer with the orbits of the higher (lower) kinetic energy electrons in red (blue). (b) Definition of the non-dispersive plane of the analyzer with the orbits of the electron emitted at an angle $+\beta$ ($-\beta$) in green (blue). (c) Sample image of an acquired spectrum.

The SGM3 beamline at Astrid

The SGM3 beamline (fig. 2.10) uses, as a source of light, the synchrotron radiation produced by ASTRID (Aarhus, DK) (now ASTRID 2). The radiation is, again, produced by an undulator, then monochromatized and finally focused

on the sample. The beamline is optimized for valence band photoemission measurements, with a photon energy range of 12-130 eV. The end station con-

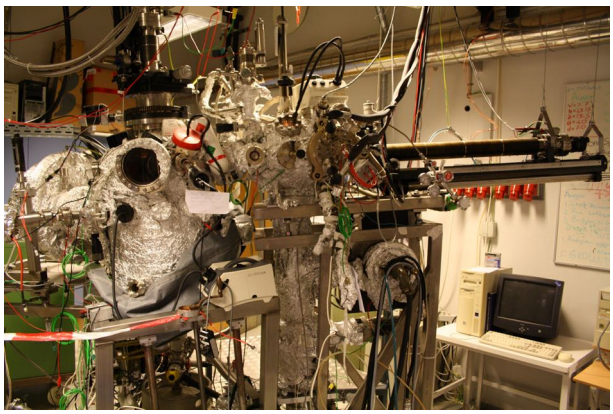

Figure 2.10: The experimental chamber of the SGM3 beamline at Astrid.

sists of two different UHV chambers: a first preparation chamber and the main chamber, where measurements are performed. The two chambers are separated by a valve, and are placed side-by-side. Every chamber has its own manipulator: the first one, in the preparation chamber, is placed horizontally and allow the transfer of the sample to the main chamber; the second one, instead, is placed vertically on the top flange of the main chamber. This manipulator has four degrees of freedom (x, y, z and Θ) and allows sample cooling to 70 K using liquid nitrogen. Both manipulators allow also sample annealing, but, due to the nature of the sample holder, in the main chamber annealing is limited to 230 K. The electron detection system consists of SPECS Phoibos 150 mm equipped with a 2D-CCD detector, as the one described before, with energy resolution better than 15 meV.

2.2 Low Energy Electron Diffraction

Low Energy Electron Diffraction (LEED) is an experimental technique used to investigate the surface structure of crystalline materials. Used for the first time by Davisson and Germer in 1927 [17] in an experiment of diffraction from a nickel surface, this technique is, even today, one of the most powerful tools used in the investigation of ordered surfaces owing to its wide range of applicability, its low cost and because it requires only an UHV environment to be used.

The investigation of diffraction patterns through low energy electron (20-400 eV) allows, by analyzing the directions in which these are scattered, to investigate the long-range order of the surface. In addition, with an approach based on the dynamic theory, it is possibile to reconstruct the precise geometric structure of the surface in question, and to obtain information on the bond lengths and the expansion/relaxation effects on the surface. The surface sensitivity is guaranteed by the mean free path of the electrons, that is less than 10 Å in the considered energy range (see fig. 2.2).

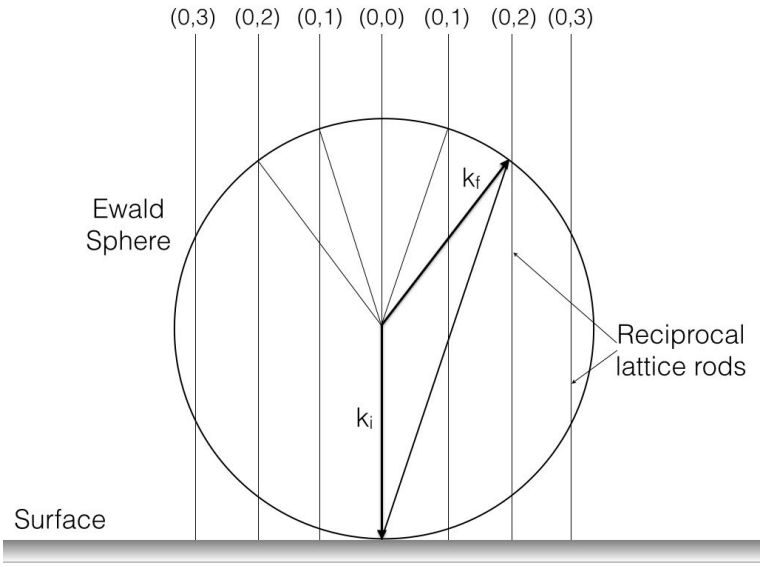

Figure 2.11: Reciprocal lattice representation of the Ewald sphere. k_i is the incident electron wave-vector, while k_f is the diffracted electron one.

In the single scattering approximation (kinematic theory), the electron is represented by a plane wave that, interacting with the surface, can be diffracted

along particular directions that satisfy the Bragg law:

$$n\lambda = d\sin\theta \tag{2.25}$$

where n is an integer number, λ is the de Broglie wave lentgh of the incoming electron[10], d is the inter-atomic distance, and θ is the diffraction angle. This equation can be interpreted in the reciprocal space through the geometric construction of the Ewald sphere, shown in fig. 2.11. The vertical lines perpendicular to the crystal surface are designed in correspondence to the points of the reciprocal lattice. The points of intersection between these lines and the Ewald sphere, the radius of which depends on the kinetic energy of the incident electrons, determine the solutions to the Bragg equation and, therefore, the directions of the scattered electrons.

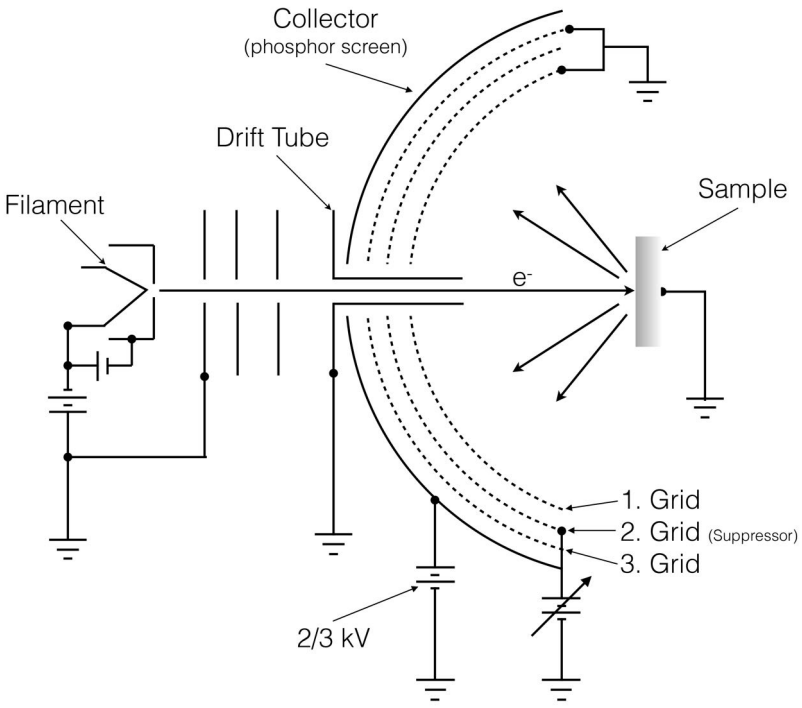

Figure 2.12: Schematic illustration of a typical LEED apparatus.

A typical LEED apparatus is presented in figure 2.12. A heated filament emits electrons, which are collimated by a system of lenses and then accelerated to the desired energy towards a drift tube. Once the collimated monochromatic beam reaches the sample, the electrons are backscattered from the sur-

[10]The de Broglie equation is given by $\lambda = h/mv$.

face and then collected. A first grid, which is grounded as the sample, is placed in order to screen electrostatic potentials and make the electrons to propagate into a field-free region. The other two grids are placed at a potential similar to that of the electron gun filament, so as to discard electrons resulting from inelastic scattering events. Elastically scattered electrons are then accelerated to a fluorescent screen by a positive potential of a few kV. LEED patterns collected on the fluorescent screen are then recorded by a CCD camera.

2.2.1 Spot Profile Analysis LEED

The two main limitations to the LEED technique are the poor transfer width, and the non linearity of the phosphor screen collector. The first one is related to the finite width of the diffraction spots, due to the intrinsic resolution limit of the apparatus. The conservation of the parallel component of the electron wave vector during the diffraction process requires that:

$$K_{||} = k_{||}^{out} - k_{||}^{in} = k|\sin\Theta_{out} - \sin\Theta_{in}| \tag{2.26}$$

where

$$k = \frac{2mE}{\hbar} \tag{2.27}$$

The minimum observable width in the k-space ($\Delta K_{||}$) allows us to define a width in the real space, usually referred as transfer width (w), corresponding to the maximum observable periodicity:

$$w = \frac{2\pi}{\Delta K_{||}} \tag{2.28}$$

By separating of the angular (w_Θ) and energetic (w_E) contribution to the transfer width, we obtain:

$$w_E = \frac{2\pi}{(\partial K_{||}/\partial E)\Delta E} = \frac{4\pi E}{K_{||}\Delta E} \tag{2.29}$$

$$w_\Theta = \frac{2\pi}{(\partial K_{||}/\partial \Theta_{out})\Delta\Theta_{out}} = \frac{\lambda}{\cos\Theta_{out}\Delta\Theta_{out}} \tag{2.30}$$

In conventional LEED, the main contribution is given by the angular spread, and typically the transfer width is limited to about 100 Å.

To overcome this limitation, a modified LEED apparatus, namely the Spot Profile Analysis LEED (SPA-LEED), was developed in the 1980s [19]. This particular kind of LEED system, reported schematically in fig. 2.13, introduces a set of electrostatic lenses between the electron gun and the sample. Specifically, the lenses consist of a three stage octupole plates and an entrance lens. The outer octupole sections are charged with an opposite potential, while the

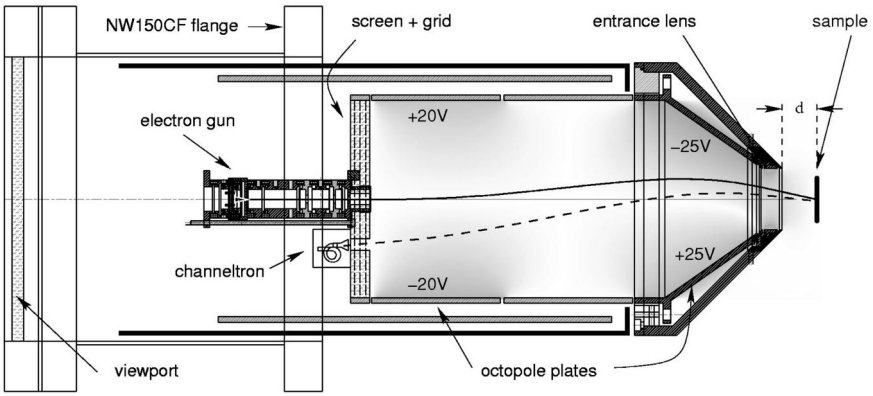

Figure 2.13: Schematic illustration of a typical SPA-LEED apparatus. Adapted from [18].

middle one is grounded. The electrons are therefore forced to follow an "S" shaped path inside the octupole. The final electrostatic lens, the entrance lens, consists of plane cylindrical lens which collimates the electron flux before impinging the sample. The diffracted electrons follow a similar "S" path and are eventually collected by a channeltron. The electron gun and the channeltron are placed on the same hypothetical hemisphere, centered on the sample, few centimeters apart, so that only the electron which are diffracted at a specific angle are collected. To obtain the full diffraction pattern, a reciprocal space scanning is performed, by changing the potential applied to the octupole plates in order to change the impinging angle of the electron on the sample, while keeping the angle between the primary and diffracted beam fixed. To understand this diffraction geometry, we must introduce a modified Ewald sphere (shown in fig. 2.14) in which the impinging and diffracted wavevectors rotate rigidly.

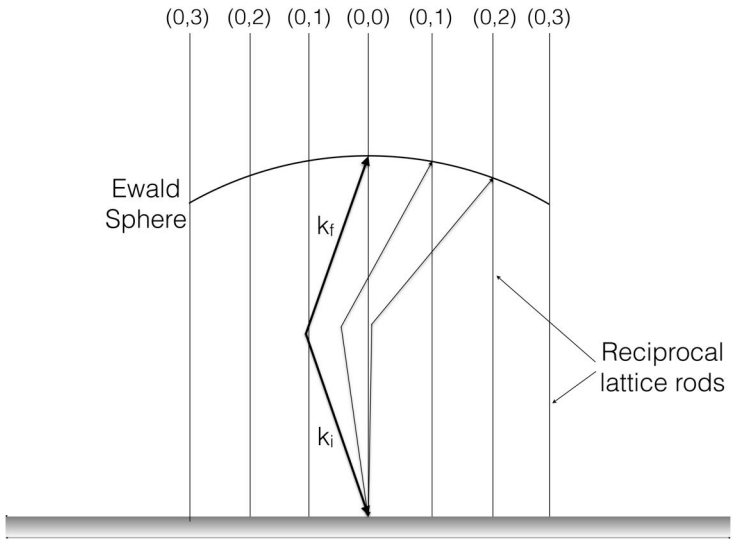

Figure 2.14: Modified Ewald sphere construction. The sphere is centered in (0,0) and has a radius given by $|\mathbf{k_i} - \mathbf{k_f}|$. Three different diffraction condition are shown.

Thanks to the deflection system, and especially to the entrance lens, the angular dispersion in a SPA-LEED instrument is minimized, so that the angular contribution to the transfer width becomes negligible. Therefore, the main contribution to the transfer width is given by the energetic part. To minimize it, the filament is obtained by a LaB_6 alloy, which offers better energetic monochromaticity with respect to conventional tungsten one. With this approach, the transfer width of our SPA-LEED was calculated to be larger than 1000 Å[20].

On the other hand, by using a channeltron as collector, the detection efficiency improves by about 4 orders of magnitude with respect to a normal phosphor screen, ensuring, at the same time, a better linearity in the acquisition range. This latter characteristic, together with the improved transfer width, allow the analysis of the fine structure of the diffraction spots, providing quantitative informations on the surface structure [21] which are usually not accessible in conventional LEED.

Thanks to the higher detection efficiency, SPA-LEED measurements are finally carried out with an order of magnitude lower electron current. This is reflected in a lower base pressure during measurements, and, most of all, minimizes the electron-induced desorption and dissociation which can be occasionally induced by conventional LEED[11].

The main limitations of the SPA-LEED technique, with respect to conven-

[11] For instance when measuring molecules weakly bounded to the substrate.

tional LEED, are the lower angular acceptance, due to the longer distance between the sample and the collector, imposed by the presence of the deflection system, and the longer acquisition time (about 2 orders of magnitude), due to pixel by pixel scanning.

The Surface Science Laboratory

The experimental chamber of the Surface Science Laboratory (University of Trieste and Elettra Sincrotrone Trieste, see fig. 2.15) is primarly devoted to electron diffraction, photoemission, and temperature desorption experiments. LEED experiments are carried out with a state of the art VG rear-view electron optical system, while the diffraction pattern are collected with a CCD camera. SPA-LEED measurements, on the other hand, are performed using a commercial Omicron SPA-LEED, with a custom written acquisition software.

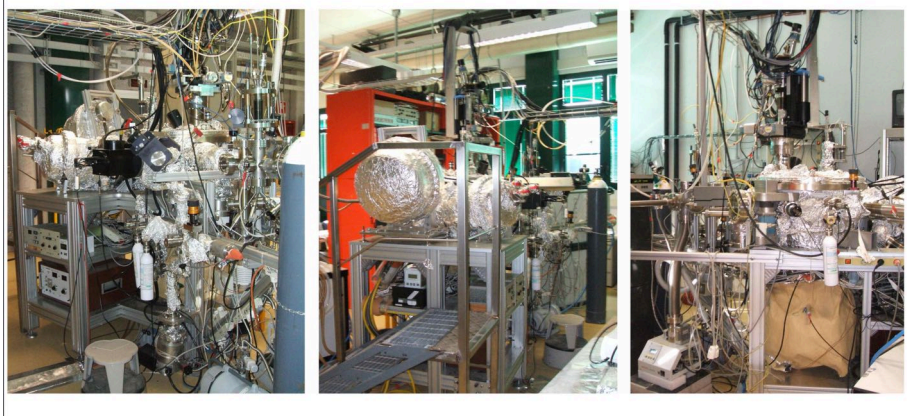

Figure 2.15: View from three different sides of the experimental chamber of the Surface Science Laboratory.

Beside the electron diffraction instrumentation, the laboratory is equipped with two conventional X-Ray sources, a $Mg - K_\alpha$ and an $Al - K_\alpha$ (which produce photon with an energy of 1253.6 and 1486.6 eV respectively) and a 150 mm hemispherical electron energy analyzer. Moreover, the accurate temperature control achievable with the particular sample mounting, combined with the presence of a quadrupole mass spectrometer, makes the system suitable also for Thermal Desorption Spectroscopy (TDS) experiments. The UHV chamber has a highly flexible configuration, thanks to the automated flange rotation and positioning system, which allows controlling the sample movements from remote, via a software interface. Several different instruments and evaporators can be installed on the different flanges of the chamber.

2.2.2 Low Energy Electron Microscopy

Low Energy Electron Microscopy (LEEM) [22, 23] is an example of cathode lens electron microscopy, *i.e.* a type of microscopy in which the sample acts as the cathode, by emitting electrons in the objective lens of the microscope. LEEM is a non-scanning technique, since each point of the surface is simultaneously imaged by means of elastically backscattered low energy electrons.

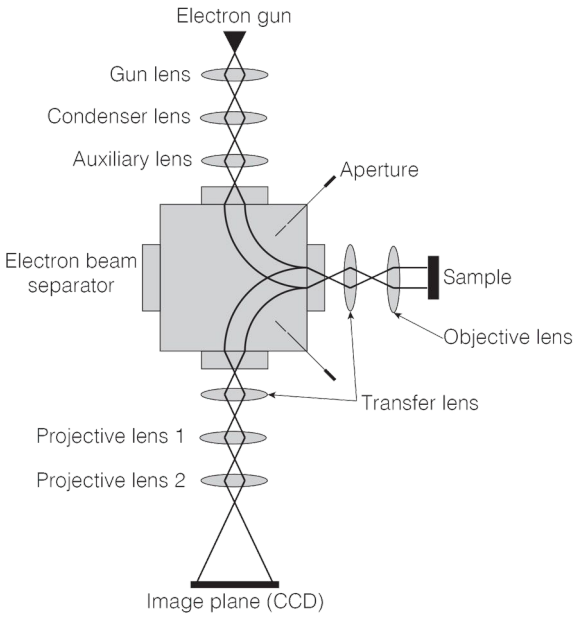

Figure 2.16: A typical LEEM system scheme.

The scheme of typical LEEM instrument is shown in fig. 2.16. A monochromatic electron beam is generated by a LaB_6 filament inside the electron gun and accelerated to the microscope potential (typically 18 kV). A set of electromagnetic lenses align the beam to the axis of the objective lens, perpendicularly to surface, and focus it in the crossover point of the back focal plane of the objective lens. The objective lens then align the incoming electron beam normal to the sample surface and decelerates it to the working energy[12]. The backscattered electrons flows through the objective lens in the opposite direction (while keeping a different trajectory in order to avoid electron-electron scattering events) and are eventually accelerated to the microscope potential and guided, by means of different sets of lenses, to the imaging column.

An image forms in the middle of the magnetic sector and a transfer lens, placed in front of the imaging column, reproduces the diffraction pattern on

[12]The energy range of LEEM measurements is typically from few eV to hundreds of eV

a secondary diffraction plane inside the column. The LEED pattern can be simply obtained as an image of the diffraction plane; alternatively, a real-space image can be collected by inserting a contrast aperture in the diffraction plane and selecting one of the diffracted beams. Placing an aperture along the beam path inside the illumination column enables selecting the field of view, *i.e.* the width of the surface region to be imaged. In this way, when operating the microscope in LEED mode, it is possible to collect the micro-spot low energy electron diffraction (μ-LEED) pattern of a restricted region of the sample.

Following the conventional Ewald sphere formalism, the normal incidence and exit condition, which is most often used for LEEM imaging corresponds to diffraction along the (00) reciprocal lattice rod. This is the so-called *bright-field* imaging mode, corresponding to specular reflection with no momentum transfer in the direction parallel to the surface. Alternatively, a *dark-field* image of the surface can be obtained by collecting the diffraction signal from a specific diffraction spot. Bright field is the standard mode of operation because it yields the best spatial resolution, but working in dark field mode allows separating the contributions of rotationally inequivalent domains and overlayers which are indistinguishable at normal incidence, where they don't produce contrast.

There are essentially two mechanisms that produce contrast in LEEM: phase contrast and quantum size contrast. In the first, the height difference between terraces on the surface leads to a phase difference in the backscattered waves. Defocussing can convert such phase difference into an amplitude difference, allowing to image steps on a surface. The second method exploits the interference of waves that are backscattered at the surface and at the interface of a thin film, producing maxima and minima in the backscattered intensity depending on the local film thickness.

Besides the excellent lateral resolution, which can be pushed down to the nanometer scale, LEEM is a surface sensitive techniques, thanks to the short mean free path of the electrons in the 50-100 eV kinetic energy range. On the other hand, by working with very low energy electrons (down to few eV), which have a mean penetrating depth of several nanometers, LEEM offers a unique opportunity to probe also deeper layers and interfaces. Moreover, electrons in the very low energy range have a very high reflectivity, which, combined with the non-scanning imaging mechanism, is translated into a short image acquisition time and a real-time imaging capability.

The Nanospectroscopy beamline at Elettra

The Nanospectroscopy beamline at Elettra (see fig. 2.17) is equipped with a state-of-the-art Elmitec LEEM apparatus with a lateral resolution of few tens of nm. Moreover, when the electron source of the microscope is replaced by the incoming x-ray synchrotron radiation, which causes the emission of photoelectron from the sample, the instrument can be used to acquire photoemission electron microscopy (PEEM) data, as well as μ-ARPES and μ-XPS spectra. These techniques can combine the spatial resolution of electron microscopy and the chemical sensitivity of photoelectron spectroscopy, opening new possibilities for the local characterization of the samples. The microscope operates under UHV condition, with a base pressure of the order of 10^{-10} mbar. A preparation chamber, connected to the main experimental chamber by a valve, is used for sample cleaning and preparation. Selected gases can be directly dosed in the main chamber, where several evaporators can be also mounted.

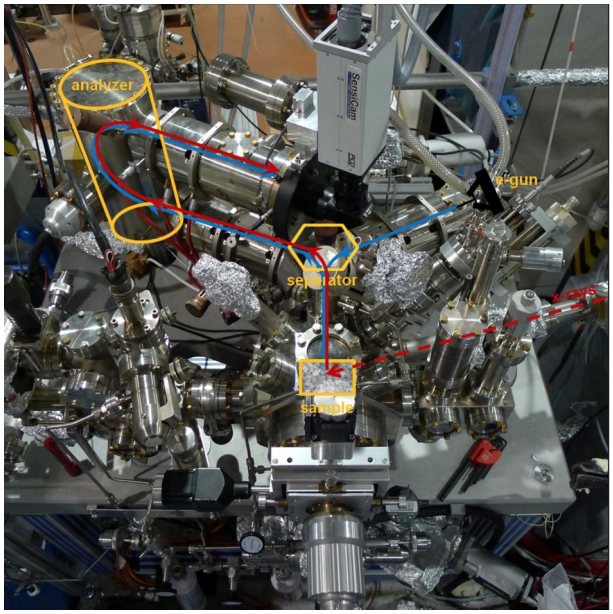

Figure 2.17: The experimental chamber of the Nanospectroscopy beamline at Elettra.

Bibliography

[1] D. P. Woodruff and T. A. Delchar, editors. *Modern Techniques of Surface Science*. Cambridge University Press, 1994.

[2] G. D. Mahan. Theory of photoemission in simple metals. *Physical Review B*, **2**(11):4334, 1970.

[3] W. Schattke and M. A. Van Hove. *Solid-state photoemission and related methods: Theory and experiment*. John Wiley & Sons, 2008.

[4] C. S. Fadley, S. B. M. Hagstrom, M. P. Klein, and D. A. Shirley. Chemical Effects on Core-Electron Binding Energies in Iodine and Europium. *The Journal of Chemical Physics*, **48**(8):3779–3794, 1968.

[5] S. Doniach and M. Šunjic. Many-electron singularity in X-ray photoemission and X-ray line spectra from metals. *Journal of Physics C: Solid State Physics*, **3**(2):285, 1970.

[6] J. J. Joyce, M. Del Giudice, and J. H. Weaver. Quantitative analysis of synchrotron radiation photoemission core level data. *Journal of Electron Spectroscopy and Related Phenomena*, **49**(1):31–45, 1989.

[7] János Végh. The Shirley background revised. *Journal of Electron Spectroscopy and Related Phenomena*, **151**(3):159–164, 2006.

[8] J. J. Rehr and Albers. R. C. Scattering-matrix formulation of curved- wave multiple-scattering theory: Application to x-ray-absorption fine structure. *Physical Review B*, **41**:8139, 1990.

[9] F. J. Garcia de Abajo, M. A. Van Hove, and C. S. Fadley. Multiple scattering of electrons in solids and molecules: A cluster-model approach. *Physical Review B*, **63**:075404, 2001.

[10] J. Stöhr. *NEXAFS spectroscopy*, volume **25**. Springer Science & Business Media, 2013.

[11] G. Hähner. Near edge X-ray absorption fine structure spectroscopy as a tool to probe electronic and structural properties of thin organic films and liquids. *Chemical Society Reviews*, **35**(12):1244–1255, 2006.

[12] H. Winick and S. Doniach. *Synchrotron radiation research*. Springer Science & Business Media, 2012.

[13] M. O. Krause. Atomic radiative and radiationless yields for K and L shells. *Journal of Physical and Chemical Reference Data*, **8**(2):307–327, 1979.

[14] A. Hofmann. *The physics of synchrotron radiation*, volume **20**. 2004.

[15] A. Abrami, M. Barnaba, L. Battistello, A. Bianco, B. Brena, G. Cautero, Q. H. Chen, D. Cocco, G. Comelli, S. Contrino, F. DeBona, S. Di Fonzo, C. Fava, P. Finetti, P. Furlan, A. Galimberti, A. Gambitta, D. Giuressi, R. Godnig, W. Jark, S. Lizzit, F. Mazzolini, P. Melpignano, L. Olivi, G. Paolucci, R. Pugliese, S. N. Qian, R. Rosei, G. Sandrin, A. Savoia, R. Sergo, G. Sostero, R. Tommasini, M. Tudor, D. Vivoda, F. Q. Wei, and F. Zanini. SuperESCA: First beamline operating at Elettra. *Review of Scientific Instruments*, **66**(2):1618–1620, 1995.

[16] G. Cautero, R. Sergo, L. Stebel, P. Lacovig, P. Pittana, M. Predonzani, and S. Carrato. A two-dimensional detector for pump-and-probe and time resolved experiments. *Nuclear Instruments and Methods in Physics Research Section A: Accelerators, Spectrometers, Detectors and Associated Equipment*, **595**(2):447–459, 2008.

[17] C. Davisson and L.H. Germer. Diffraction of Electrons by a Crystal of Nickel. *Physical Review*, **30**:705, 1927.

[18] P. Zahl and M. Horn-von Hoegen. Third-generation conical spot profile analyzing low-energy electron diffraction. *Review of Scientific Instruments*, **73**(8):2958–2962, 2002.

[19] U. Scheithauer, G. Meyer, and M. Henzler. A new LEED instrument for quantitative spot profile analysis. *Surface Science*, **178**(1):441–451, 1986.

[20] S. Lizzit, A. Baraldi, Ch. Grütter, J. H. Bilgram, and Ph. Hofmann. The surface phase transition and low-temperature phase of α-Ga(010) studied by SPA-LEED. *Surface Science*, **603**(21):3222–3226, 2009.

[21] M. Horn-von Hoegen. Growth of semiconductor layers studied by spot profile analysing low energy electron diffraction-Part I. *Zeitschrift für Kristallographie*, **214**(10):591–629, 1999.

[22] E. Bauer. Low energy electron microscopy. *Reports on Progress in Physics*, **57**(9):895, 1994.

[23] E. Bauer. LEEM basics. *Surface Review and Letters*, **5**(06):1275–1286, 1998.

3 CVD graphene synthesis and characterization

Chemical Vapor Deposition is one of most commonly employed approaches for Gr synthesis on TM surfaces. During CVD growth the C atoms are provided to the system by exposing the TM substrate to gas phase hydrocarbon precursors. The decomposition of the precursor molecules to form atomic C, which eventually becomes involved in the nucleation of single-layer graphene islands, is achieved by annealing the TM substrate. CVD can be performed either at fixed temperature, or varying the sample temperature during the process. In the latter case the process is referred to as Temperature Programmed Growth (TPG). CVD growth has proved successful on a number of different TM surfaces, including, for example, Ir(111) [1, 2], Ru(0001) [3], Rh(111) [4], Pt(111) [5], Re(0001) [6], Ni(111) [7, 8], Co(0001) [9], and Cu [10].

However, the complete picture of the atomistic processes occurring at the surface during hydrocarbon decomposition is, to a large extent, still unknown. The first part of this chapter is devoted to the characterization of the dissociation path of ethylene on Ir(111) during TPG Gr growth. A previous experimental work [11], carried out by our research group, attempted to identify the chemical species involved in this process by means of fast-XPS measurements. However, in that case, the classification of the various molecular species was complicated by the lack of high resolution spectra, as well as by the lack of any theoretical input. In the following section we demonstrate how, by combining fast and high resolution photoelectron spectroscopy to DFT calculations, it is possible to unambiguously reconstruct the full dissociation path up to atomic C formation. DFT calculations presented in this section were performed by a collaborating group of theoretician headed by Prof. Kantorovich at the King's College London.

The second part of this chapter is instead devoted to the spectroscopic characterization of the Gr-substrate interaction with a variety of TM surfaces. The interaction between Gr and TM surfaces is known to be largely dependent on the TM choice [12, 13, 14]. For example, when grown on Ir(111), Gr weakly

interacts with the TM surface and is found in a quasi free standing and almost flat configuration quite far from the surface (> 3.0 Å) [2]. On the other hand, the interaction between Gr and a Ni(111) is so strong that the whole electronic structure of Gr is strongly perturbed, and the typical linear band dispersion of Gr is lost [7]. Finally, when grown for example, on Ru and Rh, Gr shows a large corrugation alternating weakly interacting regions, which stand far from the surface, to strongly interacting areas close to the surface [3, 4]. The two possible sources for this large variety of different behaviors must be found in the chemical composition of the TM surface and in the lattice mismatch between Gr and the substrate. To separate these two contributions we designed an experiment which consisted of growing Gr on Ir(111) and Ru(0001) and subsequently intercalate different metallic species underneath Gr. By properly adjusting the evaporation parameters we were able to obtain epitaxial buffer layers with near monolayer coverage at the Gr-TM interface, thus modifying the surface chemistry of the system without altering its geometrical configuration. DFT calculation, performed by the group of Prof. Alfé at UCL, assisted and supported our analysis.

3.1 Ethylene Chemical Vapor Deposition on Ir(111): initial stages of graphene synthesis

This experiment was designed to understand the details of CVD Gr synthesis on transition metals. In particular we characterized, by combining XPS data to DFT simulations, the ethylene dissociation process on Ir(111) up to atomic C formation. The Ir(111) surface was exposed to ethylene (C_2H_4) at 90 K. Fig. 3.1 (a) shows a series of fast C 1s core level photoemission spectra acquired as a function of the C coverage[1] on the surface during ethylene adsorption. At low coverage we observe the simultaneous appearance of two components at 283.8 eV (a_1) and 283.3 eV (a_2) BE which are interpreted as a singular molecular species with two non equivalent C atoms, suggesting that the C-C bond is preserved. This assumption is motivated by the observation that their intensity increases coherently with increasing exposure, preserving a constant intensity ratio and BE difference. Above 0.06 ML we observe a new doublet at lower BE due to a different C_2H_n species. While the peak at 282.7 eV BE (b_2) can be easily distinguished, the second peak (b_1) is partially hidden by the $a_{1,2}$ components, and results in a spectral shoulder slightly above 283 eV. With a further increase in the ethylene exposure, a new broad feature can be observed at BEs larger than 284 eV (ml). The observation that in the absence of ethylene flux the intensity of this latter component rapidly decreases is consistent with the presence of ethylene multilayers. This behavior is expected for weakly interacting species at the condition of surface adsorption-desorption equilibrium [15].

Fig. 3.1 (b) shows a LEED pattern acquired after ethylene deposition at 90 K up to saturation (0.61 ML), followed by annealing to 340 K. Besides the diffraction spots originating from the Ir(111) substrate (black), we observe an additional set of spots related to the adsorbed molecules (red, cyan and yellow). The diffraction pattern is interpreted in terms of a c(4×2) structure, with three differently oriented domains, as shown in fig. 3.1 (c). Following this finding, theoretical calculations were performed using a c(4×2) unit cell.

The dissociation kinetics was monitored by temperature programmed XPS (TP-XPS) [16] measurements, reported in fig. 3.2. In light of the uptake experiment, we carried out TP-XPS experiments for three different initial ethylene coverages (highlighted in red on fig. 3.1 (a)), corresponding to the presence

[1] The C coverage was calculated comparing the C 1s integral area to the one obtained for a single layer of Gr on Ir(111). Given the lattice parameter of Ir(111) (2.71 Å) and Gr (2.46 Å), the C coverage for a single Gr layer is approximately given by $2 \cdot \left(\frac{2.71}{2.46}\right)^2 = 2.44$ ML.

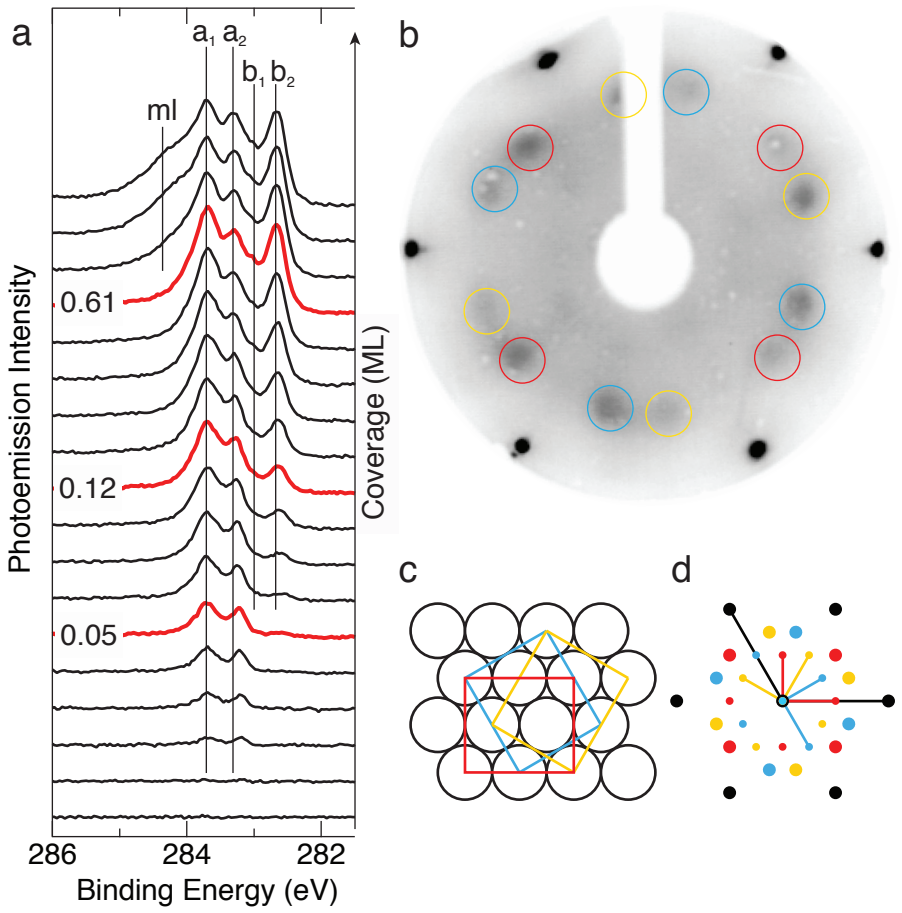

Figure 3.1: (a) C 1s photoemission spectra acquired during ethylene uptake at 90 K. The three spectra highlighted in red correspond to the three coverages used throughout the experiment. (b) LEED pattern acquired at 55 eV after ethylene deposition (0.61 ML) and annealing to 340 K, (c) real space model and (d) simulated diffraction pattern for a c(4×2) superstructure with three rotated domains.

of just the first molecular species (0.05 ML), a mix of the two (0.12 ML), and the saturated surface (0.61 ML), just before multilayer growth. The chemical evolution occurring at the surface is reflected in strong BE shifts and modifications of the C 1s core level line shape. In particular, we observe sharp transitions at about 250, 380 and 500 K (high coverage series), while at high temperature (T > 800 K) the C 1s spectrum smoothly becomes narrower and moves to higher BE. At the highest temperature, above 1000 K, the appearance of a spectral component at 284.1 eV is observed, which is the fingerprint of the initial nucleation of graphene islands [2, 17]. Most importantly, the C 1s core level evolution is only slightly influenced by the initial C coverage. In fact, the qualitative behavior is similar for the three selected coverages, while only minor modifications to the temperature range of each transition are observed, especially at the lower coverage.

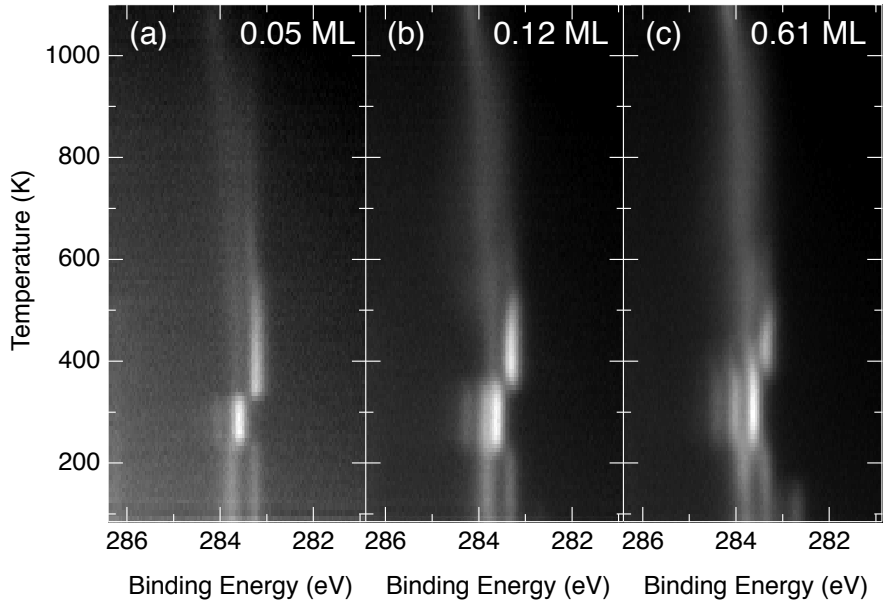

Figure 3.2: 2D plots corresponding to the TP-XPS C 1s spectral sequence acquired during the annealing from 90 K to high temperature for three different ethylene coverages. Each horizontal cut in the figures corresponds to a single photoemission spectrum acquired at a given temperature and its intensity is plotted using a color scale.

The most important spectral change in the low temperature range (T<200 K) of the highest coverage series is the decrease of the $b_{1,2}$ components, which transform into $a_{1,2}$. This suggests that, at T=90 K, the lower BE doublet can originate from ethylene species that adsorb without dissociation on

the empty sites of the surface initially covered with dissociated C_2H_n species, in agreement with previous assignments [11], and that complete dissociation of CH_2CH_2 takes place only above 200 K. Above 200 K the TP-XPS spectra are more complicated to interpret because of the overlap of spectral features originating from non-equivalent C atoms of different C_nH_m species with other components due to vibrational splitting. Indeed, it is known that, when measured with high energy resolution, the C 1s core level spectra of small hydrocarbon molecules can display vibrational fine structure due to the excitation of C-H vibrational motion in the final state [18, 19].

To shed light on the dissociation path we performed low temperature high resolution C 1s photoemission experiments after annealing the high coverage ethylene structure (0.61 ML) to selected temperatures, which were chosen to be representative of a single molecular species. High resolution photoemission spectra were then compared to DFT calculated BEs for all the possible dissociation products. Furthermore, the dissociation barriers for all the reactions, including dehydrogenation, hydrogenation, isomerization and C-C cleavage reactions, were calculated and the full dissociation path, up to the atomic C formation, was deduced. A reaction scheme for the decomposition of ethylene to carbon, incorporating all processes that the various hydrocarbon species might undergo is reported in fig. 3.3, while the corresponding energy barriers for the various reactions are listed in table 3.1. Table 3.2 shows the BE shifts for all the possible dissociation products, calculated after relaxing each molecular species to the most favourable bonding site to the substrate. High resolution XPS spectra are instead reported in fig. 3.4, together with the deduced dissociation path.

	Reaction	$\mathbf{E_f}$ **(eV)**	$\mathbf{E_b}$ **(eV)**
1	$CH_2CH_2 \rightarrow CH_2CH + H$	0.39	0.58
2	$CH_2CH_2 + H \rightarrow CH_3CH_2$	0.70	0.35
3	$CH_2CH \rightarrow CH_2C + H$	0.34	0.59
4	$CH_2CH + H \rightarrow CH_3CH$	0.64	0.27
5	$CH_3CH_2 \rightarrow CH_3CH + H$	0.33	0.49
6	$CH_3CH_2 + H \rightarrow CH_3CH_3$	2.16	–
7	$CH_2C + H \rightarrow CH_3C$	0.84	0.99
8	$CH_3CH \rightarrow CH_3C + H$	0.46	1.48
9	$CH_2CH_2 \rightarrow CH_3CH$	1.39	1.20
10	$CH_2CH \rightarrow CH_3C$	1.37	2.01
11	$CHC + H \rightarrow CH_2C$	0.54	1.17
12	$CHC \rightarrow C\text{-}C + H$	1.23	0.65
13	$CHCH \rightarrow CHC + H$	1.23	0.58
14	$CHCH + H \rightarrow CH_2CH$	1.80	0.55
15	$CHCH \rightarrow CH_2C$	2.44	2.52
16	$CH_3 \rightarrow CH_2 + H$	0.50	0.58
17	$CH_2 \rightarrow CH + H$	0.09	0.83
18	$CH \rightarrow C + H$	1.11	0.66
CB1	$CH_2CH_2 \rightarrow CH_2 + CH_2$	1.45	0.61
CB2	$CH_3CH_2 \rightarrow CH_3 + CH_2$	1.56	1.47
CB3	$CH_3CH \rightarrow CH_3 + CH$	0.89	1.31
CB4	$CH_2CH \rightarrow CH_2 + CH$	1.07	1.44
CB5	$CH_2C \rightarrow CH_2 + C$	1.29	0.21
CB6	$CHCH \rightarrow CH + CH$	0.82	1.15
CB7	$CHC \rightarrow CH + C$	0.73	1.29
CB8	$CC \rightarrow C + C$	1.18	1.29
H	$H + H \rightarrow H_2$	1.25	–

Table 3.1: Energy barriers for the various reactions. E_f is the energy barrier associated with the forward reaction while E_b is the backward reaction barrier.

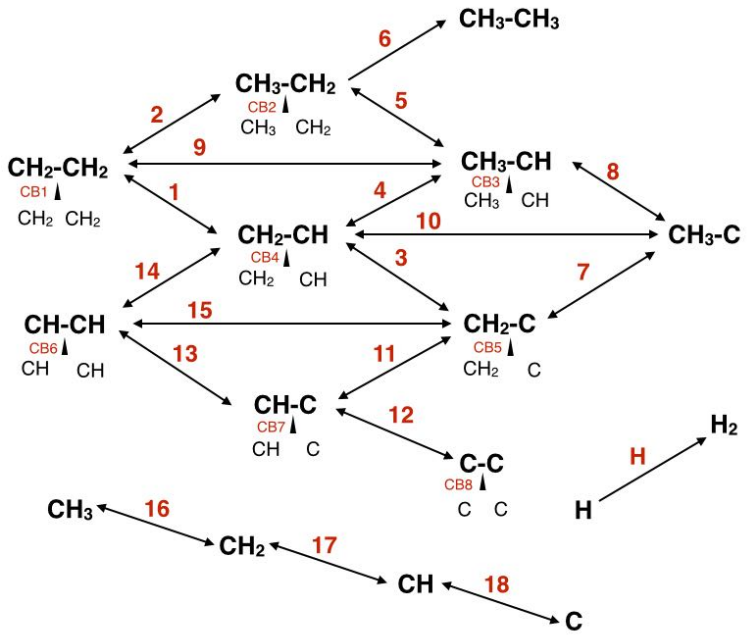

Figure 3.3: Possible reactions considered for the conversion of ethylene into atomic C. Upward and downward diagonal arrows represent hydrogenation and dehydrogenation reactions, respectively, while the horizontal arrows show isomerization processes. The reactions are numbered for later reference. C-C breaking reactions (labelled as CB) are indicated beneath each species with small vertical arrows.

DFT calculations cannot yield absolute values for the core level BEs but rather core level BE shifts, hence the DFT calculated BE scale has to be aligned to the experimental one. This was achieved by requiring an energy match between the calculated BE for the C 1s core levels for CH_2C and the experimental values obtained by fitting the high BE doublet of the low temperature high-resolution spectrum acquired after ethylene exposure. This assumption was made on the basis of the calculated reaction barriers (table 3.1), which indicate that at low temperature the system will most likely progress by following reactions 1 and 3 to form CH_2C (fig. 3.3), and therefore that this is the first and only stable species present on the surface after ethylene starts to dissociate. Our calculations suggest that CH_2C has two non-equivalent C atoms with a C 1s BE splitting of 0.49 eV, which nicely describes the highest BE doublet observed for the lowest temperature spectrum in fig. 3.4 (a). On the other hand, the lower BE component is assigned to molecular ethylene since the corresponding DFT calculated BE falls close to the experimental value. Small deviations can be accounted for by considering the presence of a dense layer, with non-negligible

lateral interactions, which can cause the C atoms within the molecules to be in different local chemical environments. This assumption is further confirmed by the fact that, as soon as the temperature increases, this low BE feature completely converts into the higher BE doublet, indicating that the metastable C_2H_4 residual molecules dehydrogenate to CH_2C, in good agreement with previous qualitative observations by fast-XPS (fig. 3.2).

Species	**BE$_{\mathrm{CLS}}$ (eV)**
CH_2CH_2	0
CH_2CH	0.03, 0.30
CH_3CH	0.62, 0.32
CH_3C	1.08, 0.88
CH_3CH_2	0.41, -0.14
CH_2C	0.55, 1.04
CHCH	0.69
CHC	1.16, 1.27
CC	0.96
CH_3	-0.41
CH_2	0.01
CH	0.59
C	0.45

Table 3.2: C 1s core level BEs shifts calculated for all the possible molecular species during ethylene dissociation. The values are referred to ethylene. For those species exhibiting two non equivalent C atoms, two energies are given.

After annealing to 323 K a new dehydrogenation product is observed, exhibiting a vibrational fine structure (spectrum at 323 K in fig. 3.4). To obtain the vibrational splitting we fitted a sum of D-S functions, with the same line shape and energy separation for all the vibrational replicas, to the experimental data (fig. 3.5)). The obtained value of 405 $\pm$ 10 meV is compatible with a C-H stretching mode. To identify this molecular species we started by analyzing the DFT calculated reaction barriers. It is important to stress that, since the calculated barrier for molecular hydrogen formation on the surface is 1.25 eV, atomic hydrogen could still be present on the surface in this temperature range, so that also hydrogenation reactions must be accounted for. Starting from CH_2C the lowest energy barrier (0.84 eV) forward reaction is the hydrogenation reaction number 7 that leads to CH_3C formation on the surface. Since the inverse reaction, as well as reaction 8 and 10 resulting in CH_3CH and CH_2CH respectively,

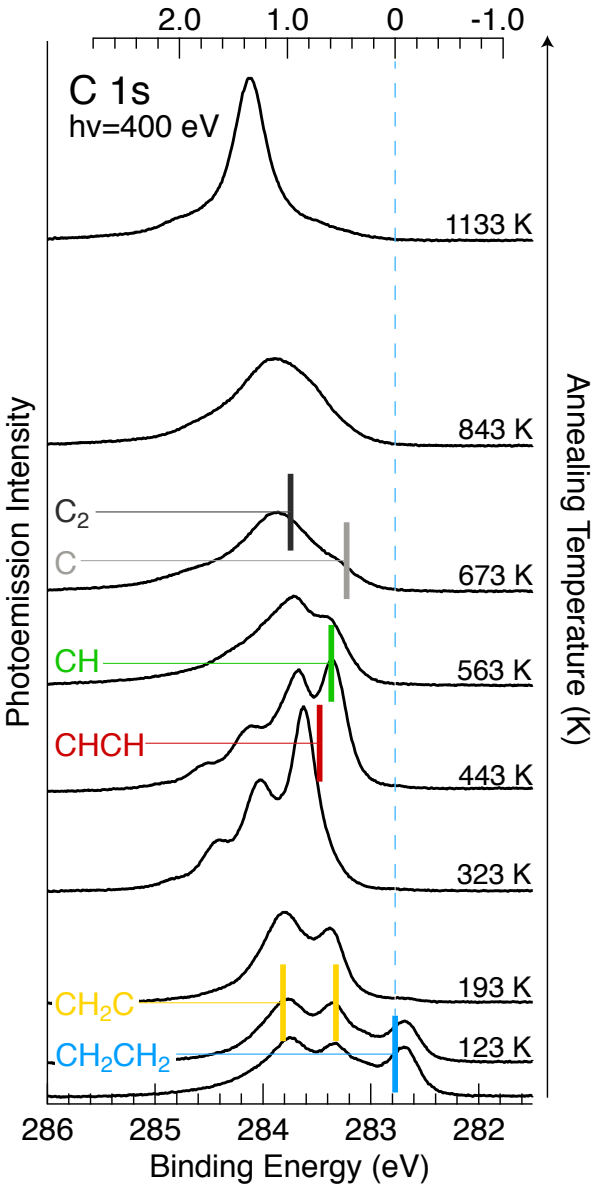

Figure 3.4: C 1s high-resolution XPS spectra acquired at 90 K after annealing the ethylene covered substrate to selected temperatures. From the bottom upwards, spectra acquired after exposure at 90 K, and after annealing at increasing temperatures. The DFT calculated BEs for the molecular species involved in the dissociation process are shown superimposed.

have a higher activation barrier, CH_3C is expected to be stable on the surface. However, the calculated CH_3C C 1s components (see table 3.2) consist of a doublet splitted by 200 meV that is not experimentally observed, thus excluding this reaction path. On the other hand, the isomerization reaction 15, resulting in CHCH formation, as well as the C-C bond cleavage reaction CB5 are easily excluded because of their high reaction barrier (2.52 and 1.29 eV respectively). CH_2C could therefore hydrogenate back to form CH_2CH (reaction 3, 0.59 eV barrier) and immediatley dehydrogenate to CHCH (reaction 14, 0.55 eV barrier). CHCH is then expected to be stable on the surface for a while, since the energy barriers for all the possible reactions involving CHCH are much higher. Another possibility for CH_2C is to follow reaction 11 to form CH-C (1.17 eV barrier), which could then either hydrogenate to form CHCH (reaction 13, 0.58 eV barrier) or dissociate to CH + C (reaction CB7, 0.73 eV barrier). Unfortunately, the calculated C 1s BEs for C, CH, and CHCH are quite similar, so that a discrimination based solely on their BEs is not possible. For this reason we calculated the C*-H vibrational energy for the possible reaction products with core-hole excited C atom (denoted C*), which turned out to be 380 meV for CHCH and 340 meV for CH. Since the calculated vibrational energy for CHCH shows, by far, the best agreement with the experimental value (405 meV) we assign this molecular species to CHCH.

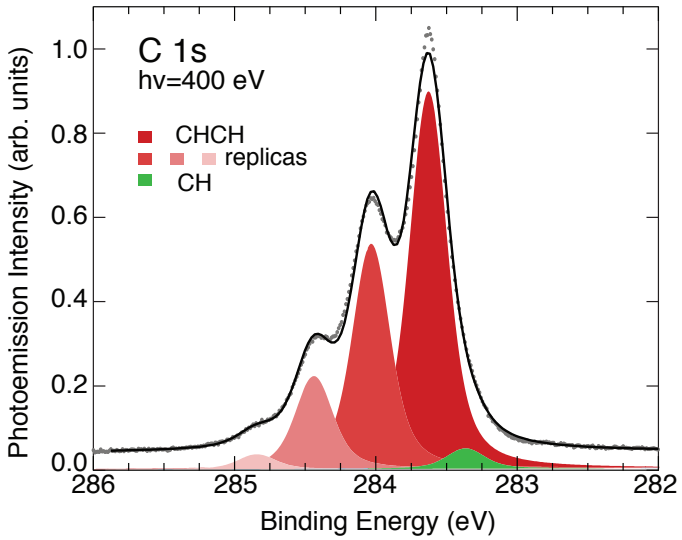

Figure 3.5: Fit of the spectrum acquired at 90 K after annealing to 323 K. This spectrum shows, besides the main peak, vibrational replicas with a BE splitting of 405 meV. A small amount of CH is already present at this temperature, reflected in the small green peak.

The next reaction product is interpreted as CH, since C-C bond cleavage (CB6) is the lowest energy barrier reaction. CH is indeed observed after annealing to 443 K (spectrum at 443 K in fig. 3.4) together with residual CHCH. At higher temperature the last dehydrogenation occurs, leaving atomic C on the surface that can then diffuse forming larger C_n cluster and eventually, above 1100 K, Gr, as judged by the narrow C 1s peak at 284.1 eV in the highest temperature spectrum in fig. 3.4.

In conclusion we were able to unambiguously identify all the molecular species involved in the temperature induced dissociation of ethylene on Ir(111) up to atomic C formation. Ethylene partly dissociate on the Ir(111) already at 90 K, since intact molecules are observed together with CH_2C species. Complete dissociation occurs only above 200 K. At higher temperature CH_2C dinamically hydrogenate back to CH_2CH which, due to the higher thermal energy, can dehydrogenate to form CHCH. CHCH is stable on the surface up to about 400 K and subsequently slowly converts to CH. Above 500 K the last dehydrogenation barrier is activated and atomic C starts to form on the surface.

3.2 Unravelling the roles of surface chemical composition and geometry for the graphene-metal interaction

As already pointed out in the introduction to this chapter, the interaction between epitaxial Gr and the TM substrate is strongly dependent on the TM choice. To date, there is still debate as to what determines the interaction strength between graphene and its metal substrate [14, 12]. One possibility is related to the mismatch between the lattice parameter of graphene and that of the underlying surface, which induces a different degree of re-hybridization on different C atoms, and is known to drive the formation of moiré superstructures [20]. The geometry of the metallic surface not only causes strain on graphene as its lattice parameter adapts to that of the substrate, but could also influence its electronic configuration. In fact, it has been demonstrated that graphene on Cu has a different degree of doping depending on the symmetry of the surface over which it has been grown [21]. On the other hand, one can quantify the interaction by extending the Hammer and Nørskov's model for the chemisorption of molecules on transition and nobel metal surfaces [22] to Gr/TM systems [23]. This model describes the bonding between molecules and d-band metals through the coupling between the valence band orbitals of the adsorbates and the metal d-band. This coupling is maximized when the orbitals of the molecules lie close in energy to the metal d-band center.

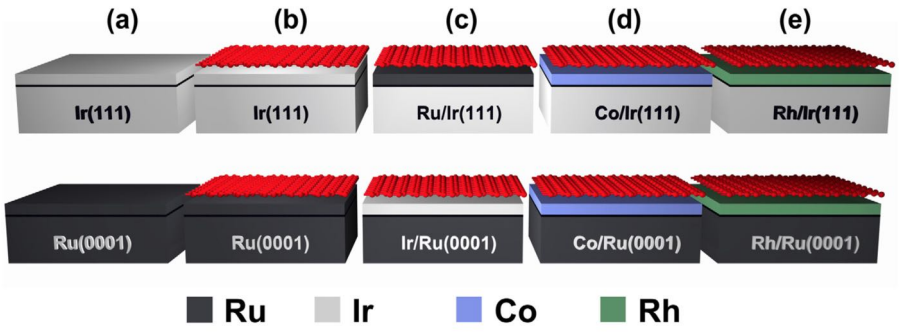

Figure 3.6: Schematic outline of the experimental procedure followed in this investigation. (a) Pristine Ir(111) (top row) and Ru(0001) (bottom row) surfaces. (b) Graphene growth on the two substrates. (c-e) Intercalation of different metallic species at the Gr/metal interfaces.

The primary aim of this combined experimental and theoretical investiga-

tion was to distinguish the contribution to the interaction between Gr and the TM substrate that arise from the geometrical (lattice mismatch) and chemical (elemental composition of the substrate) properties of the surface [24]. We have achieved this by systematic intercalation of different metallic species at Gr-metal interfaces, following the scheme reported in fig. 3.6. In fact, the intercalation process modifies the chemical composition of the first surface layer underneath Gr while preserving the geometrical arrangement of the substrate, provided that the intercalated layer is monoatomic thick. In order to make an extensive investigation in a reproducible and controlled way, we used two different single crystal close packed TM surfaces: Ir(111) and Ru(0001) which are known to be weakly and strongly interacting with Gr respectively. Both substrate have a lattice parameter (2.72 Å for Ir, and 2.70 Å for Ru) that is larger that that of Gr (2.46 Å). The intercalated species were also chosen to reflect different degree of interaction with Gr when the latter is grown on their hexagonal close packed surface. Beside Ru and Ir, we employed Rh, which exhibits an intermediate interaction strenght with Gr, and Co, which is even more strongly interacting than Ru.

HR-XPS was employed to study the electronic structure of the TM supported graphene layers. In fact, high energy resolution core level spectroscopy has proved particularly effective in determining the doping of weakly interacting Gr, since the energy shift of the core levels reflects that of the valence band [25]. Moreover, in the case of strongly interacting systems, chemical bonding between Gr and the substrate induces large shifts in C 1s the core level BE of Gr, which can be accurately measured with our setup.

Complementary extensive DFT calculations were performed by overlaying a Gr sheet over a (12$\times$12) and a (9$\times$9) supercell for Ru(0001) and Ir(111). The metal surfaces were modelled using a slab with a thickness of 5 layers, with the atoms of the 2 bottom layers kept fixed at their bulk positions, while all the other atoms were allowed to relax. By modifying the chemical species of the topmost metallic layer we were also able to model the systems obtained from the intercalation of metals below graphene. This approach allows to describe systems where a single layer of metal is intercalated below graphene with high accuracy. However, it does not take into account local defects which are unavoidable in real systems, such as vacancies or 3-dimensional islands composed of two (or more) layers of intercalated metal.

3.2.1 Experimental results

Gr was grown on Ir(111) and Ru(0001) by means of ethylene CVD. For the growth on Ir(111) a temperature programmed growth approach was adopted, consisting of repeated cycles of ethylene adsorption at room temperature up to surface saturation followed by annealing to 1400 K. In the case of Ru(0001), instead, the sample was kept at 1100 K in increasing ethylene pressure (up to $5 \cdot 10^{-8}$ mbar) until a single layer Gr was formed. Both methods lead to the formation of a high quality single layer of Gr with a low density of defects [26, 27, 28, 29, 30, 31].

A high resolution C 1s core level spectrum obtained after Gr growth on Ir(111) is presented in fig. 3.7 (a). The spectrum consists of a single narrow component (W) with a FWHM of 270 meV and a BE of 284.12 eV, which is the fingerprint of quasi free standing Gr [13, 28]. The small additional shoulder visible at higher BE is attributed to the presence of a small amount of defects in the C network.

The analysis of the C 1s core level spectrum for Gr grown on Ru(0001) is complicated by the overlap with the $3d_{3/2}$ core level of the substrate, as reported in fig. 3.9. To separate the two contributions, the Ru $3d_{3/2}$ core level had to be included in the analysis. To this purpose, the line shape of the Ru $3d_{3/2}$ level was constrained to the one obtained from clean Ru(0001) surface (not shown here), while its intensity was set proportional to that of the $3d_{5/2}$ level, with a proportionality constant obtained from the clean Ru spectrum. All the C 1s spectra presented for the various Gr/TM/Ru(0001) systems were analyzed according to this procedure and are reported after subtraction of the Ru $3d_{3/2}$ signal. The C 1s core level spectrum obtained for epitaxial Gr grown on Ru(0001) is reported in fig. 3.8 (a). The spectrum shows two distinct components: a weaker one (S3) at 284.47 eV, and a more intense and narrower one (S1) at 285.13 eV. The presence of two components reflects a broad distribution of non equivalent C atom configurations due to the lattice mismatch with the substrate, as discussed in the following section.

To check the quality and long range order of the Gr layers synthesized on the two substrates, we performed SPA-LEED measurements (see fig. 3.10). The diffraction images show narrow and sharp diffraction spots. From the analysis of the FWHM of Gr diffraction spots we can conclude that, in both cases, the average Gr domain size is comparable to the transfer width of the instrument. Moreover, the absence of additional diffraction spots, besides those arising from Gr, the substrate, and the moiré, clearly exclude the presence of other superstructures or rotational domains.

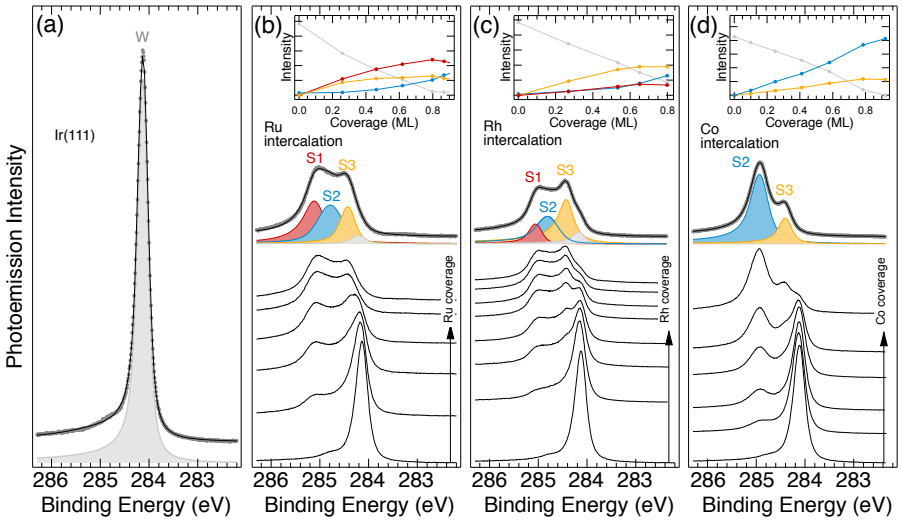

Figure 3.7: C 1s core level spectra of Gr/Ir(111) during intercalation (hv=385eV). (a) Pristine Gr/Ir(111). (b-d) Evolution of the C 1s spectrum during intercalation of (b) Ru, (c) Rh and (d) Co. Top graphs show the evolution of the area of all C 1s photoemission components corresponding to non-equivalent C populations at increasing intercalating metal coverages.

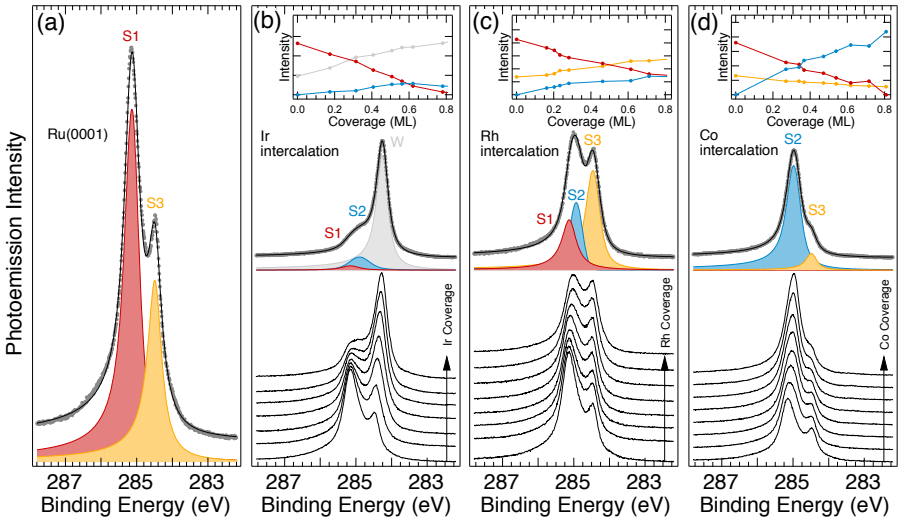

Figure 3.8: C 1s core level spectra of Gr/Ru(0001) during intercalation (hv=385eV). (a) Pristine Gr/ Ru(0001). (b-d) Evolution of the C 1s spectrum during intercalation of (b) Ir, (c) Rh and (d) Co. Top graphs show the evolution of the area of all C 1s photoemission components corresponding to non-equivalent C populations at increasing intercalating metal coverages.

The intercalation of each metal was obtained by evaporation while keeping the sample surface at 700 K. This temperature was chosen because it allows metal atoms to have enough mobility to diffuse above graphene, reach a suitable site for intercalation (mainly grain boundaries) and diffuse below the surface, while metallic species deposited at ambient temperature usually tend to form clusters on top of graphene. LEED measurements, acquired after each intercalation, confirmed that the lattice parameters were not modified, *i.e.* the intercalated layer was always pseudomorphic.

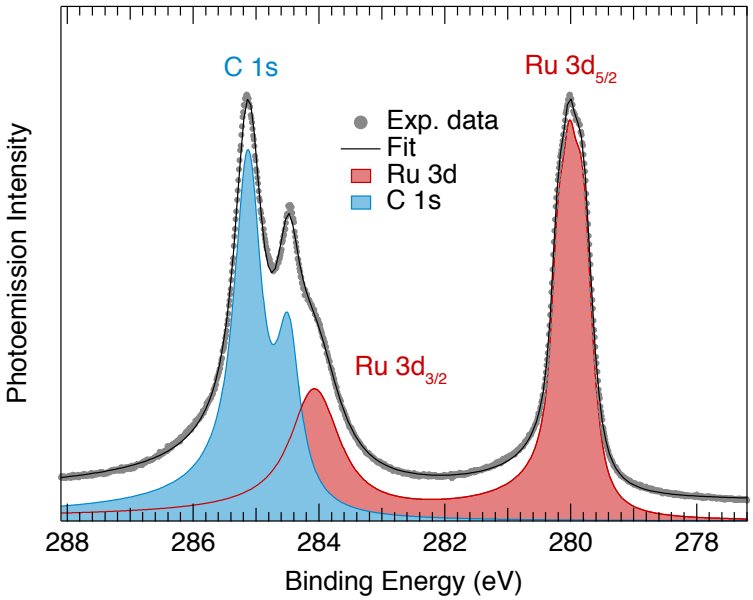

Figure 3.9: Ru 3d and C 1s high resolution photoemission spectrum acquired after Gr growth on Ru(0001) (hv = 385 eV). Experimental data (grey dots) are displayed along with the best fir result (black line). The blue spectrum represents the C 1s core level of Gr, while the red spectrum corresponds to the Ru 3d level.

In order to understand whether or not the deposited metal had completely intercalated below graphene, we compared the C 1s spectra before and after the metal deposition. In fact, a completely intercalated metal layer is reflected in an intensity loss in the photoemission signal generated by the substrate, due to photoelectron screening, whereas the photoemission intensity of graphene remains constant. On the other hand, if part of the metal atoms sit above graphene the photoemission intensity of graphene is screened as well. We did not observe any decrease in the C 1s spectral intensity after Ir, Ru, and Co deposition, indicating that, for these species, complete intercalation occurs. A small reduction of the graphene photoelectron intensity was however observed

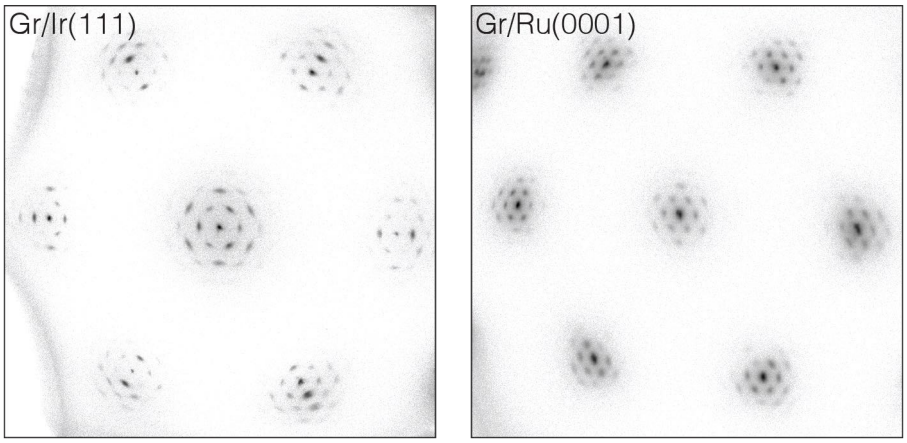

Figure 3.10: SPA-LEED diffraction patterns acquired after Gr synthesis on Ir(111) (left, 110 eV) and Ru(0001) (right, 250 eV).

after deposition of Rh, suggesting that a small amount of the deposited Rh does not intercalate, but rather form small aggregates above graphene.

Species	**BE$_{\mathrm{CLS}}$ (eV)**			
System	S1(eV)	S2(eV)	S3(eV)	W(eV)
Gr/Ir(111)	-	-	-	**284.12**
Gr/Ru/Ir(111)	**285.10**	284.75	284.41	-
Gr/Rh/Ir(111)	285.05	284.83	**284.42**	-
Gr/Co/Ir(111)	-	**284.93**	284.40	-
Gr/Ru(0001)	**285.13**	-	284.47	-
Gr/Ir/Ru(0001)	-	284.89	-	**284.23**
Gr/Rh/Ru(0001)	285.13	284.91	**284.47**	-
Gr/Co/Ru(0001)	-	**284.97**	284.47	-

Table 3.3: BE of each component of the C 1s core level photoemission spectrum in all systems studied in this work. The main component in the spectrum of each system is reported in bold.

Figure 3.7 and 3.8 shows the C 1s spectra acquired during and after intercalation of about 1 ML of each TM. All photoemission components of the C 1s core level which appear in any of the systems we analyzed are reported in Table 3.3, together with their BEs. The determination of the coverage (Θ) of the intercalated species was achieved by looking at the Ir $4f_{7/2}$ and Ru $3d_{5/2}$ spectra. In fact, these core levels shows distinct spectral features for bulk and surface atoms, due to the different coordination. As the intercalation proceeds, the

substrate surface atoms are covered by the intercalated metal, and therefore their local coordination environment becomes more and more bulk like. This implies that the spectral feature associated to these substrate surface atoms slightly decreases, eventually vanishing upon reaching about 1 ML of intercalated species. Following this approach, the intercalated species coverage can be expressed as:

$$\Theta = 1 - \frac{I(\Theta)}{I_0}$$

where $I(\Theta)$ is the intensity of the surface spectral component at the coverage Θ, and I_0 is the initial intensity. This approximation for calculating the coverage is rigorous provided that the intercalated metal does not form three dimensional islands, but rather a single epitaxial layer.

From the series of spectra acquired during each intercalation experiment (fig. 3.7 and 3.8), it is clear that the C 1s spectrum changes dramatically as the substrate is covered by the intercalated species. In order to accurately analyze the data, we first obtained the D-S lineshape parameters from the spectra corresponding to a 1 ML coverage of the intercalated species. The lineshape of each component was then assumed to be constant throughout each intercalation experiment. Small modifications of the Gaussian parameter were allowed in order to describe possible contributions due to structural inhomogeneities.

For all of the Gr/TM/Ir(111) systems (see fig. 3.7(b-d)) we observe a progressive decrease of the W component intensity upon intercalation. On the other hand, several components appear at higher BE, indicating a stronger degree of interaction between Gr and the substrate. The BE of these components does not depend on the coverage, only the relative intensities being modified throughout the experiment.

Specifically, after intercalation of Ru (fig. 3.7 (b)) we observe three high BE components (S1-3) lying between 284.41 and 285.10 eV. Besides the presence of the S2 component, the spectral distribution is quite similar to the one obtained for Gr synthesized on pristine Ru(0001) (3.8 (a), see also fig. 3.11 (b)), suggesting that the two systems have the same average interaction with the substrate. The presence of the additional S2 component in the core level spectrum of Gr/Ru/Ir(111) could be related to small differences in the Gr layer corrugation due to the different geometry of the two systems.

A similar behavior is observed after Rh evaporation on Gr/Ir(111) (3.7 (c)). Also in this case, besides the decreasing of the W component intensity, we observe a main component at 284.42 eV (S3) and two additional components (S1-2), with lower intensity, at higher BE. It is useful to stress that the BE of the S1 and S3 peaks are quite similar to the high and low BE components reported

for Gr grown on pristine Rh [32, 33], which are usually attributed to C atoms sitting in different position of the buckled Gr layer. Notably, Rh intercalation under Gr grown on Ru(0001) (fig. 3.8 (c)), produces almost the same spectral distribution in the C 1s core level spectrum (see also fig. 3.11 (c)), with the same S1-3 components in a similar ratio. Small differences in the spectral weight, as well as the presence of the additional S2 with respect to Gr synthesized directly on Rh, can be explained either in terms of small differences in the local C atoms configurations, or as due to the presence of a small amount of Rh cluster sitting on top the Gr layer, as discussed before. Finally, it is worth noticing that, even if we observe the same spectral components for the Gr/Rh and Gr/Ru systems, the different spectral weight, and in particular the higher intensity of the S3 component, indicates, on average, a lower Gr-metal interaction for the Gr-Rh interfaces.

For Co evaporation on Gr/Ir(111) (3.7 (d)), we obtained an intense component (S2) at 284.93 eV, and a weaker one (S3) at lower BE, indicating a generally strong interaction with the Co layer. A similar behavior is observed after the intercalation of Co below Gr/Ru(0001) (3.8 (d)), since the high BE component (S1) is replaced by a new one (S2), at a slightly lower BE. These two components are always distinct and their BE remains constant with increasing Co coverage. On the other hand, the low-BE component (S3) decreases: in general the spectral weight moves towards higher BE, indicating a slightly stronger interaction of Gr with Co than with Ru. Notably the final spectra for the two Gr/Co interfaces (see fig. 3.11 (d)) show almost the same spectral distribution, with small differences in the spectral weight most likely due to local differences or inhomogeneities.

Finally, intercalation of Ir under Gr grown on Ru(0001) (3.8 (b)) results in a spectrum dominated by a low BE component (W) at 284.23 eV, followed by a weaker shoulder (S2) at higher BE. This results indicates a strong reduction in the Gr-substrate interaction strength. The presence of the S2 component, which is not observed for Gr/Ir(111), can be explained in terms of Gr regions that are more strongly interacting with the substrate due to a different corrugation.

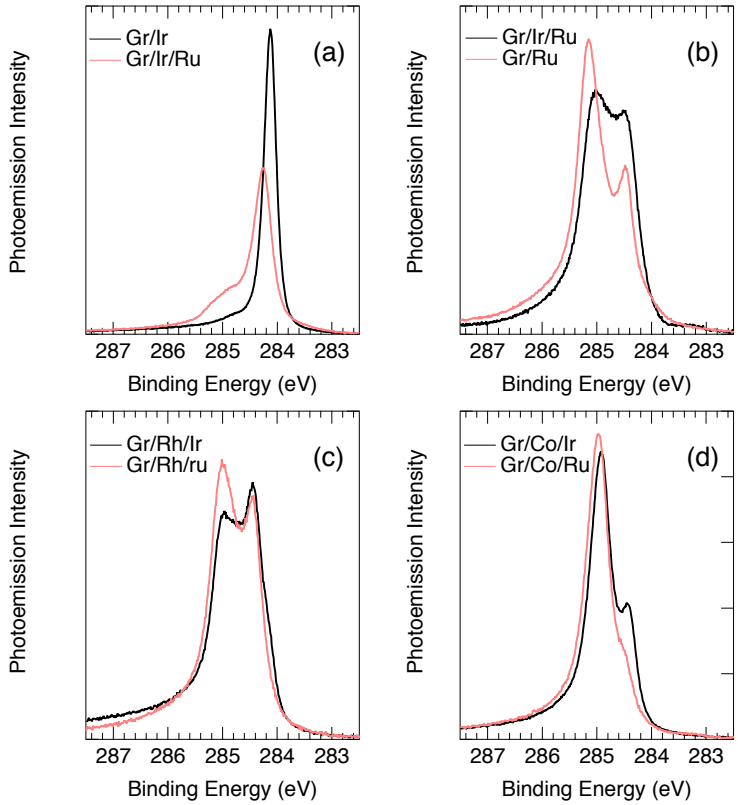

Figure 3.11: High resolution C 1s core level spectra (hv=385 eV) recorder for all the Gr/TM interfaces after intercalation of about 1 ML of each metallic species.

In conclusion, by comparing the two intercalation experiments on Ir(111) and Ru(0001), we observe that the C 1s core level spectrum of Gr (and therefore also its interaction with the substrate) show significant changes depending on the chemical composition of the topmost surface layer. A similar behavior is observed for the same Gr/TM interface, regardless of the substrate composition. In particular the Gr/Ir interface appears to be the most weakly interacting, followed by Rh and Ru. Only Co has an average interaction with Gr stronger than Ru.

3.2.2 Theoretical results

Figures 3.12 and 3.13 report the DFT computed minimum-energy geometric configuration for all the systems studied in this experiment. The color scale indicates the vertical distance (z) of each carbon atom from the surface plane of the metallic substrate. The metallic substrate itself is actually corrugated

when it strongly interacts with graphene. This corrugation, however, is an order of magnitude lower than that of graphene. For this reason, the vertical distance has been referred to the average vertical position of all atoms composing the metallic surface.

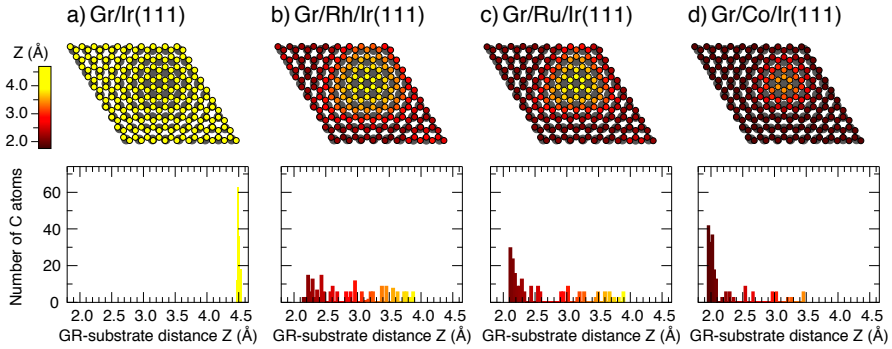

Figure 3.12: DFT results for different Gr/TM/Ir(111) interfaces. Top panels: geometric configuration of the topmost metallic atoms (large, gray circles) and of the graphene atoms (smaller, colored circles) inside the (9×9) moiré unit cell used for calculations. The color scale indicates the C-to-surface distance (z). Bottom panels: distribution of distance z for all the C atoms in the moiré unit cell.

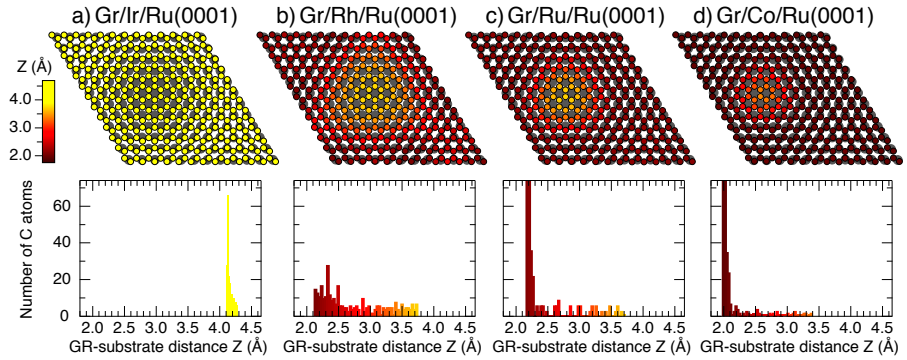

Figure 3.13: DFT results for different Gr/TM/Ru(0001) interfaces. Top panels: geometric configuration of the topmost metallic atoms (large, gray circles) and of the graphene atoms (smaller, colored circles) inside the (12×12) moiré unit cell used for calculations. The color scale indicates the C-to-surface distance (z). Bottom panels: distribution of distance z for all the C atoms in the moiré unit cell.

For all systems, graphene's geometrical properties strongly depend on the chemical composition of the topmost substrate layer. In particular, where the interaface layer consists of Ir (Figs. 3.12 and 3.13 (a)), the distance between Gr and the substrate is larger than 4 Å and the former exhibits a small corruga-

tion. This is in contrast with all other systems, where the Gr-substrate distance distribution is much wider, with the nearest atoms closer than 2 Å to the surface and the farthest between up to 3.9 Å. For all systems, the C atoms which are farthest from the surface are those which belong to a unit cell with the center of the honeycomb close to a top site of the substrate, and therefore lie in hollow sites. On the other hand, the C atoms which are found closest to the substrate are those belonging to a unit cell where the center of the honeycomb lies in bridge sites, and therefore lie in a top position.

In particular, for the Gr/Rh/Ir(111) and Gr/Rh/Ru(0001) systems we observe a quite uniform distribution in the Gr-surface distance, which ranges from 2.1 to 3.9 Å in the case Gr/Rh/Ir(111) (fig. 3.12 (b)), and from 2.1 to 3.7 Å for Gr/Rh/Ru(0001) (fig. 3.13 (b)), suggesting a smooth corrugation of the Gr layer in these cases.

On the other hand, the two Gr/Ru interfaces show a rougher corrugation. Specifically, a large amount of the C atoms lie close to the surface (between 2.1 and 2.3 Å). The others, which are more than 25% in the case of Gr/Ru(0001) and almost 50% for Gr/Ru/Ir(111), are found at a much higher distance, up to 3.7 and 3.9 Å respectively (fig. 3.12 and 3.13 (c)). The higher number of C atoms which lie close to the surface with respect to the Gr/Rh case indicates a average stronger interaction, in agreement to what deduced from the XPS data.

Finally, the distribution along z of the C atoms above a Co layer (fig. 3.12 and 3.13 (d)) has a very sharp peak at low z values (between 1.9 and 2.1 Å), with only few atoms laying farther that 2.1 Å from the surface (and up to 3.5 Å). This observation supports the hypothesis, based on XPS data, that the average Gr-surface interaction is stronger for Co with respect to the other investigated systems.

The calculated distance distribution for the two Gr/Ru interfaces is in good agreement with experimental values found for Gr grown on Ru(0001) [34]. This is also the case for Gr sitting on intercalated Co on Ir(111), which is in very good agreement with previous experiments on the same system [35]. Moreover, the z value of about 2 Å found for the majority of atoms in both systems corresponds to the height found for Gr above Co(0001), where Gr matches the lattice of the surface forming a 1×1 commensurate structure [36]. The two Gr/Rh interfaces have the same corrugation as Gr synthesized on pristine Rh(111) [14, 37]. The separation of Gr from Ir for the two Gr/Ir systems appears instead to be overestimated, being even larger than the inter-layer distance of graphite by about 1Å.This can be attributed to the presence of dispersive forces

which are not included in the present calculations [38] and which are probably not negligible in this case.

To get further details on the electronic configuration of the different Gr/TM interfaces we computed the core level BEs for all C atoms of all the systems. Since DFT methods only provide the relative value of the C 1s BEs for non equivalent atoms, we had to align the theoretical BE scale to the experimental one. To this purpose we firstly aligned the center of the calculated BE distribution for Gr/Ir(111) to the actual experimental value, and then shifted the theoretical BE scale for all systems by the same offset. This choice was motivated by the fact that the Gr/Ir(111) displays both the narrowest experimental spectrum and theoretical BE distribution, thus minimizing the error in the alignment.

The DFT computed C 1s core level BEs for the C atoms inside the moiré unit cell for the investigate systems are reported in figs. 3.14 and 3.15. A different behavior of the C 1s BE distribution can be observed for different chemical compositions of the substrate's topmost layer, regardless of its geometry. Graphene lying on top of Ir has a narrow BEs distribution centered at about 284.20 eV for Gr/Ir(111) (fig. 3.14 (a) and at about 284.27 eV for the intercalated systems (fig. 3.15 (a)), in good agreement with the experimental XPS data that show a main component (W) at 284.12 and 284. 23 eV BE respectively.

On the other hand, the BE distribution for the other investigated systems is much broader. In fact, the calculated BEs for the Ru, Rh, and Co interfaces range from about 284.4 eV up to, for Gr/Ru/Ir(111), 285.5 eV. What differs among these corrugates systems is the shape of the BE distribution, which is different depending on the topmost layer. Both the Gr/Ru and the Gr/Rh systems (figs. 3.14 and 3.15 (b,c)) display a smooth BE distribution with a similar BE range, but a higher density of C atoms with higher BE is observed for Ru, once more suggesting that the interaction of Gr with the substrate is, on average, stronger for Ru with respect to Rh. Again, the BE distribution is in good agreement with the experimental XPS spectra.

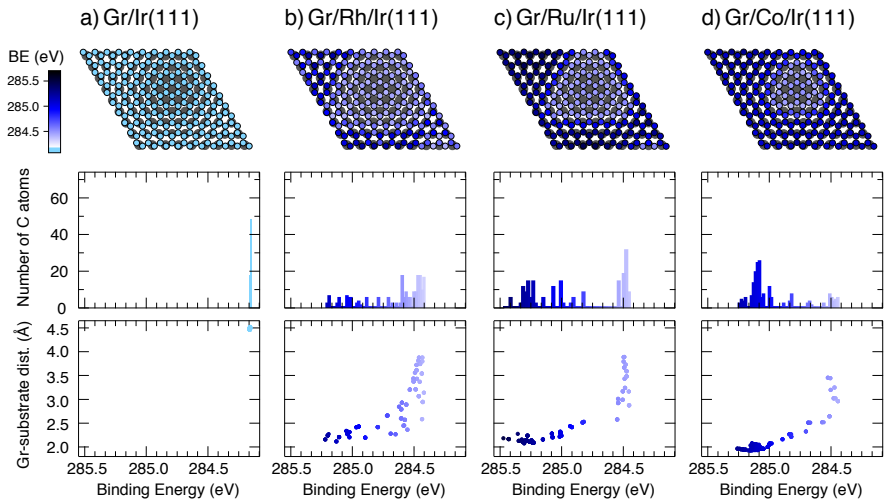

Figure 3.14: DFT results for different Gr/TM/Ir(111) systems. Top panels: the calculated C 1s core level BE is represented for each C atom (small dots) in the moiré cell using a color scale. The larger, gray circles represent the underlying metallic atoms. Middle panels: Distribution of BEs for all C atoms. Bottom panels: correlation between C 1s BE and separation of each atom from the topmost metallic layer.

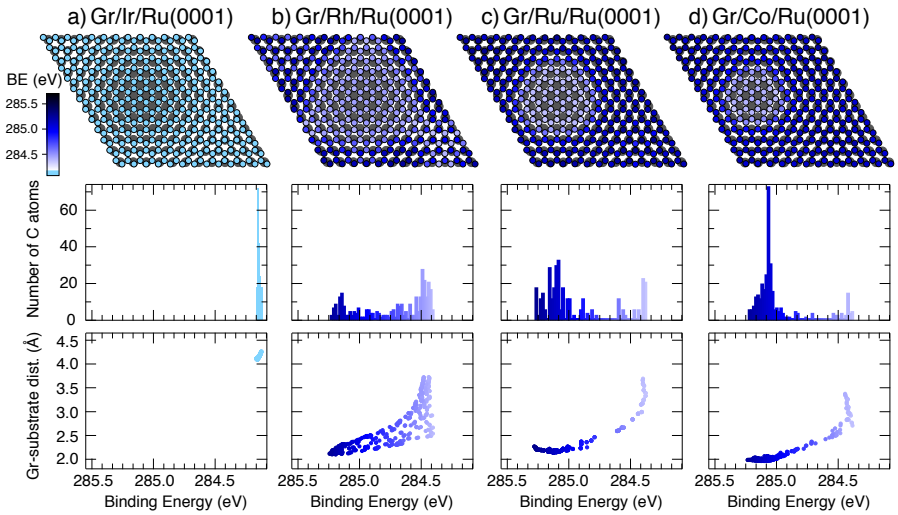

Figure 3.15: DFT results for different Gr/TM/Ru(0001) systems. Top panels: the calculated C 1s core level BE is represented for each C atom (small dots) in the moiré cell using a color scale. The larger, gray circles represent the underlying metallic atoms. Middle panels: Distribution of BEs for all C atoms. Bottom panels: correlation between C 1s BE and separation of each atom from the topmost metallic layer.

Finally, the BE distributions for C atoms belonging to Gr/Co interfaces present a sharp peak around 285.1 eV, with only around 15% of the C atoms having a C 1s BE lower than 284.7eV. This actually reflects the C 1s core level spectra, in which the main contribution was given by the S2 peak at about 285 eV BE.

As it can be observed in the bottom graphs in figs. 3.14 and 3.15, there is usually a correlation between the distance of each C atom from the underlying surface and its C 1s BE, with the latter decreasing as the former increases. This dependency is less evident for the case of Gr on Rh, where some adjacent atoms, despite being at the same distance from the substrate, show a large difference (up to 500 meV) in the C 1s BE. In this case, in fact, the BE of each atom is strongly influenced by its adsorption site on the surface. This particular behavior has already been observed for epitaxial Gr on Rh(111) and has been explained in terms of a different hybridization of the π states of Gr with the d bands of Rh [39]. The dependency of the BE on the site is weaker for atoms either too close to the surface (around 2 Å) or too far (above 3 Å).

In order to further confirm the agreement between the experimental C 1s core level spectra and the DFT computes C 1s BEs, we compared the barycenter of each calculated BE distribution with that of the corresponding experimental spectrum. The results are reported in fig. 3.16, where the experimental and theoretical C 1s barycenter are plotted together versus the calculated d-band centre of the topmost metallic layer. In most systems, the experimental C 1s spectrum barycenter value (round markers) agrees with the calculated ones (square markers), within an uncertainty of 40 meV. The only cases where we found a slightly worse agreement were the Gr/Rh systems and the one obtained by intercalating Ru at the Gr/Ir(111) interface. All these systems were characterized by a higher disorder. In particular, in the first two cases, the reason can be ascribed to the fact that a small portion of Rh atoms were not completely intercalated but most likely formed clusters on the graphene surface.

Besides the very good agreement between experiment and theory, we found a strong linear relationship between C 1s spectral center of mass and calculated d-band centers. Indeed, as firstly pointed out by Wang *et al* [40], and more recently extensively described by Toyoda *et al.* [41], the interaction between the d-band of TM metals and Gr potential energy surface strongly influence the adsorption properties of Gr. Although core level BEs are affected by final-state contributions that are intrinsic to the photoemission process, their contribution does not obscure this linear relationship. This offers a further proof that core level spectroscopy can be considered a useful experimental descriptor of the interaction strength of graphene with transition metal surfaces.

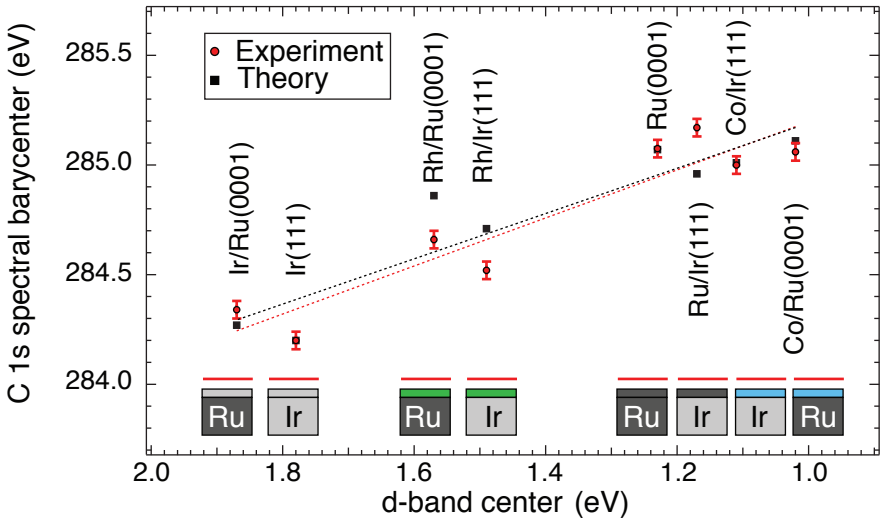

Figure 3.16: Theoretical (black squares) and experimental (red circles) values of the C 1s core-level BE distribution's barycentre of all C atoms in the moiré unit cell, for each system studied in this work, versus the calculated d-band centre of the underlying clean metal surface.

To complete the characterization of the investigated systems, we computed the average distance of each C atom from its three nearest neighbors for all the investigated systems. As reported in figs. 3.17 and 3.18, the C-C distance distribution inside the moiré cell is strongly influenced by the geometry of the substrate.

In particular, in the case of Gr supported by Ir, the nearest neighbor distance is the same for all C atoms: 1.45 Å for Gr/Ir/Ru(0001) and 1.42 Å for Gr grown on pristine Ir(111). Notably, the latter corresponds to the nearest neighbor distance of free standing Gr, while the former is large. This could be due to the fact that, when Gr is grown on Ru(0001), the interaction with the substrate induces a strain in the Gr layer in order to form a commensurate moiré lattice, while in the case of Gr on Ir(111) the interaction with the substrate is too weak to significantly modify the geometry of Gr. Graphene geometrical arrangement is preserved upon intercalation, otherwise it would require breaking or a strong rippling of the strong in plane C-C bonds. For this reason, in all systems modeled after the geometry of Ru(0001) the distribution of C-C distances is shifted towards higher values with respect to that of the systems modeled on Ir(111). This additional strain could also account for the small differences in the C 1s BEs which were observed for the same topmost layer chemical composition.

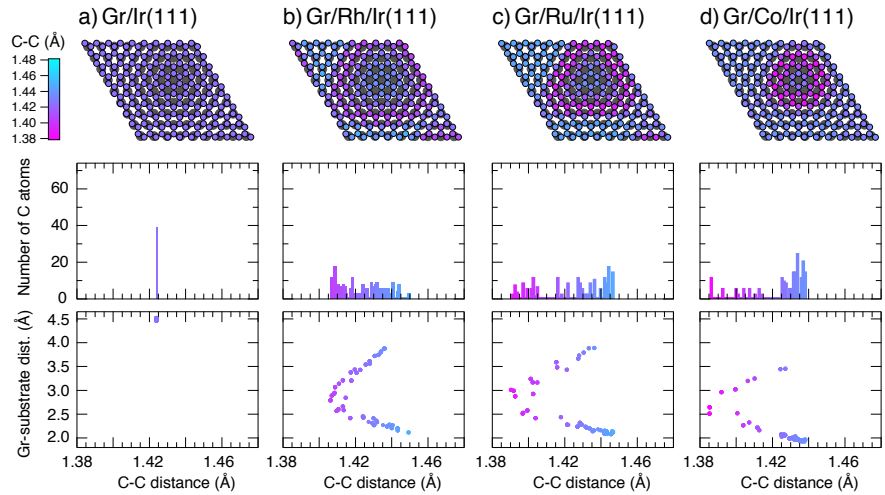

Figure 3.17: DFT results for different Gr/TM/Ir(111) systems. Top panels: geometric configuration of the topmost metallic atoms (large, gray circles) and of the graphene atoms (smaller, colored circles) inside the moiré cell. The color scale indicates the average distance of each C atom from its three nearest neighbors. Middle panels: Distribution of C-C distances of all C atoms. Bottom panel: correlation between C-C distance and separation of each atom from the topmost metallic layer.

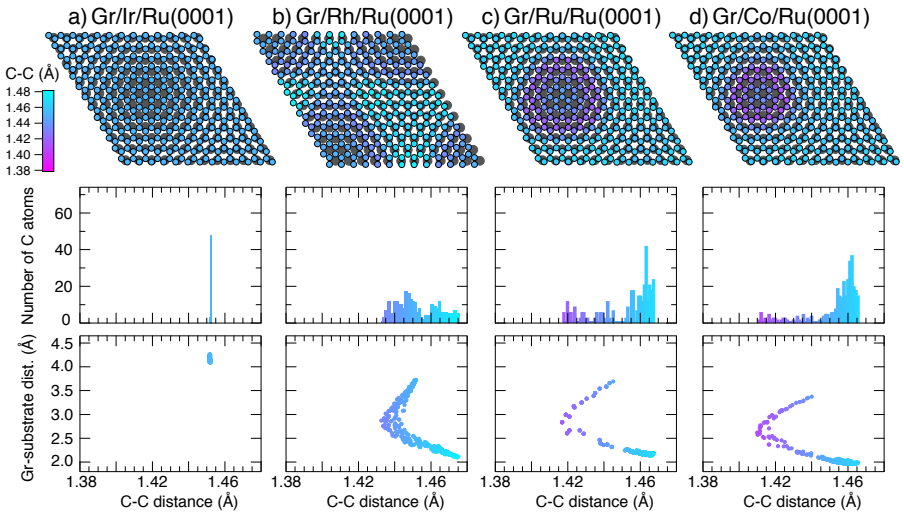

Figure 3.18: DFT results for different Gr/TM/Ru(0001) systems. Top panels: geometric configuration of the topmost metallic atoms (large, gray circles) and of the graphene atoms (smaller, colored circles) inside the moiré cell. The color scale indicates the average distance of each C atom from its three nearest neighbors. Middle panels: Distribution of C-C distances of all C atoms. Bottom panel: correlation between C-C distance and separation of each atom from the topmost metallic layer.

Corrugated systems show a broader C-C distance distribution. For Gr/Rh systems (figs. 3.17 and 3.18 (b)) the nearest neighbor distance displays a smooth distribution ranging from 1.41 to 1.45 Å in the case of Ir(111), and from 1.43 to 1.48 Å in the case of Ru(0001). Gr/Ru and Gr/Co show a similar C-C distance distribution, but both displays a sharp peak towards higher values. Also for these systems, the nearest neighbor distance is, on average, larger for Ru(0001) based geometries.

By studying the correlation between the C-C separation, the position inside the moiré cell (fig. 3.17 and 3.18, top panel), and to the distance from the substrate (fig. 3.17 and 3.18, bottom panel), it can be noticed that the C-C distance is usually minimum on the edges of the hills, whereas it is larger in the flat areas both on top of them and at the bottom of the valleys.

To conclude, by combining HR-XPS and DFT results, we observed that the Gr-metal interaction strength is mainly driven by the chemical composition of the interface. Both the experimental core level spectra and the computed C 1s BEs showed similar spectroscopic features and a comparable BE distribution for the same Gr/TM systems, regardless of the substrate. For example, the intercalation of Ir on Gr/Ru(0001) leads to a very weakly interacting Gr, as for graphene/Ir(111), while intercalation of Ru below Gr/Ir(111) leads to stronger interaction with the substrate, resulting in a buckling of the Gr layer. Geometry, on the other hand, mainly determines the periodicity of the moiré, which is preserved after intercalation. This is particularly obvious if we consider the case of Gr interacting with Co: it is flat and commensurate on Co(0001), while it is buckled in the case of the Co intercalation. Moreover, the geometrical sorting of the substrate strongly influence the local arrangement of the C atoms, in particular inducing a different degree of strain depending on the substrate lattice. Small variations in the core level spectra could be related to this latter point. Finally, we have verified that the C 1s spectral barycentre has a linear relationship with the d-band centre position of the substrate, which is recognized to strongly influence the coupling between Gr and the metal surface. We have therefore demonstrated that C 1s core level spectra contain relevant information on Gr-metal interfaces and can be considered a reliable descriptor of the Gr-substrate interaction strength.

Bibliography

[1] I. Pletikosić, M. Kralj, P. Pervan, R. Brako, J. Coraux, A. T. N'Diaye, C. Busse, and T. Michely. Dirac cones and minigaps for graphene on Ir(111). *Physical Review Letters*, **102**(5):056808, 2009.

[2] C. Busse, P. Lazić, R. Djemour, J. Coraux, T. Gerber, N. Atodiresei, V. Caciuc, R. Brako, A. T. N'Diaye, S. Blügel, J. Zegenhagen, and T. Michely. Graphene on Ir(111): physisorption with chemical modulation. *Physical Review Letters*, **107**(3):036101, 2011.

[3] P. W. Sutter, J. I. Flege, and E. A. Sutter. Epitaxial graphene on ruthenium. *Nature Materials*, **7**(5):406–411, 2008.

[4] M. Sicot, S. Bouvron, O. Zander, U. Rüdiger, Y. S Dedkov, and M. Fonin. Nucleation and growth of nickel nanoclusters on graphene Moiré on Rh(111). *Applied Physics Letters*, **96**(9):093115, 2010.

[5] P. Sutter, J. T Sadowski, and E. Sutter. Graphene on Pt(111): Growth and substrate interaction. *Physical Review B*, **80**(24):245411, 2009.

[6] E. Miniussi, M. Pozzo, A. Baraldi, E. Vesselli, R. R. Zhan, G. Comelli, T. O. Menteş, M. A. Niño, A. Locatelli, S. Lizzit, and D. Alfé. Thermal stability of corrugated epitaxial graphene grown on Re(0001). *Physical Review Letters*, **106**(21):216101, 2011.

[7] A. Varykhalov, J. Sánchez-Barriga, A. M. Shikin, C. Biswas, E. Vescovo, A. Rybkin, D. Marchenko, and O. Rader. Electronic and magnetic properties of quasifreestanding graphene on Ni. *Physical Review Letters*, **101**(15):157601, 2008.

[8] J. Lahiri, T. Miller, L. Adamska, I. I Oleynik, and M. Batzill. Graphene growth on Ni (111) by transformation of a surface carbide. *Nano Letters*, **11**(2):518–522, 2010.

[9] A. Varykhalov and O. Rader. Graphene grown on Co(0001) films and islands: Electronic structure and its precise magnetization dependence. *Physical Review B*, **80**(3):035437, 2009.

[10] X. Li, W. Cai, J. An, S. Kim, J. Nah, D. Yang, R. Piner, A. Velamakanni, I. Jung, E. Tutuc, S. K. Banerjee, L. Colombo, and R. S. Ruoff. Large-area synthesis of high-quality and uniform graphene films on copper foils. *Science*, **324**(5932):1312–1314, 2009.

[11] S. Lizzit and A. Baraldi. High-resolution fast X-ray photoelectron spectroscopy study of ethylene interaction with Ir(111): From chemisorption to dissociation and graphene formation. *Catalysis Today*, **154**(1):68–74, 2010.

[12] J. Wintterlin and M. L. Bocquet. Graphene on metal surfaces. *Surface Science*, **603**(10):1841–1852, 2009.

[13] A. B. Preobrajenski, M. L. Ng, A. S. Vinogradov, and N. Mårtensson. Controlling graphene corrugation on lattice-mismatched substrates. *Physical Review B*, **78**(7):073401, 2008.

[14] M. Batzill. The surface science of graphene: Metal interfaces, CVD synthesis, nanoribbons, chemical modifications, and defects. *Surface Science Reports*, **67**(3):83–115, 2012.

[15] M. B. Hugenschmidt, P. Dolle, J. Jupille, and A. Cassuto. Ethylene π species on bare and cesiated Pt(111) surfaces. *Journal of Vacuum Science & Technology A*, **7**(6):3312–3316, 1989.

[16] A. Baraldi, G. Comelli, S. Lizzit, D. Cocco, G. Paolucci, and R. Rosei. Temperature programmed X-ray photoelectron spectroscopy: a new technique for the study of surface kinetics. *Surface Science*, **367**(3):L67–L72, 1996.

[17] P. Lacovig, M. Pozzo, D. Alfé, P. Vilmercati, A. Baraldi, and S. Lizzit. Growth of dome-shaped carbon nanoislands on Ir(111): the intermediate between carbidic clusters and quasi-free-standing graphene. *Physical Review Letters*, **103**(16):166101, 2009.

[18] J. N. Andersen, A. Beutler, S. L. Sorensen, R. Nyholm, B. Setlik, and D. Heskett. Vibrational fine structure in the C 1s core level photoemission of chemisorbed molecules: ethylene and ethylidyne on Rh(111). *Chemical Physics Letters*, **269**(3):371–377, 1997.

[19] H. P. Steinrück, T. Fuhrmann, C. Papp, B. Tränkenschuh, and R. Denecke. A detailed analysis of vibrational excitations in x-ray photoelectron spectra of adsorbed small hydrocarbons. *The Journal of Chemical Physics*, **125**(20):204706, 2006.

[20] P. Merino, M. Švec, A. L. Pinardi, G. Otero, and J. A. Martín-Gago. Strain-driven moiré superstructures of epitaxial graphene on transition metal surfaces. *ACS Nano*, **5**(7):5627–5634, 2011.

[21] O. Frank, J. Vejpravova, V. Holy, L. Kavan, and M. Kalbac. Interaction between graphene and copper substrate: The role of lattice orientation. *Carbon*, **68**:440–451, 2014.

[22] B. Hammer and J. K. Nørskov. Theoretical surface science and catalysis calculations and concepts. *Advances in Catalysis*, **45**:71–129, 2000.

[23] K. Toyoda, K. Nozawa, N. Matsukawa, and S. Yoshii. Density functional theoretical study of graphene on transition-metal surfaces: the role of metal d-band in the potential-energy surface. *The Journal of Physical Chemistry C*, **117**(16):8156–8160, 2013.

[24] F. Presel, N. Jabeen, M. Pozzo, D. Curcio, L. Omiciuolo, P. Lacovig, S. Lizzit, D. Alfè, and A. Baraldi. Unravelling the roles of surface chemical composition and geometry for the graphene–metal interaction through C1s core-level spectroscopy. *Carbon*, **93**:187–198, 2015.

[25] A. Dahal, R. Addou, H. Coy-Diaz, J. Lallo, and M. Batzill. Charge doping of graphene in metal/graphene/dielectric sandwich structures evaluated by C-1s core level photoemission spectroscopy. *APL Materials*, **1**(4):042107, 2013.

[26] J. Coraux, A. T. N'Diaye, C. Busse, and T. Michely. Structural coherency of graphene on Ir (111). *Nano Letters*, **8**(2):565–570, 2008.

[27] A. T. N'Diaye, S. Bleikamp, P. J. Feibelman, and T. Michely. Two-dimensional Ir cluster lattice on a graphene moiré on Ir(111). *Physical Review Letters*, **97**(21):215501, 2006.

[28] R. Larciprete, S. Ulstrup, P. Lacovig, M. Dalmiglio, M. Bianchi, F. Mazzola, L. Hornekær, F. Orlando, A. Baraldi, Ph. Hofmann, and S. Lizzit. Oxygen switching of the epitaxial graphene–metal interaction. *ACS Nano*, **6**(11):9551–9558, 2012.

[29] S. Gunther, S. Danhardt, B. Wang, M. L. Bocquet, S. Schmitt, and J. Wintterlin. Single terrace growth of graphene on a metal surface. *Nano Letters*, **11**(5):1895–1900, 2011.

[30] A. L. Vázquez De Parga, F. Calleja, B. M. C. G. Borca, M. C. G. Passeggi Jr, J. J. Hinarejos, F. Guinea, and R. Miranda. Periodically rippled graphene: growth and spatially resolved electronic structure. *Physical Review Letters*, **100**(5):056807, 2008.

[31] S. Lizzit, R. Larciprete, P. Lacovig, M. Dalmiglio, F. Orlando, A. Baraldi, L. Gammelgaard, L. Barreto, M. Bianchi, E. Perkins, and Ph. Hofmann. Transfer-free electrical insulation of epitaxial graphene from its metal substrate. *Nano Letters*, **12**(9):4503–4507, 2012.

[32] K. Gotterbarm, W. Zhao, O. Höfert, C. Gleichweit, C. Papp, and H. P. Steinrück. Growth and oxidation of graphene on Rh (111). *Physical Chemistry Chemical Physics*, **15**(45):19625–19631, 2013.

[33] B. Casarin, A. Cian, Z. Feng, E. Monachino, F. Randi, G. Zamborlini, M. Zonno, E. Miniussi, P. Lacovig, S. Lizzit, and A. Baraldi. The Thinnest Carpet on the Smallest Staircase: The Growth of Graphene on Rh (533). *The Journal of Physical Chemistry C*, **118**(12):6242–6250, 2014.

[34] W. Moritz, B. Wang, M. L. Bocquet, T. Brugger, T. Greber, J. Wintterlin, and S. Günther. Structure determination of the coincidence phase of graphene on Ru(0001). *Physical Review Letters*, **104**(13):136102, 2010.

[35] D. Pacilé, S. Lisi, I. Di Bernardo, M. Papagno, L. Ferrari, M. Pisarra, M. Caputo, S. K. Mahatha, P. M. Sheverdyaeva, P. Moras, P. Lacovig, S. Lizzit, A. Baraldi, M. G. Betti, and C. Carbone. Electronic structure of graphene/Co interfaces. *Physical Review B*, **90**(19):195446, 2014.

[36] D. Eom, D. Prezzi, K. T. Rim, H. Zhou, M. Lefenfeld, S. Xiao, C. Nuckolls, M. S. Hybertsen, T. F. Heinz, and G. W. Flynn. Structure and electronic properties of graphene nanoislands on Co(0001). *Nano Letters*, **9**(8):2844–2848, 2009.

[37] E. Voloshina and Y. Dedkov. Graphene on metallic surfaces: problems and perspectives. *Physical Chemistry Chemical Physics*, **14**(39):13502–13514, 2012.

[38] I. Hamada and M. Otani. Comparative van der Waals density-functional study of graphene on metal surfaces. *Physical Review B*, **82**(15):153412, 2010.

[39] B. Wang, M. Caffio, C. Bromley, H. Fruchtl, and R. Schaub. Coupling epitaxy, chemical bonding, and work function at the local scale in transition metal-supported graphene. *ACS Nano*, **4**(10):5773–5782, 2010.

[40] B. Wang, M. L. Bocquet, S. Marchini, S. Günther, and J. Wintterlin. Chemical origin of a graphene moiré overlayer on Ru(0001). *Physical Chemistry Chemical Physics*, **10**(24):3530–3534, 2008.

[41] K. Toyoda, K. Nozawa, N. Matsukawa, and S. Yoshii. Density functional theoretical study of graphene on transition-metal surfaces: the role of metal d-band in the potential-energy surface. *The Journal of Physical Chemistry C*, **117**(16):8156–8160, 2013.

4 Graphene Oxide Interfaces

The coupling of Gr with dielectric materials is a hot topic in contemporary material science [1, 2, 3], in the view of Gr integration into device architectures [4]. Gr can be used, for example, for the production of Gr-based Field Effect Transistors (GFETs) [5, 6, 7], with very high operational switching frequency, thanks to Gr high charge carrier mobility. In a typical GFET, Gr is used as channel material (see fig. 4.1) and, like in conventional FETs, must be electrically decoupled from the back (or top) gate by means of a thin oxide film (typically SiO_2 or Al_2O_3). Another example is given by Gr-base supercapacitors [8, 9, 10, 11], where the large specific surface area and the extremely high electronic conductivity of Gr could lead to possible improvement in the energy storage technology.

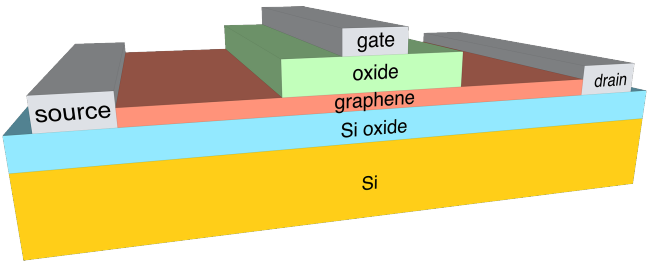

oxide	dielectric constrant
SiO_2	3.9
Al_2O_3	9
$HfSiO_4$	11
HfO_2	25
ZrO_2	25
Ta_2O_5	27
La_2O_3	30
$LaAlO_3$	30
Nb_2O_5	35
TiO_2	30-40 (Anatase) 80-100 (Rutile)

Figure 4.1: (left) schematics of a typical Gr transistor and (right) relative dielectric constant values for common oxides.

The most exploited method to produce Gr-oxide interfaces is, by far, the transfer of epitaxially grown Gr from the transition metal substrate onto an insulating material. Large scale Gr synthesis is usually achieved by means of hydrocarbon CVD on a transition metal substrate, like copper. Once a single layer is grown, Gr is spin coated with an intermediate medium, usually consisting of a plastic polymer like the Poly(methyl methacrylate) (PMMA). The metallic substrate is then removed by chemical etching. Finally, the Gr layer is transferred onto the insulating material and the polymer matrix is dissolved in acetone. This process, however, usually introduces impurities and defects in

the Gr layer, such as vacancies, grain boundaries and multilayers [12], which are reflected in a degradation of its electronic properties.

The direct growth of graphene on top of oxide surfaces, has also been tested [13, 14, 15]. These methods, however, pose a series of difficulties, such as the need for very high temperatures, can hardly discriminate between mono- and multi-layer graphene, and often results in Gr layers strongly interacting with the oxide substrate.

On the other hand, atomic layer deposition, used to directly synthesize oxide layers on top of Gr, typically requires a chemical modification of Gr to avoid wetting problems, and introduces impurities or causes C-C bond cleavages, leading to a significant degradation of the electron mobility. Recently, the direct synthesis of an Y_2O_3 layers on top of epitaxial Gr grown on Pt(111) has proved very successful [16], but, in this case, Gr is still electrically coupled to the transition metal substrate.

Part of my PhD research project was therefore devoted to the investigations of Gr-oxide interfaces. Here, two different important results for the synthesis and the functionalization of such interfaces are introduced and discussed. In the first part a transfer free method for the synthesis of graphene-alumina nanosheet interfaces is presented. Aluminum oxide (Al_2O_3, or alumina) films, in fact, play a key role in the electronic industry due to their employment as high-k oxides in high-frequency transistor and low-power chips, where a high dielectric constant is needed to maximize the gate capacitance, and a high dielectric strength is vital in order to avoid electrical breakthrough[1] (see also fig. 4.1). Moreover, it has been proved that exfoliated Gr on Al_2O_3 has a high mobility [17, 18] (up to 23,600 cm^2 V^{-1} s^{-1}).

In the second part, a novel method for the controllable chemical gating of epitaxial graphene is presented. Chemical gating is achieved by exploiting the electrostatic polarization of a ultrathin SiO_2 layer synthesized below it, due to intercalated oxygen diffusing through the SiO_2 layer which modifies the metal-oxide work function and hole dopes graphene.

[1] The dielectric constant of α-alumina is $\epsilon_r = 9.1$, while its dielectric strength is about 16.7 kV/mm.

4.1 Graphene-Alumina Nanosheet Interfaces

In this section, a novel method for the direct synthesis of high quality Gr-alumina interfaces, developed during my research work, is described [19]. Starting from a clean $Ni_3Al(111)$ surface (fig. 4.2 (a)), a single layer of Gr is grown by means of ethylene CVD (fig. 4.2 (b)). Subsequently, the interfacial aluminum atoms are oxidized in such a way to induce the formation of an alumina nanosheet below graphene (fig. 4.2 (c)).

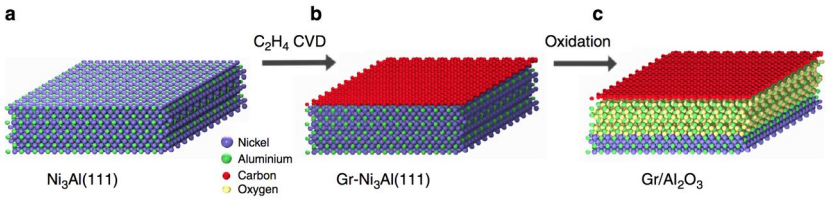

Figure 4.2: Schematic outline of Gr-alumina interface synthesis method: (a) The clean $Ni_3Al(111)$ surface, (b) Gr synthesis by means of high temperature ethylene CVD, and (c) selective oxidation of the interface Al atoms.

LEED measurements presented in this chapter were acquired at the Surface Science Laboratory, XPS and valence band photoemission data were collected at the SuperESCA and at the SGM3 beamlines respectively, while LEEM and μ-LEED data were acquired at the Nanospectroscopy beamline. Additional DFT calculations were performed by a collaborating group headed by Prof. D. Alfé at University College London (UK).

4.1.1 Characterization of the clean $Ni_3Al(111)$ surface

Ni_3Al is a stoichiometric bulk alloy of nickel and aluminum which crystallizes in a face centered cubic (FCC) lattice.The experimentally obtained lattice parameter is 3.56 Å [20]. The (111) surface does not reconstruct and presents an Al-Al distance of 4.9 Å [21]. First-to-second and second-to-third layer distances are also known to be 1.99 and 2.02 Å respectively, to be compared with the bulk value of 2.05 Å. Moreover, it has been shown that the outermost Al atoms are pushed forward from the plane formed by Ni atoms by 0.15 Å. A very low density of surface defects is finally reported in literature [20]: in fact, variations from the stoichiometric composition were found, but the maximum deviation observed is always less than 8%.

The Ni_3Al single crystal used in this work was a disk with a diameter of 8 mm exposing the (111) face of the FCC lattice. The crystal was carefully cleaned by repeated cycles of sputtering and annealing up to 1170 K. After each cleaning procedure, the surface quality was checked by means of XPS and LEED.

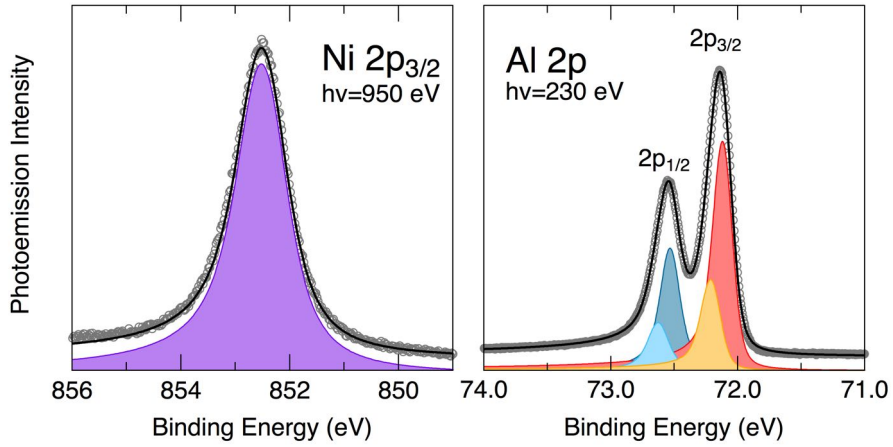

Figure 4.3: (left) Ni $2p_{3/2}$ and (right) Al 2p XPS spectra for the clean $Ni_3Al(111)$ surface. The fit components are shown superimposed.

Fig. 4.3 shows the XPS characterization of the clean sample. The Ni $2p_{3/2}$ spectrum (left) shows the presence of a single broad component at 852.50 $\pm$ 0.05 eV BE, with a FWHM of about 1.2 eV.

On the other hand, the Al 2p core level (fig. 4.3 right) shows a more structured shape. Beside the two spin orbit components, another doublet must be included in the fitting procedure. The presence of another doublet can be interpreted in terms of the signal arising from the surface atoms, opposed to that coming from the bulk ones, in analogy to similar system like the NiAl(110) and the Al(111) [22, 23]. The two spin orbit replicas are shifted by 95 $\pm$ 10 meV, as obtained by fitting a 4 components D-S function to the experimental data. To correctly assign the components,we performed a set of DFT calculations, finding a SCLS of -87 meV, in good agreement with the experimental value. Following this finding we were able to identify all the 4 components as follow:

Fitting parameters	**2p$_{1/2}$ doublet**	**2p$_{3/2}$ doublet**
	bulk (light blue)	bulk (yellow)
Lorentzian width	125 $\pm$ 70 meV	52 $\pm$ 8 meV
Asymmetry	≈ 0	0.11 $\pm$ 0.07
Gaussian width	115 $\pm$ 35 meV	145 $\pm$ 15 meV
Binding Energy	72.62 $\pm$ 0.02 eV	-0.42 $\pm$ 0.04 eV (spin-orbit)
	surface (deep blue)	surface (red)
Lorentzian width	123 $\pm$ 25 meV	52 $\pm$ 5 meV
Asimmetry	≈ 0	0.11 $\pm$ 0.06
Gaussian width	107 $\pm$ 17 meV	144 $\pm$ 5 meV
SCLS	-95 $\pm$ 12 meV	-95 $\pm$ 12 meV

Table 4.1: Al 2p core level lineshape parameters obtained for the clean $Ni_3Al(111)$.

Oxygen contaminations, due to the background pressure of the vacuum chamber, can be excluded by looking at the Al 2p core level. In fact, due to high reactivity of the surface towards the oxidation process, a tiny amount of adsorbed oxygen would result in the formation of some aluminum oxide on the surface, dramatically affecting the Al 2p spectral lineshape. Moreover, other contaminations, like C, Si, S and other metals were excluded by checking their core levels. Thanks to the high photon flux and to the excellent resolving power of the SuperESCA beamline, we were able to exclude any contamination with a 0.01 ML accuracy.

The surface quality was also checked by means of LEED measurements. Fig. 4.4 shows a diffraction pattern acquired after the cleaning procedure. The presence of the the hexagonal (2x2) pattern alone (previously reported for this surface [20]) clearly excludes any superstructure, which could be related to contaminants or defects. Finally, the sharp and round diffraction spots indicate the presence of large surface terraces, with an average dimension well beyond the experimental transfer width (100 Å).

4.1.2 Graphene growth and characterization of the $Ni_3Al(111)$ surface

A single graphene layer was grown on the surface by means of high temperature ethylene CVD. The sample was kept at 950 K while exposing it to a maximum partial pressure of ethylene of $2{\cdot}10^{-6}$ mbar, up to a total exposure of about 10^3 Langmuir. These parameters were chosen, after a set of trial exper-

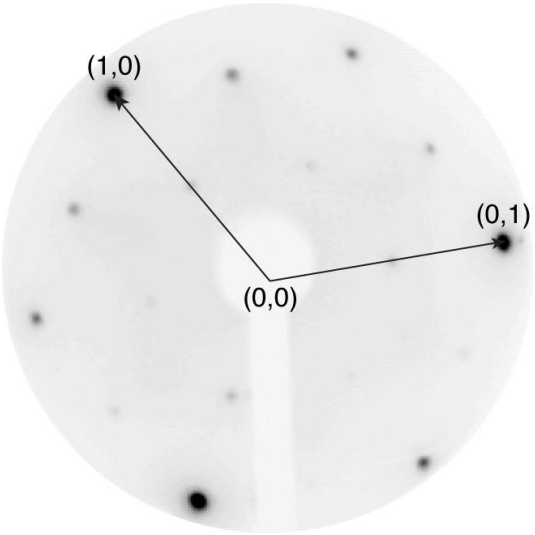

Figure 4.4: LEED image of the clean $Ni_3Al(111)$ surface acquired at 71 eV.

iments, to reduce the probability of carbon dissolution into the bulk and, at the same time, to obtain a high-quality graphene layer. In particular, a high pressure was needed to ensure a fast formation of nucleation seeds, while a high temperature was selected to enhance the carbon surface mobility, and hence to promote their surface diffusion and the subsequent formation of an ordered graphene layer. Higher temperatures were not allowed due to the thermally enhanced carbon bulk solubility.

The fingerprint of Gr formation is given by the C 1s core level spectrum. Fig. 4.5 shows a set of C 1s core level photoemission spectra acquired during Gr growth at 950 K after different ethylene exposure. At low exposure, we observe a peak at $\approx$ 283.5 eV, most probably due to C_2H_4 fragments and surface carbides, as suggested by previous findings for Gr grown on a Ni(111) [24, 25, 26, 27]. As the coverage increases, a new component is observed at $\approx$ 284.8 eV, attributed to Gr by comparison with Gr on Ni(111) [24, 25]. The integrated intensity of the C 1s spectrum (fig. 4.5 top) shows a saturating behaviour, indicating a self-limiting process. Moreover, the spectral weight of the initial low BE component gradually decreases from 8% to 1% of the final total area, indicating an almost complete conversion to Gr. When measured at room temperature, and with a higher resolution (see fig. 4.6), the C 1s core level XPS spectrum shows, beside the residual low BE phase, two narrow components related to Gr: the main component (C0) centered at 284.84 eV BE, and a weaker shoulder (C1) shifted by -410 meV. These values are quite close to what is reported for Gr on Ni(111), where a single peak is observed at 284.7

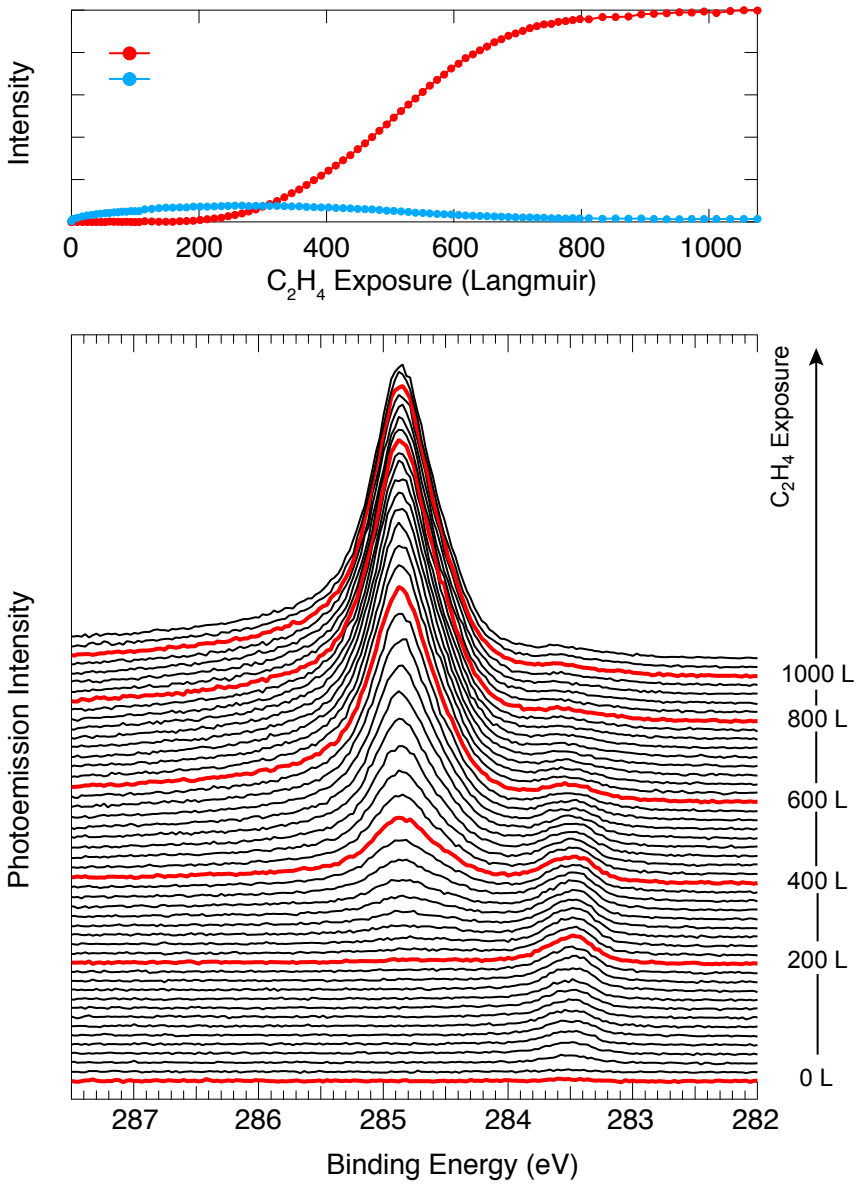

Figure 4.5: (bottom) C 1s core level photoemission spectra acquired at different exposures during ethylene exposure at 950 K, and (top) integrated area of the Gr (red) and C_2H_4 fragments/carbide (light blue) components of the C 1s spectrum. Intensities have been normalized to the final value.

eV BE. Moreover, the high value of the C 1s BE, compared to those reported for Gr grown on other transition metals [2, 28], suggests that Gr strongly interacts with the $Ni_3Al(111)$ surface, similarly to other strongly interacting systems, such as, for example, Gr/Ni(111), Gr/Ru(0001), and Gr/Rh(111).

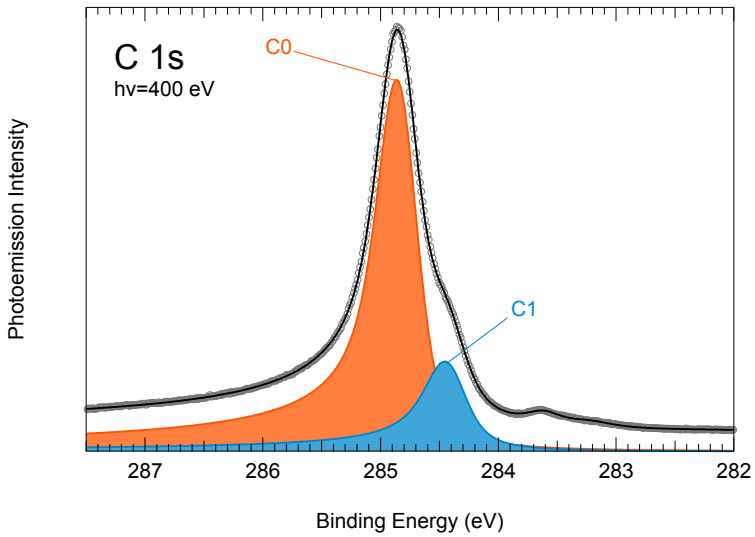

Figure 4.6: C 1s core level photoemission spectrum acquired after Gr growth on $Ni_3Al(111)$. The C0 (orange) and C1 (light blue) fitting components are shown superimposed to the experimental data (grey circles), together with the best fit result (black line).

Fitting parameters	**C0**	**C1**
Lorentzian width	188 $\pm$ 7 meV	261 $\pm$ 7 meV
Asymmetry	0.16 $\pm$ 0.01	0.16 $\pm$ 0.03
Gaussian width	271 $\pm$ 5 meV	230 $\pm$ 7 meV
Binding Energy	284.84 $\pm$ 0.02 eV	-410 $\pm$ 20 meV

Table 4.2: C 1s core level lineshape parameters obtained for after Gr growth on $Ni_3Al(111)$.

The corresponding fast XPS measurements of the Al 2p core level (fig. 4.7 (a)) are consistent with the formation of a Gr layer, which causes a $\approx$65% reduction of the overall Al 2p photoemission signal. In the high resolution Al 2p spectrum measured at room temperature after Gr growth (fig. 4.7 (b)), we observe two spin-orbit doublets. The first doublet (dark/light grey) is assigned to bulk atoms, by comparison to what was found for the clean surface (fig.

4.3), while the additional doublet (dark/light yellow), shifted by +160 meV with respect to the bulk one, is assigned to the interacting Al atoms at the metal-Gr interface. Note that the surface doublet observed for the clean surface is no longer present, confirming that the Gr layer covers the whole metallic surface.

The Ni $2p_{3/2}$ core level photoemission spectrum (fig. 4.7 (c)) does not show any appreciable lineshape modification after Gr growth, but an intensity reduction due to the screening from the topmost Gr layer, meaning that the Ni atoms are not strongly perturbed.

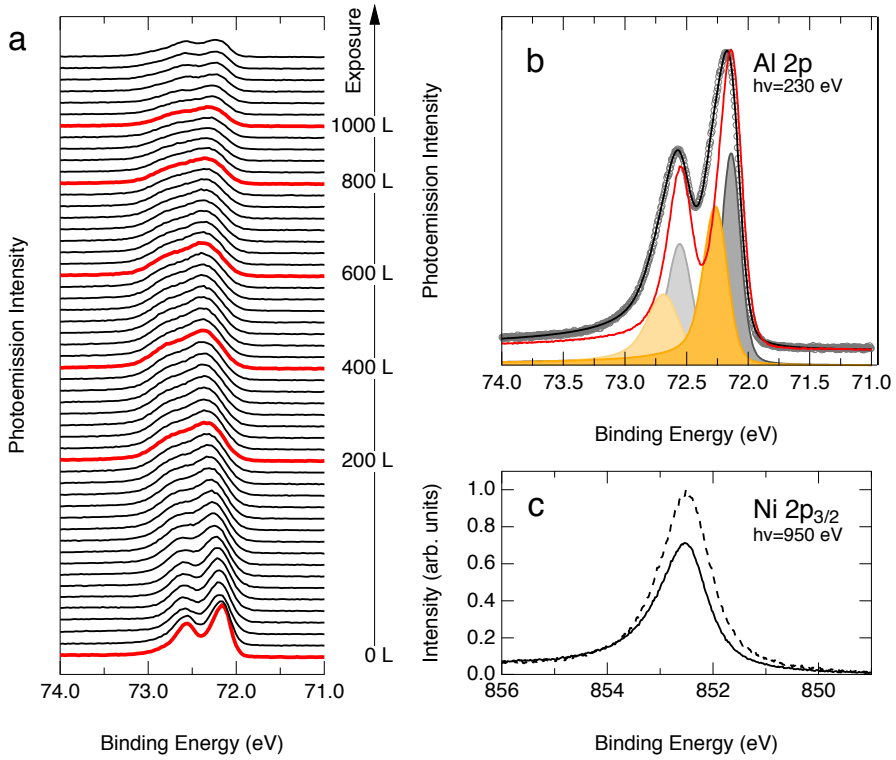

Figure 4.7: (a) Al 2p core level fast XPS spectra acquired during ethylene exposure up to Gr formation. (b) High resolution Al 2p photoemission spectrum measured at room temperature after Gr growth. The fit (black curve) is shown superimposed to the experimental data (grey circles), along with the bulk (dark/light grey) and interface (dark/light yellow) components for the spin-orbit levels. The Al 2p spectrum obtained for the clean surface (red line) is plotted, after proper normalization, as a reference. (c) Ni $2p_{3/2}$ core level photoemission spectra. The spectrum acquired after Gr growth (solid line) is plotted together with the one acquired for the clean surface (dashed line).

The LEED pattern of the Gr/Ni_3Al(111) system, reported in fig. 4.8, shows the same hexagonal periodicity observed for the clean substrate (see fig. 4.4),

indicating that, due to little lattice parameter mismatch of only 2.4 %, Gr grows commensurate to the surface and that the first substrate layers do not undergo any reconstruction. The enhanced intensity of the second order diffraction spots, as well as the decreased intensity of the first order ones, with respect to the clean case are explained in terms of constructive interference of the Gr and substrate diffraction patterns, and of a Gr induced screening effect respectively. On the other hand, the weak ring-shaped modulation observed in the diffraction pattern, reveals the presence of a small amount of rotational domains, as reported also for Gr on Ni(111) [29, 30]. These rotational domains are mainly aligned $\pm 16^{\circ}$ with respect to the main substrate orientation, as obtained by the analysis of the intensity modulation of the ring-shaped feature.

Figure 4.8: LEED diffraction pattern for the Gr/Ni_3Al(111) system acquired at 71 eV.

To get a more detailed insight into the structure and properties of our system, we performed extensive DFT calculations. Fig. 4.9 shows the six possible high symmetry adsorption geometries that can be obtained by imposing that Gr forms a commensurate (2x2) structure with the substrate, as judged by LEED. All these configurations were tested and are named after the adsorption sites of the two non equivalent C atoms inside Gr unit cell. We found that the minimum energy configuration is the B-TOP, followed by the TOP-FCC, which is only 60 meV higher in energy, like in the case of Gr on Ni(111) [29]. The B-FCC and B-HCP configurations are not stable and eventually relax into the TOP-FCC and TOP-HCP configurations respectively. Finally, the TOP-HCP and FCC-HCP are the least stable, separated by 0.16 and 1.12 eV respectively, with respect to the minimum energy configuration.

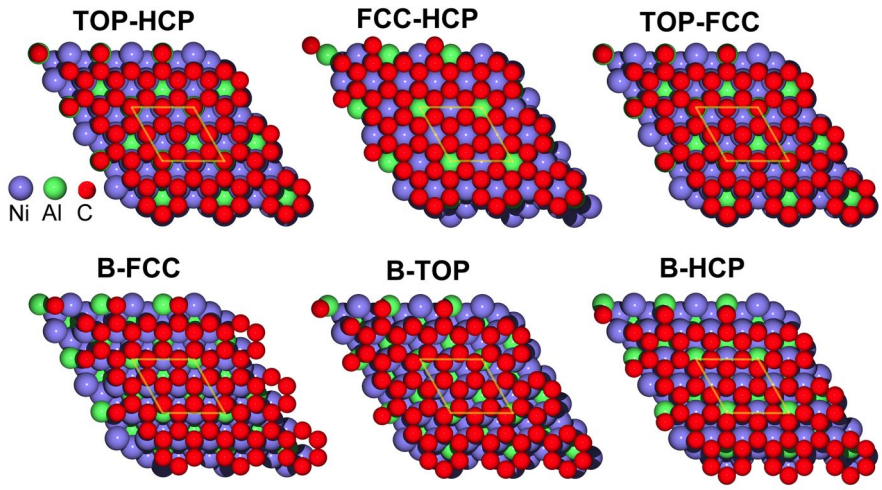

Figure 4.9: Different simulated adsorption geometries for the Gr/Ni_3Al(111) system. Each configurations is labelled after the adsorption sites of the non equivalent C atoms inside Gr unit cell.

To understand which of the two minimum energy configurations is the experimentally observed one, we simulated the C 1s photoemission spectrum for the two cases. To this purpose, we first calculated the C 1s BE for all the non equivalent C atoms inside the (2x2) unit cell. Subsequently we fitted a multi-peak D-S function to the data. Each non equivalent C atom was associated to a different component in the D-S function. The lineshape was constrained to be the same for all the components, which is equivalent to assuming the same final state lifetime, the same phonon broadening, and the same electron-hole pair excitation probability. On the other hand the intensity of each component was set proportional to the number of equivalent C atoms, while the BE shifts were constrained to be the DFT calculated one. The fitting results are shown in fig. 4.10 . By comparing the simulated photoemission spectra for the two cases, we found a slightly better agreement for the TOP-FCC structure. However, the coexistence of the two phases cannot be excluded. For the TOP-FCC structure, the calculated mean distance between the Gr layer and the substrate is 2.12 Å, similar to Gr/Ni(111) [31].

The electronic structure of the system was investigated by means of valence band photoemission measurements. Specifically, ARPES measurements (fig. 4.11) show that the whole π-band of Gr is shifted to higher BE with respect to free-standing case. This is similar to what has been reported for Gr on Ni(111) [32] and results from the strong hybridization between the Gr and metal 3d

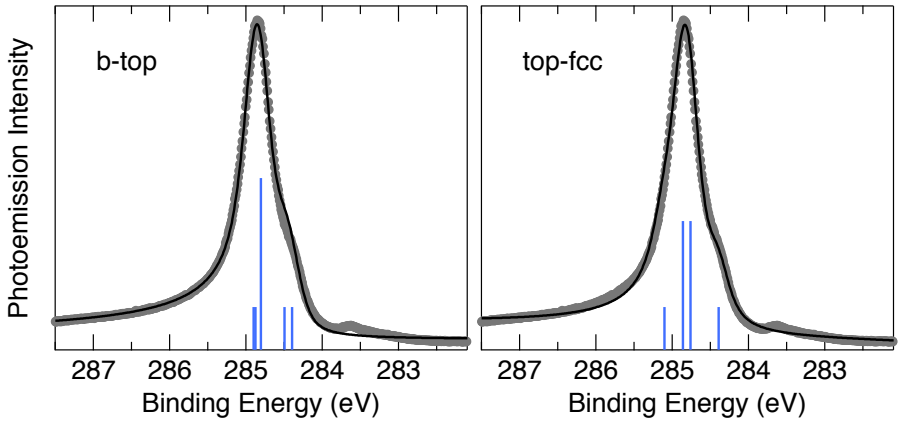

Figure 4.10: Simulated C 1s spectra (black line) for the B-TOP (left) and TOP-FCC (right) configurations, after DFT calculations of the C 1s BE (blue bars) and fitting. The experimental data are shown superimposed (grey circles).

valence band states. In particular the bottom of the band, at the M point, is found 4.7 $\pm$ 0.1 eV below the Fermi level, while the Dirac point (K) is found at 2.7 $\pm$ 0.5 eV BE. The high density of states at the Fermi level, on the other hand, is dominated by the Ni d-band of the alloy substrate. The calculated band structure for the TOP-FCC Gr/Ni_3Al(111) geometry shows an excellent agreement with the experimental data, supporting the hypothesis that the observed structure is predominantly TOP-FCC.

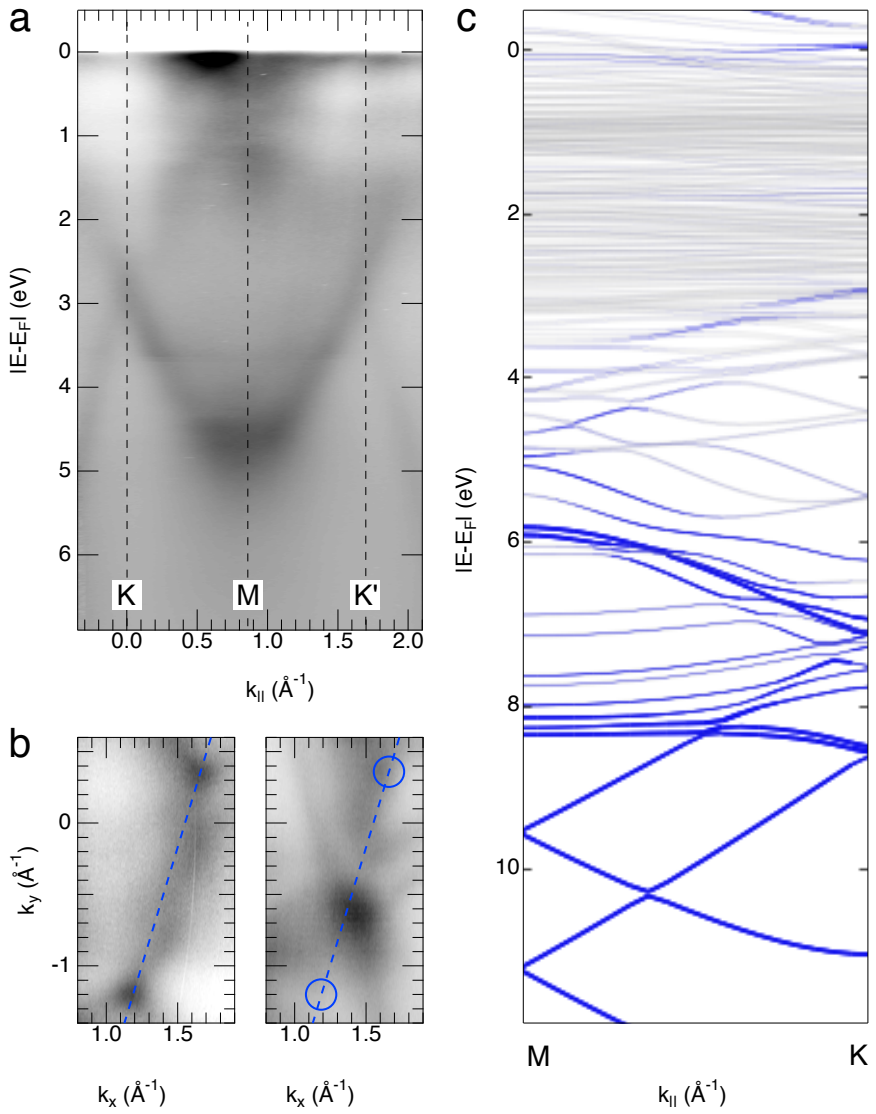

Figure 4.11: (a) ARPES measurement of the Gr/Ni_3Al(111) energy band dispersion along the K-M-K' direction in the reciprocal space and (b) constant energy surfaces at the Dirac point energy (left) and at the Fermi level (right). (c) DFT-calculated Gr energy band dispersion along the M-K direction for the TOP-FCC structure. The bands with a participation of 50% or more of carbon orbitals are highlight using blue lines.

4.1.3 Graphene alumina nanosheet interface: oxidation of the $Ni_3Al(111)$ surface

After Gr growth the sample was exposed to a high partial pressure of oxygen ($3{\cdot}10^{-3}$ torr) at 520 K. Following this procedure, it is possible to intercalate oxygen underneath Gr and to selectively oxidize only the Al atoms at the metal interface. In fact, the intercalation of light atoms has already proven to be an effective method for creating an interfacial layer between Gr and the substrate [33, 34, 35, 36]. On the other hand, selective oxidation of Ni-Al alloys, to form ordered alumina layers, has been previously reported [37, 38].

Fig. 4.12 shows a series of high resolution core level XPS spectra acquired at different oxygen exposures during the oxidation process. Looking at the evolution of the C 1s core level spectrum, we observe the appearance of a new component, at lower BE with respect to the previously described Gr peak. This new component is assigned, by comparison with literature [2, 28, 39], to regions of weakly interacting Gr supported by an oxide substrate. As the oxygen exposure increases, the spectral weight shifts continuously to this new peak, indicating that the oxide layer growth proceeds by subsequent nucleation and expansion of oxide islands. Eventually, after a total O_2 exposure of more that 10^7 L, the original Gr peak completely vanishes, confirming the formation of a decoupled Gr layer sitting on a fully oxidized surface. The final C 1s core level photoemission spectrum consists of a single, narrow, peak at 284.18 $\pm$ 0.02 eV BE, corresponding to 590 meV lower BE shift with respect to the higher BE component (C0) of the original C 1s spectrum. It is important to stress that, during the oxidation process, the total integrated intensity of the C 1s spectrum decreases by less than 5%, indicating that the oxide layer grows below Gr[2] and that the integrity of the Gr layer itself is preserved during the process. On the other hand, the presence of a single and narrow component ensures that the quality of the C network has been preserved as well. In fact, the formation of a high density of defects, such as single/double vacancies, and Stone-Wales defects, would result in additional low BE components, as obtained by previous DFT calculations and photoemission data [40, 41]. Our high resolution C 1s spectrum clearly exclude a defects concentration >1%, as observed in fig. 4.13, where the experimental C 1s core level spectrum acquired after substrate oxidation is reported together with the simulated spectra for different concentrations of single/double vacancies and Stone-Wales defects. Finally, it is important to underline the absence of any interfacial buffer layer between Gr and

[2] In fact, if the oxide layer had grown on top on Gr, we would have observed a strong screening effect on the C photoemission signal.

alumina, which would give rise to a feature at 281.5 eV (the BE corresponding to the Al-C bonds) and 282.5 eV (Al-O-C bond) [42, 43], and also to C-O bonds, which are typically found in the C 1s spectrum at binding energies >284.2 eV [34].

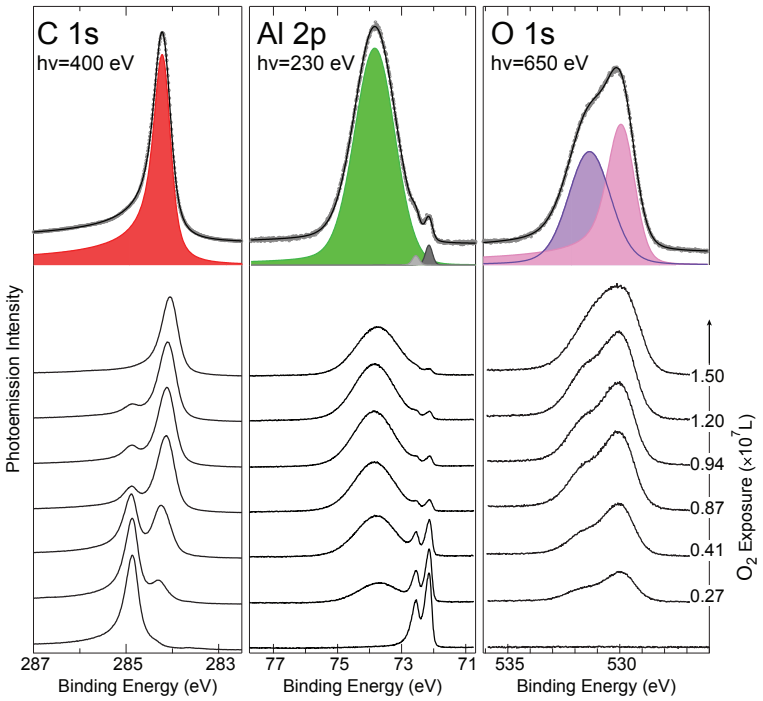

Figure 4.12: High resolution XPS core level spectral series acquired, at different oxygen exposure, during the surface oxidation below Gr. From left to right: C 1s, Al 2p, and O 1s. The spectra were recorded at room room temperature after each oxidation step. (top) The final spectrum is reported together with the deconvolution of the fitting components.

The formation of an alumina layer is confirmed by looking at the Al 2p core level photoemission spectrum (fig. 4.12). Similarly to C 1s case, we monitored the Al 2p spectrum during oxidation, as a function of the total oxygen exposure. As the oxygen intercalation proceeds, we observe the appearance of a new broad peak, centered at about 73.8 eV BE, in the region typically associate to aluminum oxide [38, 37]. However, rather than multiple, well defined, components, the Al 2p spectrum shows one single broad peak, with a FWHM >1.5 eV, suggesting that the alumina film is not homogeneous and well ordered.

On the other hand, by looking at the Ni $2p_{3/2}$ spectral series (not reported here), we observe that Ni atoms are only marginally affected by the oxidation process. The major effect observable in the series is, by far, a strong screening by the topmost alumina layer, which causes an intensity drop >90%. A new

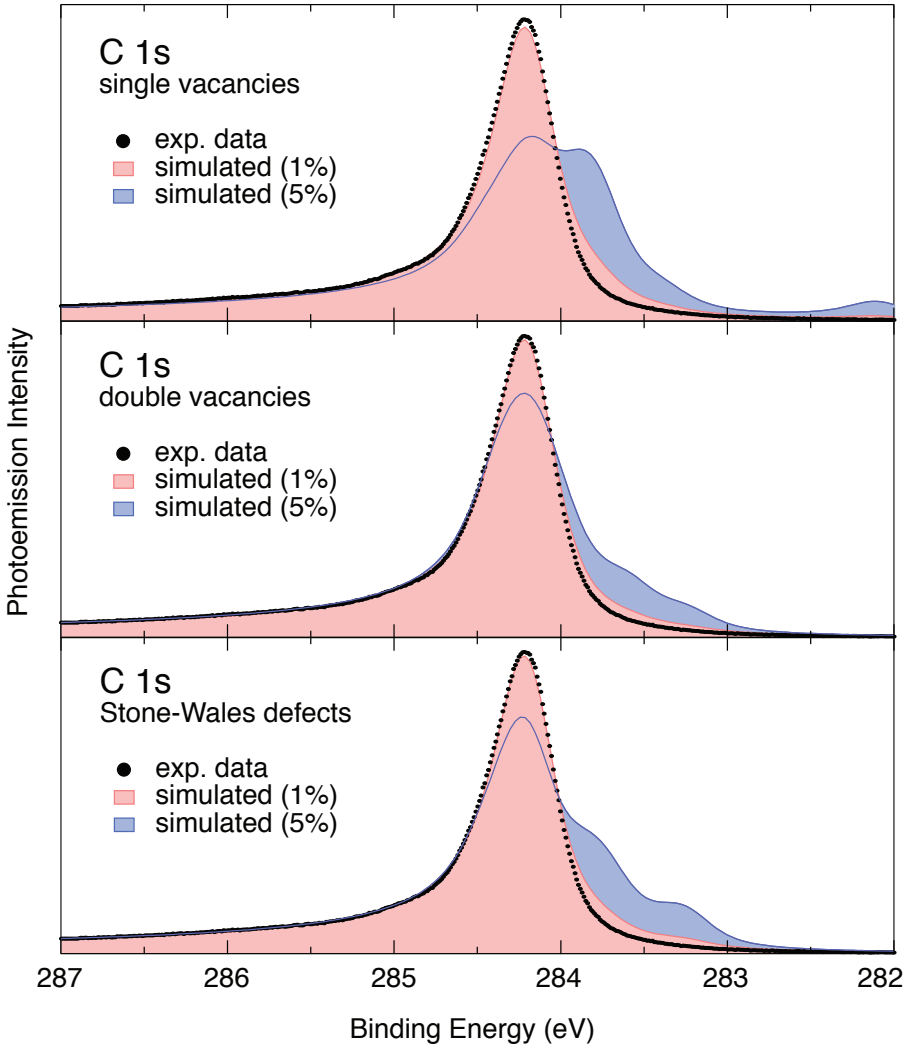

Figure 4.13: High resolution C 1s core level spectrum after substrate oxidation. The experimental spectrum (black dots) is plotted together with the simulated spectra for 1% (red) and 5% (blue) concentration of single vacancies (top), double vacancies (middle), and Stone-Wales defects (bottom). The simulated spectra were obtained by imposing a fixed amount of defective C atoms whose BE was fixed to the one calculated in literature [40].

component is also observed, at higher BE, which is interpreted in terms of partly oxidized interfacial Ni atoms. This finding can be explained in terms of a thermally promoted surface segregation of the Al atoms, resulting in a Ni-depleted first layer. Since the oxide film is mainly composed by alumina, we were able to estimate the oxide layer thickness from the intensity drop of the Ni $2p_{3/2}$ signal. The calculation was done taking into account the inelastic mean free path for the alumina layer, at a given photoelectron kinetic energy, which was set equal to the bulk value of 7.07 Å, as obtained by the Tanuma, Powell, and Penn formula [44]. The estimated mean thickness of the alumina layer is 1.5 ± 0.2 nm.

Finally, the O 1s spectrum after oxidation shows two components at about 529.8 and 531.3 eV BE, which were interpreted, by comparison to literature [37], in terms of oxygen atoms belonging to different layers of the oxide film.

ARPES measurements, reported in fig. 4.14, further confirm that Gr sitting on alumina is strongly decoupled from the metallic substrate. The bottom of the band at the M point is now found at 2.6 ± 0.1 eV, corresponding to a ≈ 2 eV shift of the whole π band with respect to Gr/Ni_3Al(111). A similar bahaviour is reported for Gr electrically decoupled from the Ni(111) substrate by means of Au intercalation [32]. On the other hand, close to the Fermi level, the linearity of the band dispersion is fully restored. From a linear fit of the dispersion curve close to the K point (fig. 4.14 (c)) we estimated that the group velocity of the charge carriers ($\delta E(k)/\delta k$) is $\approx 8 \cdot 10^5$ m s $^{-1}$ (≈1/370 of the speed of light), in good agreement with the theoretically predicted value for free-standing Gr [45]. From fig. 4.14 we can also observe that the K and K' Dirac points are found above the Fermi level, as judged from the fact that Gr π band crosses the Fermi level, indicating an oxygen induced p-doping. This is further confirmed by a k_y vs k_x map at the Fermi level, shown in fig. 4.14 (d), where a non-zero density of states in observed at the K point. From a linear extrapolation we estimate that the Dirac point is 200 ± 40 meV above E_F. The DFT calculated band dispersion for a Gr layer on α-phase Al_2O_3(0001), reported in fig. 4.14 (b), which approximately reproduces the experimentally obtained thick alumina layer, shows excellent agreement with the experimental data. In particular, the bottom of the π-band and the region near the Dirac point are well-reproduced. The calculated band energy value at the K point lies 220 meV above E_F, consistent with the experimentally extrapolated value.

To investigate the structural quality of the Gr layer after the oxidation process, we performed LEED, μ-LEED, and LEEM measurements. Fig. 4.15 shows three diffraction pattern acquired at 71 eV for the clean sample,

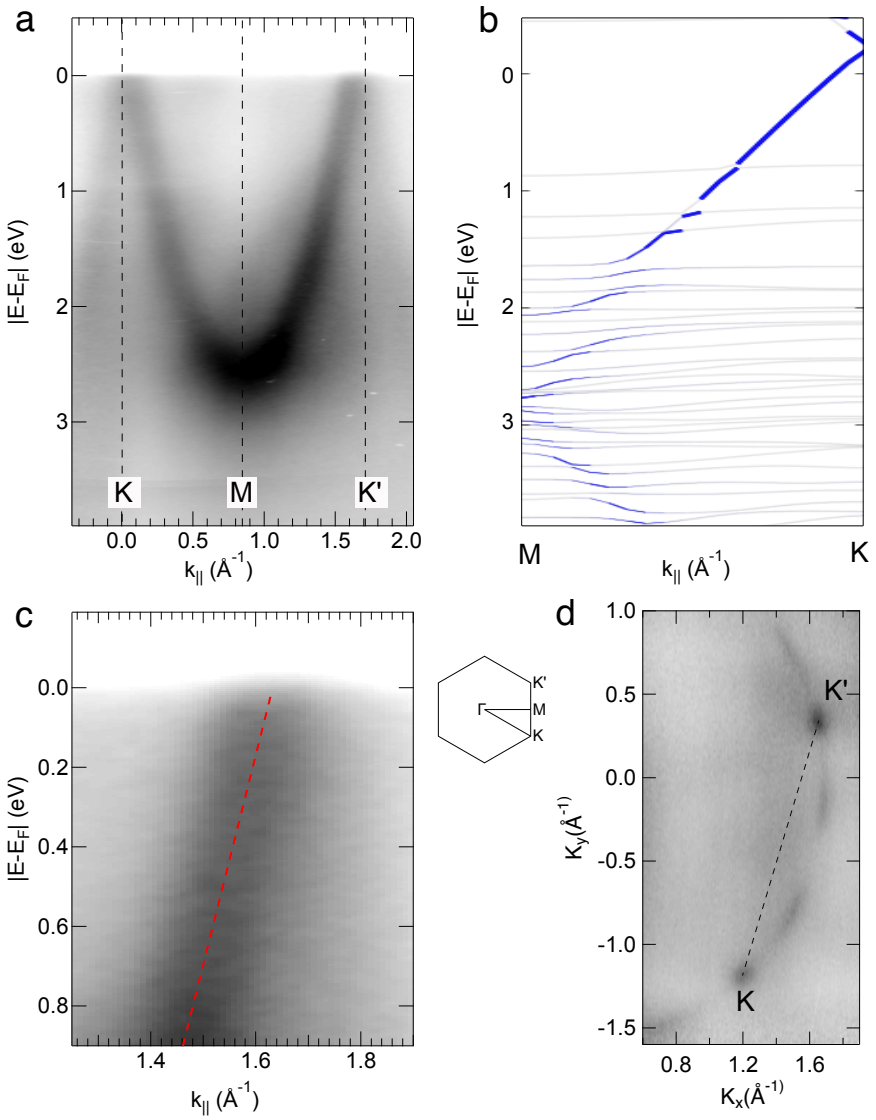

Figure 4.14: (a) Experimental electronic band structure along the K-M-K' direction of the reciprocal space for the $Gr/Al_2O_3/Ni_3Al$ system. (b) DFT simulated electronic band structure along the M-K reciprocal space direction for the Gr/Al_2O_3 system. The bands with a participation of 50% or more of carbon orbitals are highlight using blue lines. (c) Zoom of the experimental energetic band dispersion near the Dirac point at the Fermi level. The result of a linear fit is shown superimposed (red, dashed line). (d) Experimental constant energy surface at the Fermi level. The K-M-K' direction is shown superimposed (dashed line).

Gr/Ni_3Al(111), and Gr/Al_2O_3/Ni_3Al(111) cases. The transition from a threefold to a sixfold symmetry between the clean and Gr diffraction pattern, as judged by the circular line profiles reported in the bottom part of the figure, is consistent with the formation of a single Gr layer on top of the metallic substrate. Most importantly, comparing the Gr/Ni_3Al(111) diffraction pattern to the one observed for Gr/Al_2O_3/Ni_3Al(111), we observe that the spot shape and size is preserved and additional spots cannot be detected. This indicates that the long range order of Gr is unperturbed, and that the overall quality of the C layer is largely preserved. The diffraction pattern acquired after oxidation shows an increased background, clearly visible in the circular line profile, consistent with the hypothesis of a disordered oxide film. Moreover, the diffraction spots of the metallic surface are no longer visible in the last pattern, due to the screening of the thick alumina layer. Finally, the small increase in the FWHM of the spots ($\sim$9%) is interpreted as due to corrugations of the alumina layer. In this respect, it is important to stress that the roughness of epitaxial Gr on SiO_2 is always found to be larger than that of free-standing Gr, due of the energetic cost of the elastic deformations, which prevent the Gr layer from exactly conforming to the substrate morphology [46, 47].

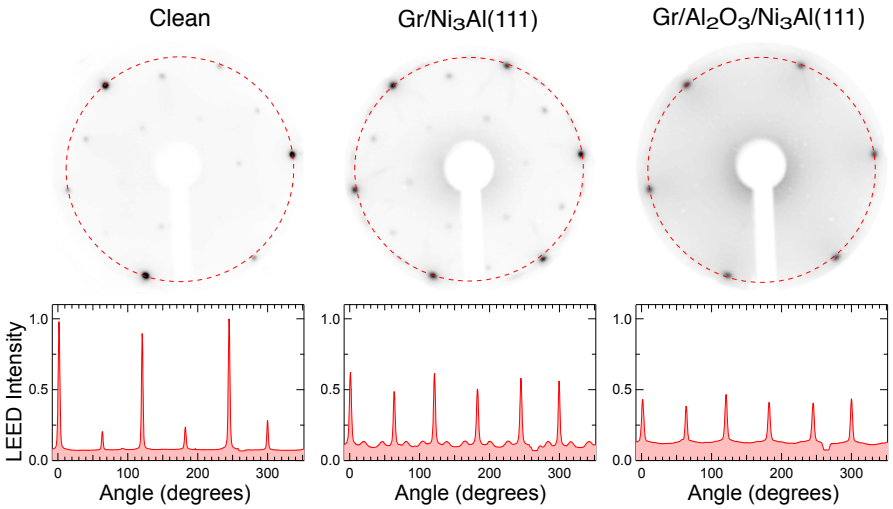

Figure 4.15: Low energy electron diffraction patterns of the (left) clean Ni_3Al(111), (middle) Gr/Ni_3Al(111), and (right) Gr/Al_2O_3/Ni_3Al(111) structures acquired at the same electron energy (71 eV). The bottom panel represents the corresponding circular diffraction profiles, as shown in the top images (red, dashed circles).

To achieve a more detailed insight into the morphological structure quality of the sample at the nanometer scale, we employed LEEM and μ-LEED. Our

measurements showed that Gr extends continuously across the oxide film, thus confirming that the C atoms are not etched by oxygen during the oxidation process. Fig. 4.16 shows two dark field images of the same region of the $Gr/Al_2O_3/Ni_3Al(111)$ system. These images were acquired using one of the first order diffraction spot of the epitaxial and rotated structures, to map their lateral extension. Micrometer size Gr flakes were observed for both phases. A few nanometer-size dark features are observed within some of them, suggesting that the structure of the oxidized substrate may be locally inhomogeneous.

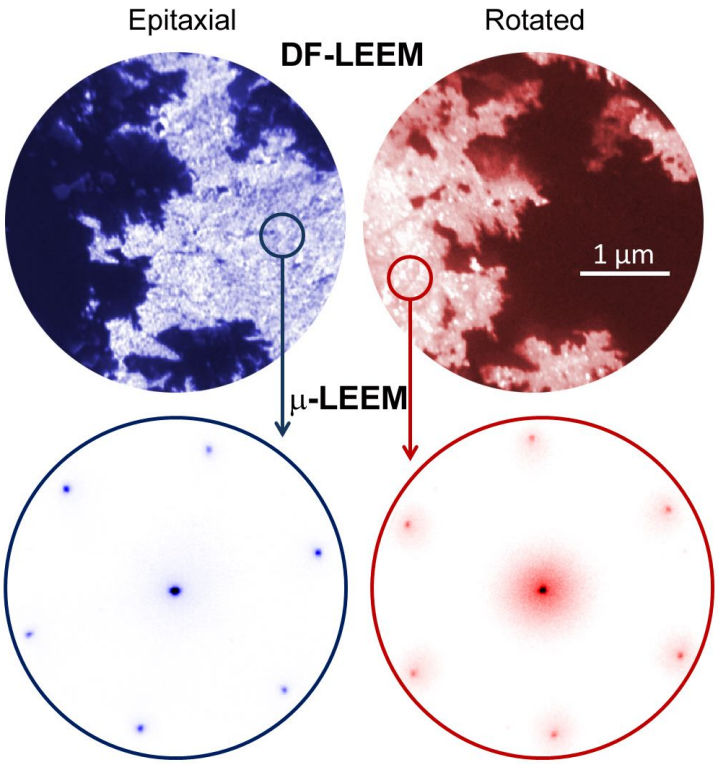

Figure 4.16: (top) Dark field LEEM images of (left) an epitaxial and (right) a rotated Gr flake. The two images, which were obtained using the corresponding first order diffraction beams, map the lateral extent of two differently oriented Gr domains within the same microscopic region of the sample. (bottom) μ-LEED pattern from the same two domains, as measured by probing an area of diameter 500 nm. Electron energy is 50 eV.

The μ-LEED diffraction patterns for the epitaxial and rotated flakes show similar characteristics, suggesting a similar crystal quality. In particular, the epitaxial Gr pattern displays a purely Gaussian line shape profile, with HWHM <0.06 $Å^{-1}$. This value is much smaller than those reported for both SiO_2-

supported and suspended exfoliated single-layer Gr [48], the former being the reference material used in graphene prototypical devices and indicative of excellent crystal quality. On the other hand, the diffraction pattern of rotated Gr flakes shows a predominantly Gaussian line shape with a HWHM<0.08 $Å^{-1}$, indicating a slightly lower crystal quality, probably due to the lower rotational coherence.

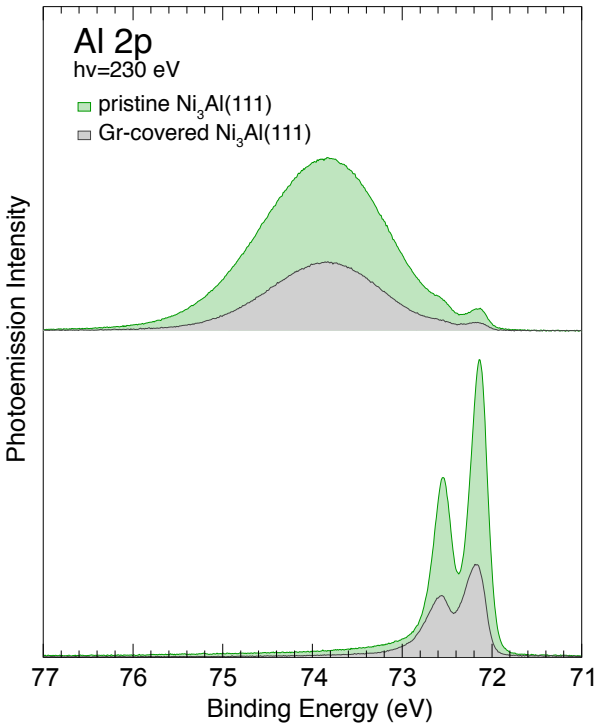

Figure 4.17: Al 2p photoemission spectra acquired in the same condition for the clean (green) and Gr-covered (grey) sample: (bottom) clean substrate and (top) after formation of an alumina nanosheet.

To understand the effect of the Gr layer on the oxidation process, we finally performed oxidation experiments on the clean $Ni_3Al(111)$ surface, to be compared to $Gr/Ni_3Al(111)$. Fig. 4.17 shows a series of photoemission spectra acquired for the clean and Gr-covered sample in similar oxygen coverage conditions. Fig. 4.17 (a) shows the Al 2p XPS spectra before and after Gr growth, while fig. 4.17 (b) shows the same core level photoemission spectra for the oxidized bare $Ni_3Al(111)$ and for $Gr/Al_2O_3/Ni_3Al(111)$. The clean surface was oxidized at 520 K in $4{\cdot}10^{-7}$ torr oxygen atmosphere, approximately to the same coverage reached in the oxygen intercalation experiment (fig. 4.12). After oxidation, the Al 2p spectrum is comparable to the one obtained in the presence

of Gr, apart from an intensity enhancement due to the absence of the Gr layer. In particular, both spectra shows a broad peak centered at 73.8 eV BE, while a residual signal arising from the metallic Al bulk atoms is still visible. This finding suggests that the oxide layer composition is the same in both cases, and that Gr plays a minor role in the substrate oxidation process. The only difference is that, of course, a higher oxygen exposure is needed to oxidize the surface in the presence of Gr, since the intercalation probability must be taken into account. Notably, the effect of Gr on the Al 2p signal reduction amounts to 65% in both cases.

In conclusion, a novel, effective method, for the direct synthesis of high-quality Gr-alumina nanosheet interfaces was discussed. Starting from a Ni_3Al surface, we firstly grew a single Gr layer by means of high temperature CVD, and subsequently selectively oxidized the interfacial Al atoms by means of oxygen intercalation. This process resulted in a high-quality Gr layer supported by a $\sim$1.5 nm alumina film, as proved by a combination of photoemission, diffraction, and microscopy experimental techniques. DFT calculations strongly supported our findings.

We believe that our method could be used also other Al-based bimetallic alloys ($CuAl_2$, CoAl, FeAl, Fe_3Al) capable of breaking the C-H bonds in hydrocarbon molecules and of selectively oxidizing the Al atoms. On the other hand, the availability of a large range of bimetallic compounds, like Ni_3Ti and Pt_3Zr, can open new avenues for Gr-integrated materials with higher dielectric constant (ZrO_2 ϵ_r=25, TiO_2 ϵ_r=30 (anatase)-100 (rutile)) than conventional SiO_2 (ϵ_r=3.9). Finally, other oxide layers could be deposited on top of the Gr-oxide interface [16], in such a way to build oxide-Gr-oxide sandwiched heterostructures, which represents a fundamental architecture in most new generation electronic devices.

4.2 Chemical gating of epitaxial graphene

In the context of Gr integration into new generation nano-devices, ultrathin oxide layers on metal substrates represent a flexible class of supports due to the possibility, unavailable for bulk oxides, to adjust their thickness and therefore tune their electronic properties. Moreover, an additional and remarkable way for engineering ultrathin oxides is given by the possibility of introducing dopant atoms at the metal-oxide interface, in such a way to adjust the electron flow through the dielectric [49, 50, 51, 52]. In this case the controllable doping obtained by the spontaneous charge transfer through the thin dielectric barrier could enable new Gr-based architectures and activate unexplored graphene functionalization mechanisms. In this section we describe a method for producing high quality ultrathin SiO_2 layers with variable thickness at the Gr/Ir(111) interface by stepwise intercalation of silicon and oxygen. We demonstrate that, by controlling the amount of oxygen that diffuses to the Ir/SiO_2 interface, as well as the oxide layer thickness, it is possible to modulate the doping of the Gr layer lying on top of the oxide [53].

We start with a monolayer Gr grown on Ir(111) by thermal dissociation of ethylene molecules, as already described in the previous chapter. The bottom curves in fig. 4.18 (yellow lines) show the C 1s and Ir $4f_{7/2}$ core level spectra measured after Gr growth. The C 1s spectrum shows a single, narrow, peak at 284.09 eV, in good agreement with previous findings (see also chapter 3). On the other hand, the Ir $4f_{7/2}$ core level exhibits a two components lineshape, associated to the surface (S, 60.31 eV) and bulk (B, 60.85 eV) Ir atoms respectively [54, 55].

The first step to grow the Gr/SiO_2/Ir(111) structure is the intercalation of few MLs of Si below Gr [39, 56]. Silicon was evaporated in UHV conditions at a rate of about 0.02 ML per min using an electron beam evaporator placed at around 60 mm from the sample. To promote surface diffusion and intercalation of Si below Gr, the sample was kept at 670 K during the process. After the intercalation of 2.6 ML of Si the C 1s core level (fig. 4.18, green) shows a single, narrow, component (C_1) at 284.25 eV, corresponding to a +160 meV shift with respect to the Gr/Ir(111) system. The fact that the intensity of the C 1s spectrum is preserved upon intercalation of Si indicates that Si does not accumulate on top of Gr, but completely diffuses underneath forming a layer on the Ir surface. In fact, a Si layer partially sitting on top of Gr would induce a decrease in the C 1s photoemission intensity due to screening of the photoelectrons. If we assume a rigid shift of the C 1s core level due to charge transfer with substrate,

the observed BE shift indicates that Gr supported on Si is slightly n-doped with respect to the pristine case.

The Ir $4f_{7/2}$ core level recorded after Si intercalation shows an overall strong intensity decrease due to the screening of the additional Si buffer layer. This decrease is more pronounced for the S component, since the topmost layer Ir atoms are now found in a different local configuration. In fact, the increased spectral weight around 60.70 eV, indicating the presence of a new component, is most likely related to interfacial Ir atoms interacting with the Si layer. Accordingly the Si 2p spectrum shows a complex lineshape due to the formation of different Si-Si and Si-Ir bonds (fig. 4.18, green).

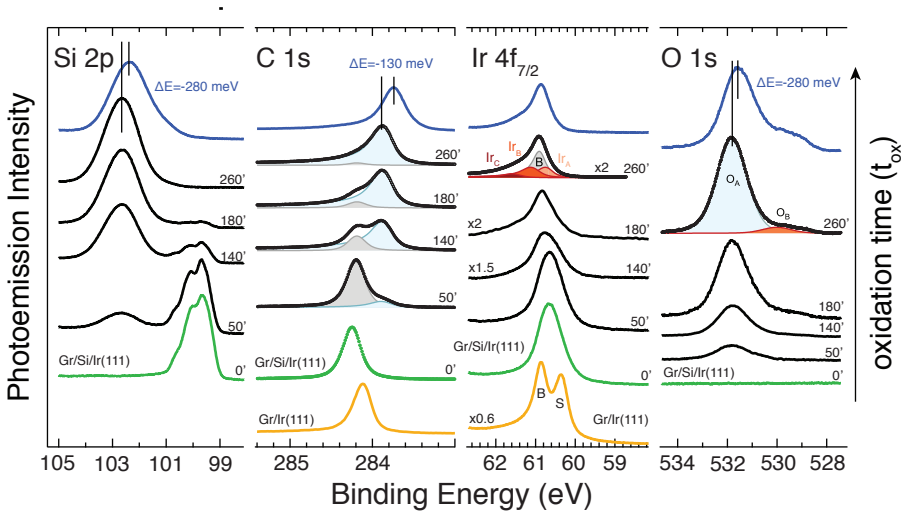

Figure 4.18: SiO_2 synthesis below graphene. Si 2p, C 1s, Ir $4f_{7/2}$ and O 1s core level spectra recorded on the Gr/Ir(111) surface (yellow), after the intercalation of 2.6 ML of Si (green) and during the oxidation by O intercalation (black). The top blue curves show the same core levels recorded after the oxidation of the Gr/Si/Ir(111) interface obtained after intercalation of 1.4 ML of Si; the numbers indicate the relative BE shifts measured with respect to the sample with the thicker oxide layer.

The oxidation of the Si layer was achieved by means of oxygen intercalation at 720 K. [39]. The corresponding core level spectra, acquired at increasing oxidation time (t_{ox}) up to complete oxidation, are reported in the upper part of fig. 4.18. During oxidation, the Si 2p spectrum lineshape gradually transform into a single broad component centered at 102.6 eV that indicates the formation of a SiO_2 layer [51].

Looking at the C 1s spectrum evolution we observe a gradual shift of the spectral weight from the C_1 component, which is associated to the Gr/Si system interface, to the lower BE C_2 component, which arises from regions of Gr sitting

on the oxide layer. Eventually, when the Si layer is fully oxidized, the C 1s spectrum presents only the C_2 component, shifted by -390 meV with respect to Gr/Si/Ir(111) and by -230 meV with respect to pristine Gr on Ir(111). Such a sizable doping is due to the effect of the electronegative O-Ir(111) surface which forms underneath, as oxygen partly diffuses to the SiO_2/Ir interface and chemisorbs on the metal substrate [39, 51, 52].

The presence of interfacial oxygen between the Ir surface and the oxide layer is reflected in the multiple components observed in the final Ir $4f_{7/2}$ spectrum (fig. 4.18, top). Besides the bulk peak (B), this core level spectrum exhibits the Ir_A (60.75 eV) and Ir_B (61.12 eV) components due to Ir atoms bonded to one and two oxygen atoms, respectively [34, 55], whereas the small Ir_C peak (61.60 eV) can be tentatively assigned to Ir atoms bonded to three O atoms. The relative intensities of the Ir_A and Ir_B components with respect to B are consistent with an O coverage of about 0.5 ML [34], this estimation being only marginally influenced by the Ir_C contribution.

Finally, the O 1s core level spectrum exhibits a two components lineshape, with the intense O_A components (531.8 eV) associated to the oxide phase, and the smaller O_B (530.0 eV) arising from the oxygen buffer atoms chemisorbed on the Ir surface [34]. Notably, the polarization arising from the presence of such O atoms on Ir surface is responsible for the BE shift of about -1 eV observed fro the Si 2p and O 1s core levels with respect to the values usually measured for SiO_2/Si interfaces [57].

By analyzing the Ir $4f_{7/2}$ core level intensity drop due to photoelectron screening, we computed the average thickness of the oxide layer to be about 1.6 nm, equivalent to 6.6 ± 0.7 MLs. However, the lack of any diffraction feature in the LEED pattern, besides the spots related to Gr, indicates that the oxide layer is predominantly amorphous.

For comparison the top blue curves in fig. 4.18 represent the core level spectra measured after the oxidation of the Gr/Si/Ir(111) interface obtained with a smaller amount of Si (1.4 ML). In this case, while the Ir $4f_{7/2}$ spectrum indicates a similar O coverage on the metal surface, the lower SiO_2 thickness (about 3.5 ML) determines a different energy level alignment at the Gr/SiO_2/O-Ir(111) interface. In fact both the Si 2p and O 1s spectra show an extra BE shift of about -280 meV because of the stronger electrostatic effect at the SiO_2 surface which now is closer to the O-Ir(111) interface. This is reflected in an extra BE shift of -130 meV for the C 1s peak, giving a total shift of -360 meV with respect to Gr/Ir(111).

Figure 4.19 (a) shows a summery of the C 1s spectra acquired for the in-

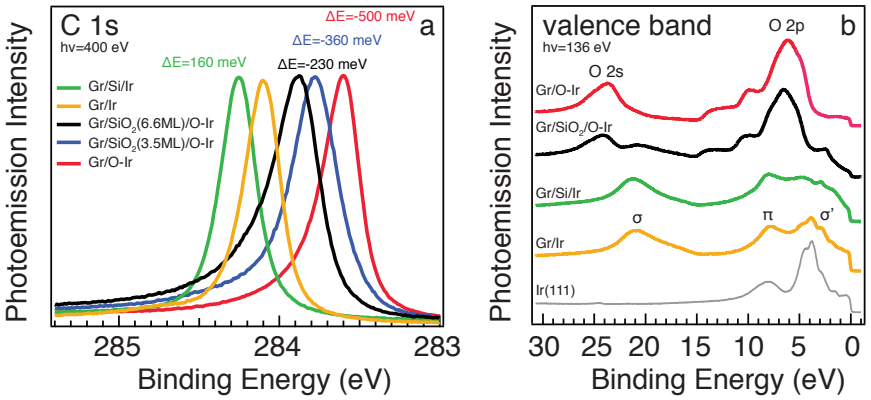

Figure 4.19: (a) C 1s core level spectra and (b) VB spectra recorded on the Gr/Ir(111) surface before and after the intercalation of Si, and after the synthesis of SiO_2 by stepwise intercalation of Si and O. In (a), the BE shifts with respect to the C 1s position measured for the Gr/Ir(111) surface (yellow curve) are shown at the top of the figure.

vestigated systems. For comparison, the spectrum recorded after intercalation of O below Gr grown on Ir(111) in the absence of the SiO_2 spacer is also reported, which has a similar amount of O chemisorbed on the Ir surface. With respect to Gr/Ir(111), Si intercalation induces an upward shift of 160 meV due to n-doping, whereas for the Gr/O-Ir(111) the C 1s peak shifts by -500 meV due to p-doping [34]. In the presence of the oxide layer the effect is lower and therefore the C 1s BE shift varies between -230 and -360 meV, depending on the thickness of the dielectric spacer.

Figure 4.19 (b) shows the VB spectra recorded during the experiment. When compared to the clean Ir(111) case (grey), the spectra obtained after Gr growth (yellow) and after Si intercalation (green) show the typical σ (20.9 eV), π (7.8 eV), and σ' (2.7 eV) bands associated to Gr. After oxidation the Gr valence band features are indiscernible because of the appearance of the typical SiO_2 spectral structures, which are the O 2s at about 24 eV, the O 2p lone pairs in the 4-8.5 eV region, and the features due to hybridization with the substrate between 10 and 13.5 eV [58].

The top curve in fig. 4.19 (b) shows the VB spectrum acquired for the SiO_2/O-Ir(111) system obtained by oxidizing a Si layer evaporated on the bare Ir(111) surface. Notably, the strong similarity between the spectral features measured for the SiO_2 layers synthesized with and without graphene excludes any influence on the oxide layer structure due to the presence of the graphene overlayer, in spite of the fact that on the bare Si/Ir(111) surface the oxidation rate is almost ten times faster.

The possibility to tunably doping graphene by modifying the buried metal-oxide interface was explored by removing the O chemisorbed on the Ir surface by thermal annealing. In fact, after the desorption from the Ir surface the oxygen diffuses through the porous ultrathin oxide [51, 59, 50] and escape from the sample relieving the graphene doping. The results obtained by annealing up to 1050 K the Gr/SiO_2/O-Ir(111) system corresponding to the 3.5 ML oxide layer are reported in fig. 4.20. High resolution XPS spectra (b-e) were acquired at room temperature after annealing the system to the selected temperature, while fast-XPS Si 2p core level presented in (a) were recorded as a function of the annealing temperature.

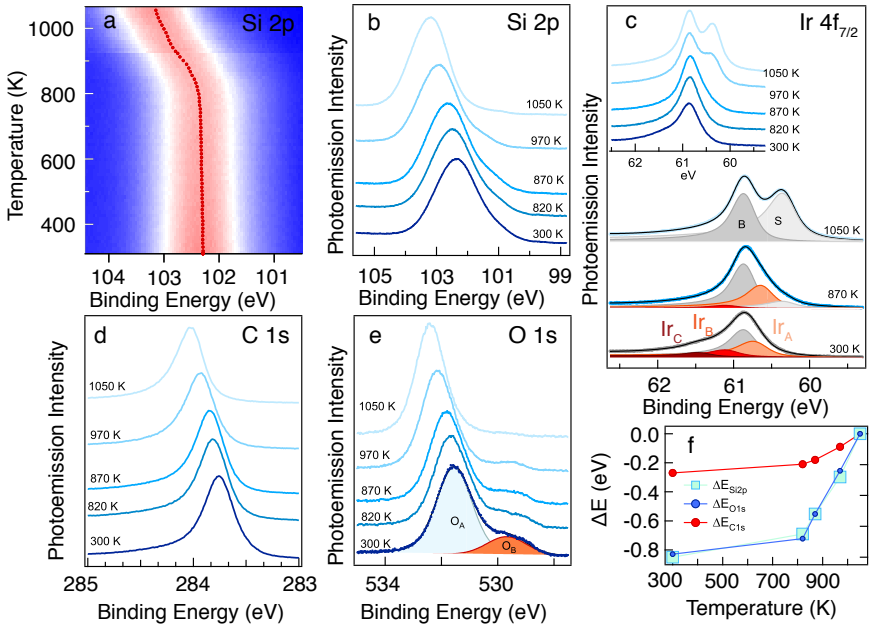

Figure 4.20: Thermal annealing of the Gr/SiO_2/O-Ir(111) structure with a 3.5 ML thick SiO_2 layer. (a) 2D plot of the Si 2p spectra recorded during sample heating at a rate of 1 K/s. The red dots indicate the position of the spectral maxima. (b) Si 2p, (c) Ir $4f_{7/2}$, (d) C 1s and (e) O 1s high resolution spectra recorded at room temperature after annealing to increasing temperature. In (c) the bottom part shows the deconvolution of selected spectra. (f) Temperature dependent BE shifts of the Si 2p, O 1s and C 1s core levels with respect to the corresponding BE values measured for the sample annealed to 1050 K.

As observed in fig. 4.20 (a) and (b), above 800 K the Si 2p core level spectrum starts shifting to higher BEs. This is parallelled by an analogous behavior observed for the the O_A component in the O 1s spectrum, which is associated to SiO_2. On the other hand, the O_B component progressively disappear, indi-

cating the thermal desorption of the interfacial oxygen from the Ir(111) surface. The loss of oxygen is also reflected in the Ir $4f_{7/2}$ core level spectrum, where, as the temperature increases, we observe a gradual decrease of the $Ir_{A\text{-}C}$ components intensity, followed by the appearance of the surface component S that was reported for Gr/Ir(111). Notably, the intensity of the S component, which is comparable to that of the pristine Gr/Ir(111) interface, demonstrates a negligible interaction between the metal surface and the SiO_2 layer. After complete desorption of the interfacial oxygen the O 1s and Si 2p spectra are both shifted by +850 meV, approaching the typical BE value reported for SiO_2/Si [57]. Figure 4.20 (d) shows how the polarization of the SiO_2 intralayer is reflected in the doping state of graphene. Similarly to what observed for Si 2p and O 1s, during sample annealing the C 1s core level shifts by 280 meV.

During the annealing procedure, the oxygen atoms that diffuse through the oxide layer partly react with Gr, causing the removal of about 18% of C atoms (after annealing to 1050 K) that most likely desorb as CO or CO_2. In this respect we can safely rule out the formation of a high density of point defects in the Gr network, such as single- and double-vacancies or Stone-Wales defects because, according to DFT calculations performed on graphite [41] and graphene [40], the presence of this kind of defects in a concentration down to 1% would result in the presence of low BE components in the C 1s spectrum, which are not experimentally observed. Therefore we believe that C removal occurs at the edges of the graphene islands, which maintain a high crystalline structure.

Figure 4.20 (f) compares the shifts of the Si 2p, O 1s and C 1s core levels with respect to the BE values measured after annealing to 1050 K as a function of the temperature. This behavior is better explained by considering the relationship which links the gate voltage V_g to the Fermi level shift ΔE_F in back gated Gr [60]:

$$\Delta E_F \propto sign(V_g) \cdot \sqrt{|V_g|}$$

In our case ΔE_{O1s} and ΔE_{Si2p} measure the local potential in the dielectric, *i.e.* V_g, while ΔE_{C1s} reflects ΔE_F, assuming a rigid shift of the C 1s core level. Therefore, ΔE_{C1s} should be proportional to $-\sqrt{\Delta E_{Si2p}}$ and $-\sqrt{\Delta E_{O1s}}$. A linear trend is indeed observed in fig. 4.21 up to 970 K, demonstrating that the heterostructure behaves as a gated plane capacitor with the *in situ* grown ultrathin SiO_2 layer acting as a homogeneous dielectric spacer. Notably, due to the high capacity of the ultrathin oxide layer, the efficiency of the electrostatic gating of graphene in this system is much higher than in conventional devices which generally use hundreds of nm thick dielectric spacers. For example, a

similar ΔE_{C1s} of 220 meV has been measured for graphene supported on a 100 nm thick Si_3N_4 layer, when applying an external voltage of about 22 V [61]. At 1050 K the capacitance of the structure decreases. This behavior can be explained in terms of morphological and structural changes occurring at high temperature in the SiO_2 layer, which degrade the electrical response.

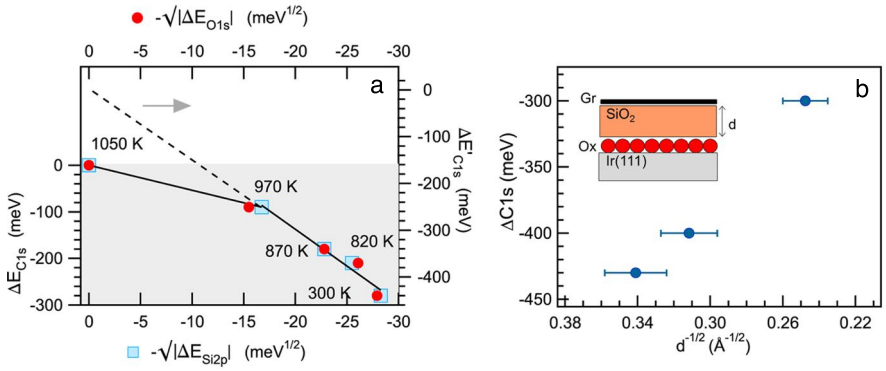

Figure 4.21: (a) ΔE_{C1s} vs. $-\sqrt{\Delta E_{Si2p}}$ (red circles) and vs $-\sqrt{\Delta E_{O1s}}$ (blue squares). The solid curves are the linear fits of the data in the low and high temperature regions. The dashed line extrapolates the behavior observed at low temperature to the complete removal of oxygen and the right scale evaluates the corresponding C 1s BE shift. (b) C 1s core level shift measured for Gr/SiO_2/O-Ir(111) samples corresponding to different oxide thickness (d) as a function of $1/\sqrt{d}$.

Our results thus show that the amount of electronegative oxygen chemisorbed on the metal surface acts as an efficient gate electrode on the oxide supported graphene. As a final part of our investigation, we explored the possibility to tune the charge state of Gr also by modifying the oxide layer thickness. Figure 4.21 shows that the ΔE_{C1s} values measured as a function of the SiO_2 layer thickness exhibit a nearly linear dependence on $1/\sqrt{d}$ as expected from a planar capacitor model.

To conclude, we presented a strategy to change the charge state of graphene by chemically modifying oxide/metal interface buried in the substrate and without the need to include doping species in the Gr lattice or to bind on top of it or below it adsorbates. Since the active interface is protected from the reactions taking place on the surface, the stability of the charge configuration is preserved. This method could be extended to any chemical species able to diffuse through the ultrathin porous oxide film and reach the oxide/metal interface, in order to induce different charge states on Gr. Moreover, the synthesis of dielectric layers other than SiO_2, such as high-k oxides, nitrides and oxynitrides, is in principle affordable. Finally, the possibility to grow high quality Gr

layers on Ir thin films [62, 63] opens the way the the possible extension beyond single crystal substrates, thus minimizing the production cost.

Bibliography

[1] K. S. Novoselov, V. I. Fal'ko, L. Colombo, P. R. Gellert, M. G. Schwab, and K. Kim. A roadmap for graphene. *Nature*, **490**(7419):192–200, 2012.

[2] M. Batzill. The surface science of graphene: Metal interfaces, CVD synthesis, nanoribbons, chemical modifications, and defects. *Surface Science Reports*, **67**(3):83–115, 2012.

[3] M. Osada and T. Sasaki. Two-Dimensional Dielectric Nanosheets: Novel Nanoelectronics From Nanocrystal Building Blocks. *Advanced Materials*, **24**(2):210–228, 2012.

[4] L. Colombo, R. M. Wallace, and R. S. Ruoff. Graphene growth and device integration. *Proceedings of the IEEE*, **101**(7):1536–1556, 2013.

[5] Y. M. Lin, C. Dimitrakopoulos, K. A. Jenkins, D. B. Farmer, H. Y. Chiu, A. Grill, and Ph. Avouris. 100-GHz transistors from wafer-scale epitaxial graphene. *Science*, **327**(5966):662–662, 2010.

[6] F. Schwierz. Graphene transistors. *Nature Nanotechnology*, **5**(7):487–496, 2010.

[7] Y. Wu, Y. M. Lin, A. A. Bol, K. A. Jenkins, F. Xia, D. B. Farmer, Y. Zhu, and Ph. Avouris. High-frequency, scaled graphene transistors on diamond-like carbon. *Nature*, **472**(7341):74–78, 2011.

[8] M. Zhi, C. Xiang, J. Li, M. Li, and N. Wu. Nanostructured carbon–metal oxide composite electrodes for supercapacitors: a review. *Nanoscale*, **5**(1):72–88, 2013.

[9] L. Peng, X. Peng, B. Liu, C. Wu, y. Xie, and G. Yu. Ultrathin two-dimensional MnO_2/graphene hybrid nanostructures for high-performance, flexible planar supercapacitors. *Nano Letters*, **13**(5):2151–2157, 2013.

[10] J. J. Yoo, K. Balakrishnan, J. Huang, V. Meunier, B. G. Sumpter, A. Srivastava, M. Conway, A. L. Mohana Reddy, J. Yu, R. Vajtai, and M. A. Pulickel. Ultrathin planar graphene supercapacitors. *Nano Letters*, **11**(4):1423–1427, 2011.

[11] J. R. Miller, R. A. Outlaw, and B. C. Holloway. Graphene double-layer capacitor with ac line-filtering performance. *Science*, **329**(5999):1637–1639, 2010.

[12] A. Hashimoto, K. Suenaga, A. Gloter, K. Urita, and S. Iijima. Direct evidence for atomic defects in graphene layers. *Nature*, **430**(7002):870–873, 2004.

[13] M. A. Fanton, J. A. Robinson, C. Puls, Y. Liu, M. J. Hollander, B. E. Weiland, M. LaBella, K. Trumbull, R. Kasarda, C. Howsare, J. Stitt, and D. W. Snyder. Characterization of graphene films and transistors grown on sapphire by metal-free chemical vapor deposition. *ACS Nano*, **5**(10):8062–8069, 2011.

[14] M. Zhou, F. L. Pasquale, P. A. Dowben, A. Boosalis, M. Schubert, V. Darakchieva, R. Yakimova, L. Kong, and J. A. Kelber. Direct graphene growth on Co_3O_4(111) by molecular beam epitaxy. *Journal of Physics: Condensed Matter*, **24**(7):072201, 2012.

[15] G. Lippert, J. Dabrowski, M. Lemme, C. Marcus, O. Seifarth, and G. Lupina. Direct graphene growth on insulator. *Physica Status Solidi B*, **248**(11):2619–2622, 2011.

[16] R. Addou, A. Dahal, and M. Batzill. Growth of a two-dimensional dielectric monolayer on quasi-freestanding graphene. *Nature Nanotechnology*, **8**(1):41–45, 2013.

[17] L. Liao, J. Bai, Y. Qu, Y.-C. Lin, Y. Li, Y. Huang, and X. Duan. High-κ oxide nanoribbons as gate dielectrics for high mobility top-gated graphene transistors. *Proceedings of the National Academy of Sciences*, **107**(15):6711–6715, 2010.

[18] S. Jandhyala, G. Mordi, B. Lee, G. Lee, C. Floresca, P. R. Cha, J. Ahn, R. M. Wallace, Y. J Chabal, M. J. Kim, L. Colombo, C. Kyeongjae, and K. Jiyoung. Atomic layer deposition of dielectrics on graphene using reversibly physisorbed ozone. *ACS Nano*, **6**(3):2722–2730, 2012.

[19] L. Omiciuolo, E. R. Hernández, E. Miniussi, F. Orlando, P. Lacovig, S. Lizzit, T. O. Menteş, A. Locatelli, R. Larciprete, M. Bianchi, S. Ulstrup, P. Hofmann, D. Alfé, and A. Baraldi. Bottom-up approach for the low-cost synthesis of graphene-alumina nanosheet interfaces using bimetallic alloys. *Nature Communications*, **5**, 2014.

[20] O. Bikondoa, G. R. Castro, X. Torrelles, F. Wendler, and W. Moritz. Surface-induced disorder on the clean Ni_3Al(111) surface. *Physical Review B*, **72**(19):195430, 2005.

[21] E. Vesselli, L. Bianchettin, A. Baraldi, A. Sala, G. Comelli, S. Lizzit, L. Petaccia, and S. de Gironcoli. The $Ni_3Al(111)$ surface structure: experiment and theory. *Journal of Physics: Condensed Matter*, **20**(19):195223, 2008.

[22] R. Nyholm, J. N. Andersen, J. F. van Acker, and M. Qvarford. Surface core-level shifts of the Al(100) and Al(111) surfaces. *Physical Review B*, **44**(19):10987, 1991.

[23] A. Stierle, C. Tieg, H. Dosch, V. Formoso, E. Lundgren, J. N. Andersen, L. Köhler, and G. Kresse. Surface core level shift observed on NiAl(110). *Surface Science*, **529**(3):L263–L268, 2003.

[24] A. Grüneis, K. Kummer, and D. V. Vyalikh. Dynamics of graphene growth on a metal surface: a time-dependent photoemission study. *New Journal of Physics*, **11**(7):073050, 2009.

[25] L. L. Patera, C. Africh, R. S. Weatherup, R. Blume, S. Bhardwaj, C. Castellarin-Cudia, A. Knop-Gericke, R. Schloegl, G. Comelli, S. Hofmann, and C. Cepek. In situ observations of the atomistic mechanisms of Ni catalyzed low temperature graphene growth. *ACS Nano*, **7**(9):7901–7912, 2013.

[26] J. Lahiri, T. Miller, L. Adamska, I. I Oleynik, and M. Batzill. Graphene growth on Ni(111) by transformation of a surface carbide. *Nano Letters*, **11**(2):518–522, 2010.

[27] R. Addou, A. Dahal, P. Sutter, and M. Batzill. Monolayer graphene growth on Ni(111) by low temperature chemical vapor deposition. *Applied Physics Letters*, **100**(2):021601, 2012.

[28] A. B. Preobrajenski, M. L. Ng, A. S. Vinogradov, and N. Mårtensson. Controlling graphene corrugation on lattice-mismatched substrates. *Physical Review B*, **78**(7):073401, 2008.

[29] W. Zhao, S. M. Kozlov, O. Höfert, K. Gotterbarm, M. P. A. Lorenz, F. Vines, C. Papp, A. Görling, and H. P. Steinrück. Graphene on ni(111): coexistence of different surface structures. *The Journal of Physical Chemistry Letters*, **2**(7):759–764, 2011.

[30] F. B. Bianchini, L. L. Patera, M. Peressi, C. Africh, and G. Comelli. Atomic Scale Identification of Coexisting Graphene Structures on Ni(111). *The Journal of Physical Chemistry Letters*, **5**(3):467–473, 2014.

[31] F. Mittendorfer, A. Garhofer, J. Redinger, J. Klimeš, J. Harl, and G. Kresse. Graphene on Ni(111): Strong interaction and weak adsorption. *Physical Review B*, **84**(20):201401, 2011.

[32] A. Varykhalov, J. Sánchez-Barriga, A. M. Shikin, C. Biswas, E. Vescovo, A. Rybkin, D. Marchenko, and O. Rader. Electronic and magnetic properties of quasifreestanding graphene on Ni. *Physical Review Letters*, **101**(15):157601, 2008.

[33] P. Sutter, J. T. Sadowski, and E. A. Sutter. Chemistry under cover: Tuning metal-graphene interaction by reactive intercalation. *Journal of the American Chemical Society*, **132**(23):8175–8179, 2010.

[34] R. Larciprete, S. Ulstrup, P. Lacovig, M. Dalmiglio, M. Bianchi, F. Mazzola, L. Hornekær, F. Orlando, A. Baraldi, Ph. Hofmann, and S. Lizzit. Oxygen switching of the epitaxial graphene–metal interaction. *ACS Nano*, **6**(11):9551–9558, 2012.

[35] C. Riedl, C. Coletti, T. Iwasaki, A. A. Zakharov, and U. Starke. Quasi-freestanding epitaxial graphene on SiC obtained by hydrogen intercalation. *Physical Review Letters*, **103**(24):246804, 2009.

[36] A. M. Shikin, G. V. Prudnikova, V. K. Adamchuk, F. Moresco, and K. H. Rieder. Surface intercalation of gold underneath a graphite monolayer on Ni(111) studied by angle-resolved photoemission and high-resolution electron-energy-loss spectroscopy. *Physical Review B*, **62**(19):13202, 2000.

[37] E. Vesselli, A. Baraldi, S. Lizzit, and G. Comelli. Large interlayer relaxation at a metal-oxide interface: the case of a supported ultrathin alumina film. *Physical Review Letters*, **105**(4):046102, 2010.

[38] N. M. Martin, J. Knudsen, S. Blomberg, J. Gustafson, J. N. Andersen, E. Lundgren, H. H. Ingelsten, P. A. Carlsson, M. Skoglundh, and A. Stierle. High-resolution core-level spectroscopy study of the ultrathin aluminum oxide film on NiAl(110). *Physical Review B*, **83**(12):125417, 2011.

[39] S. Lizzit, R. Larciprete, P. Lacovig, M. Dalmiglio, F. Orlando, A. Baraldi, L. Gammelgaard, L. Barreto, M. Bianchi, E. Perkins, and Ph. Hofmann. Transfer-free electrical insulation of epitaxial graphene from its metal substrate. *Nano Letters*, **12**(9):4503–4507, 2012.

[40] T. Susi, M. Kaukonen, P. Havu, M. P. Ljungberg, P. Ayala, and E. I. Kauppinen. Core level binding energies of functionalized and defective graphene. *Beilstein Journal of Nanotechnology*, **5**(1):121–132, 2014.

[41] A. Barinov, O. B. Malcioglu, S. Fabris, T. Sun, L. Gregoratti, M. Dalmiglio, and M. Kiskinova. Initial stages of oxidation on graphitic surfaces: photoemission study and density functional theory calculations. *The Journal of Physical Chemistry C*, **113**(21):9009–9013, 2009.

[42] B. Maruyama and F. S. Ohuchi. H_2O catalysis of aluminum carbide formation in the aluminum-silicon carbide system. *Journal of Materials Research*, **6**(06):1131–1134, 1991.

[43] Benji Maruyama, Fumio S Ohuchi, and L. Rabenberg. Chemical interactions in the Al-C and Al-Si-C systems. *Mater. Res. Soc. Symp. Proc.*, 170:167, 1990.

[44] S. Tanuma, C. J. Powell, and D. R. Penn. Calculations of electron inelastic mean free paths. *Surface Interface Analysis*, **21**:165–176, 1993.

[45] K. S. Novoselov, A. K. Geim, S. V. Morozov, D. Jiang, M. I. Katsnelson, I. V. Grigorieva, S. V. Dubonos, and A. A. Firsov. Two-dimensional gas of massless Dirac fermions in graphene. *Nature*, **438**(7065):197–200, 2005.

[46] V. Geringer, M. Liebmann, T. Echtermeyer, S. Runte, M. Schmidt, R. Rückamp, M. C Lemme, and M. Morgenstern. Intrinsic and extrinsic corrugation of monolayer graphene deposited on SiO_2. *Physical Review Letters*, **102**(7):076102, 2009.

[47] M. Ishigami, J. H. Chen, W. G. Cullen, M. S. Fuhrer, and E. D. Williams. Atomic structure of graphene on SiO_2. *Nano Letters*, **7**(6):1643–1648, 2007.

[48] A. Locatelli, K. R Knox, D. Cvetko, T. O. Mentes, M. A. Nino, S. Wang, M. B. Yilmaz, P. Kim, R. M. Osgood Jr, and A. Morgante. Corrugation in exfoliated graphene: An electron microscopy and diffraction study. *ACS Nano*, **4**(8):4879–4889, 2010.

[49] U. Martinez, L. Giordano, and G. Pacchioni. Tuning the work function of ultrathin oxide films on metals by adsorption of alkali atoms. *Journal of Chemical Physics*, **128**(16):164707–164707, 2008.

[50] T. Jaouen, S. Tricot, G. Delhaye, B. Lépine, D. Sébilleau, G. Jézéquel, and Ph. Schieffer. Layer-resolved study of Mg atom incorporation at the

MgO/Ag(001) buried interface. *Physical Review Letters*, **111**(2):027601, 2013.

[51] R. Włodarczyk, M. Sierka, J. Sauer, D. Löffler, J. J. Uhlrich, X. Yu, B. Yang, I. M. N. Groot, S. Shaikhutdinov, and H. J. Freund. Tuning the electronic structure of ultrathin crystalline silica films on Ru(0001). *Physical Review B*, **85**(8):085403, 2012.

[52] D. Löffler, J. J. Uhlrich, M. Baron, B. Yang, X. Yu, L. Lichtenstein, L. Heinke, C. Büchner, M. Heyde, S. Shaikhutdinov, H. G. Freund, R. Wlodarczyk, M. Sierka, and J. Sauer. Growth and structure of crystalline silica sheet on Ru(0001). *Physical Review Letters*, **105**(14):146104, 2010.

[53] R. Larciprete, P. Lacovig, F. Orlando, M. Dalmiglio, L. Omiciuolo, A. Baraldi, and S. Lizzit. Chemical gating of epitaxial graphene through ultrathin oxide layers. *Nanoscale*, **7**(29):12650–12658, 2015.

[54] P. Lacovig, M. Pozzo, D. Alfé, P. Vilmercati, A. Baraldi, and S. Lizzit. Growth of dome-shaped carbon nanoislands on Ir(111): the intermediate between carbidic clusters and quasi-free-standing graphene. *Physical Review Letters*, **103**(16):166101, 2009.

[55] M. Bianchi, D. Cassese, A. Cavallin, R. Comin, F. Orlando, L. Postregna, E. Golfetto, S. Lizzit, and A. Baraldi. Surface core level shifts of clean and oxygen covered Ir(111). *New Journal of Physics*, **11**(6):063002, 2009.

[56] L. Meng, R. Wu, H. Zhou, G. Li, Y. Zhang, L. Li, Y. Wang, and H. J. Gao. Silicon intercalation at the interface of graphene and Ir(111). *Applied Physics Letters*, **100**(8):083101, 2012.

[57] F. J. Himpsel, F. R. McFeely, A. Taleb-Ibrahimi, J. A. Yarmoff, and G. Hollinger. Microscopic structure of the SiO_2/Si interface. *Physical Review B*, **38**(9):6084, 1988.

[58] G. Hollinger, S. J. Sferco, and M. Lannoo. Deviation from the classical 4: 2 coordination in very thin SiO_2 films grown on silicon. *Physical Review B*, **37**(12):7149, 1988.

[59] U. Martinez, J. F. Jerratsch, N. Nilius, L. Giordano, G. Pacchioni, and H. J. Freund. Tailoring the interaction strength between gold particles and silica thin films via work function control. *Physical Review Letters*, **103**(5):056801, 2009.

[60] Y. J. Yu, Y. Zhao, S. Ryu, L. E. Brus, K. S. Kim, and P. Kim. Tuning the graphene work function by electric field effect. *Nano Letters*, **9**(10):3430–3434, 2009.

[61] M. Copuroglu, P. Aydogan, E. O. Polat, C. Kocabas, and S. Süzer. Gate-tunable photoemission from graphene transistors. *Nano Letters*, **14**(5):2837–2842, 2014.

[62] C. Struzzi, N. I. Verbitskiy, A. V. Fedorov, A. Nefedov, O. Frank, M. Kalbac, G. Di Santo, M. Panighel, A. Goldoni, J. Gärtner, W. Weber, M. Weinl, M. Schreck, C. Woll, H. Sachdev, A. Grüneis, and L. Petaccia. High-quality graphene on single crystal Ir(111) films on Si(111) wafers: Synthesis and multi-spectroscopic characterization. *Carbon*, **81**:167–173, 2015.

[63] C. Vo-Van, A. Kimouche, A. Reserbat-Plantey, O. Fruchart, P. Bayle-Guillemaud, N. Bendiab, and J. Coraux. Epitaxial graphene prepared by chemical vapor deposition on single crystal thin iridium films on sapphire. *Applied Physics Letters*, **98**(18):181903, 2011.

5 Synthesis and characterization of graphene-like two dimensional systems

The first isolation of graphene and the subsequent discovery of its unusual properties have definitely led to a remarkable interest from both the scientific and the industrial communities. However, the integration of pristine Gr in the fabrication of high efficiency logical circuits is limited by the absence of a band gap. For this reason, in the last ten years, Gr research has broaden to a much wider set of Gr-related systems. For example, nanographene and Gr nanoribbons has proved to be an effective way to tailor Gr electronic properties [1, 2, 3]. In particular, it has been demonstrated the possibility to open an energy gap at the Fermi level, with clear interesting applications in electronics. However, the band gap obtained with this approach is highly dependent on the dimensions and edge terminations of these islands, thus implying the need of a precise control on these parameters during the growth. A previosuly reported and promising strategy to achieve the growth of Gr nanoribbons and nanoflakes with atomic width control consists of a bottom-up approach based on surface assisted cyclodehydrogenation of suitable precursors [4, 5, 6, 7, 8].

The first part of this chapter is therefore devoted to understanding the dehydrogenation mechanism of coronene on Ir(111), up to the formation of dome-shaped Gr nanoflakes. The exotic dehydrogenation path, which includes molecular lifting, twisting, and curling, was characterized by a combination of several different experimental techniques, including adsorption spectroscopy, photoelectron spectroscopy, electron diffraction, and thermal desorption spectroscopy. Additional extensive DFT calculations were performed by a collaborating group at the University College London in order to get the atomistic details of the process. Besides the fundamental interest in the reaction kinetics, this complex reactions path could be exploited to produce functionalized nanographene flakes, or to encapsulate single atoms beneath the C domes.

On the other hand, after Gr first isolation other 2D layered materials, such as

hexagonal Boron Nitride (*h*-BN), transition metal dichalcogenides, and transition metal oxides have gained renewed interest. The common feature of these layered materials is that they present a stacked bulk structure, with strong covalent in-plane bonds within the crystal planes and weak van der Waals interactions between adjacent planes. Such materials present a large variety of electronic transport properties, from insulator to metal, and display a number of interesting properties. For example molybdenum disulfide (MoS_2), which is formed by an hexagonal layer of Mo atoms sandwiched between two layers of S atoms, is an indirect band semiconductor [9, 10]. On the contrary, *h*-BN is a wide band insulator [11, 12]. Because of their distinct properties and high specific surface areas, these 2D materials could have important applications in different technological fields, including electronics, spintronics, catalysis, chemical and biological sensors, supercapacitors, solar cells, and lithium ion batteries. Moreover, the natural layered configurations of these materials suggests compelling applications in the production of stacked heterostructures with tailored properties, by putting different layers on top of each other [13].

In the 2D materials framework, *h*-BN is particularly important due to its particular structure. It presents the same geometrical configuration of Gr, with almost the same lattice parameter, but the two C atoms inside Gr unit cell are replaced by B and N atoms. Moreover *h*-BN presents a wide band gap of more than 6 eV [14]. Thanks to these properties, the use of *h*-BN as a dielectric substrate for graphene transistors has been shown, for example, to significantly improve the carrier mobility in graphene [15]. However, unlike Gr, it is challenging to obtain large single crystalline *h*-BN domains because of the formation of rotated phases that give rise to grain boundaries and other 1D defects [16]. For example, nucleation of rotational domains has been reported for weakly interacting systems, such as Pd(111) [17], Cu(111) [18], and Ag(111) [19], as well as in the case of substrates with strongly chemisorbed *h*-BN monolayers, such as Ni(111) [20] and Rh(111) [21]. To date much effort is still needed in order to achieve the highest quality for *h*-BN films on metal surfaces.

In the second part of this chapter, a method for the synthesis of large single domain *h*-BN sheets is presented. We demonstrate how, by properly adjusting the growth parameters, temperature programmed thermal dissociation of borazine ($B_3N_3H_6$) can be exploited to obtain singly oriented *h*-BN domains on Ir(111). The system was characterized by a combination of spectroscopic and diffraction techniques.

5.1 Coronene on Ir(111): the complex path from molecular adsorption to nanographene formation

This section is devoted to the characterization of the thermally assisted cyclodehydrogenation of coronene ($C_{24}H_{12}$) on Ir(111), up to the formation of nanographene flakes. Commercially available coronene powder (99%, purified by sublimation) was used throughout the experiment. Coronene molecules were evaporated in vacuum using a custom evaporator consisting of a Boron Nitride (BN) crucible wrapped with a 1mm diameter Ta wire used to heat it by resistive dissipation. Before the experiment, the crucible was annealed in vacuum to increasing temperatures up to 670 K, in order to clean the evaporation cell from impurities. During evaporation, the temperature inside the crucible was measured trough a K-type thermocouple in thermal contact with the coronene powder. Coronene evaporation was achieved by keeping the crucible at a fixed temperature in the 400 to 440 K range. Before each evaporation, coronene was further purified in vacuum by means of short annealing cycles up to 450 K, while monitoring the chamber residual gas composition with a residual gas analyzer system. During evaporation the sample was kept at room temperature.

5.1.1 Coronene adsorption on Ir(111)

Figure 5.1 reports the C K-edge absorption spectra measured at two different incident angles for sub-monolayer coronene coverage. By comparison to literature [22], resonances in the 284÷289 eV range are ascribed to C 1s $\rightarrow \pi^*$ transistions, while the features above 290 eV are assigned to C 1s $\rightarrow \sigma^*$ transitions. The presence of multiple components in each spectral region can be explained in terms of C 1s $\rightarrow$ LUMO+*n* transitions, as well as by initial state effects given by the presence of non equivalent C atoms due to the interaction with the surface. The most noticeable result is the strongly reduced intensity of the C 1s $\rightarrow \pi^*$ transition components and the increased spectral weight in the σ^* region when the electric field is almost normal to the surface (red curve), indicating a nearly flat adsorption geometry. In fact, the σ^* molecular orbitals for sp^2 C compounds, like coronene, are parallel to the molecular plane, while the π^* are normal to it. Thus, if the molecules lie flat on the surface, the C 1s $\rightarrow$ σ^* transition probability is maximized when the impinging electric field vector is parallel to the surface, while C 1s $\rightarrow \pi^*$ transitions are maximized when the electric vector is normal to the surface.

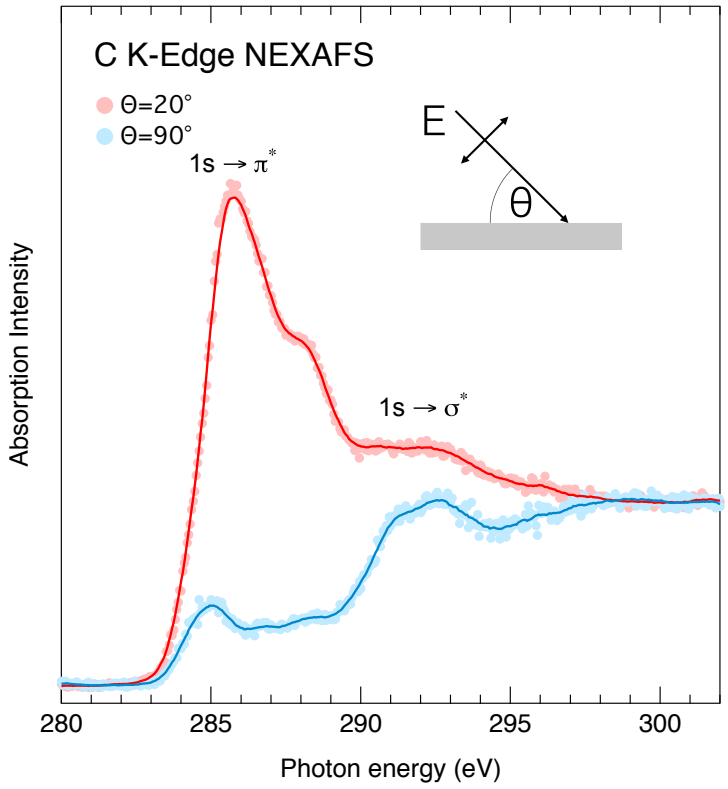

Figure 5.1: C K-edge NEXAFS spectra acquired after deposition of sub-monolayer coverage of coronene on Ir(111) at room temperature. The spectra were acquired with linearly polarized radiation, with the electric field either parallel (blue dots) or almost normal (red dots) to the crystal surface. Corresponding smoothed spectra (solid lines) are also presented.

The electronic structure of coronene upon adsorption was checked by UPS and ARPES measurements, presented in fig. 5.2. The valence band (VB) spectra (fig. 5.2 (a)) have been measured at normal emission after different surface preparations. The spectrum acquired after deposition of a monolayer of coronene on clean Ir(111) (light blue), shows several peaks attributed to molecular signals, since they appear at different binding energies with respect to those present in the spectrum of clean Ir(111) (gray), which is dominated by the large d-band density of states. These molecular states can be associated to non-dispersing features in the ARPES maps (fig. 5.2 (c,e)), as underlined also by an Energy Dispersion Curve (EDC) acquired near the M point, where the substrate density of state is almost flat (fig. 5.2 (b,d)). In particular four peaks are observed ($M_{1\text{-}4}$) at 1.8, 2.4, 4.1, and 5.2 eV, attributed to hybridization of the coronene molecular orbitals with the Ir 5d bands. The Ir(111) surface's ability in creating strong π bonds to poly aromatic hydrocarbons (PAHs) is confirmed by considering the spectral components appearing for other coronene-based interfaces with weaker interactions, *i.e.* coronene multilayers grown on Ir(111) (fig. 5.2 (a), yellow) and for coronene on Gr/Ir(111) (fig. 5.2 (a), red). In these cases, besides the rigid shift induced by different charge transfer, the VB spectra are a clear fingerprint of the coronene molecular orbitals (marked with vertical lines in the figure), whose binding energy distribution is in excellent agreement with previous experimental findings and theoretical calculations [23, 24, 25].

To further investigate the modifications to coronene electronic structure induced upon adsorption, we acquired high-resolution XPS C 1s core level spectra at different molecular coverages (fig. 5.3, shades of grey). A three-peak spectral shape was observed, in contrast to the two-peak lineshape observed for coronene on Gr (red curve), and for gas phase coronene [22]. Moreover, the C 1s spectra acquired at different coverages show the same line shape regardless of the coronene amount, suggesting that the adsorption configuration and site are not modified by intermolecular interactions in denser molecular layers. It should be noted that the presence of three components cannot be simply justified as due to the geometrically non equivalent C atoms forming the inner, middle, and outer rings in the molecule, since the spectral weight does not match the 1:1:2 ratio corresponding to the population of those atoms.

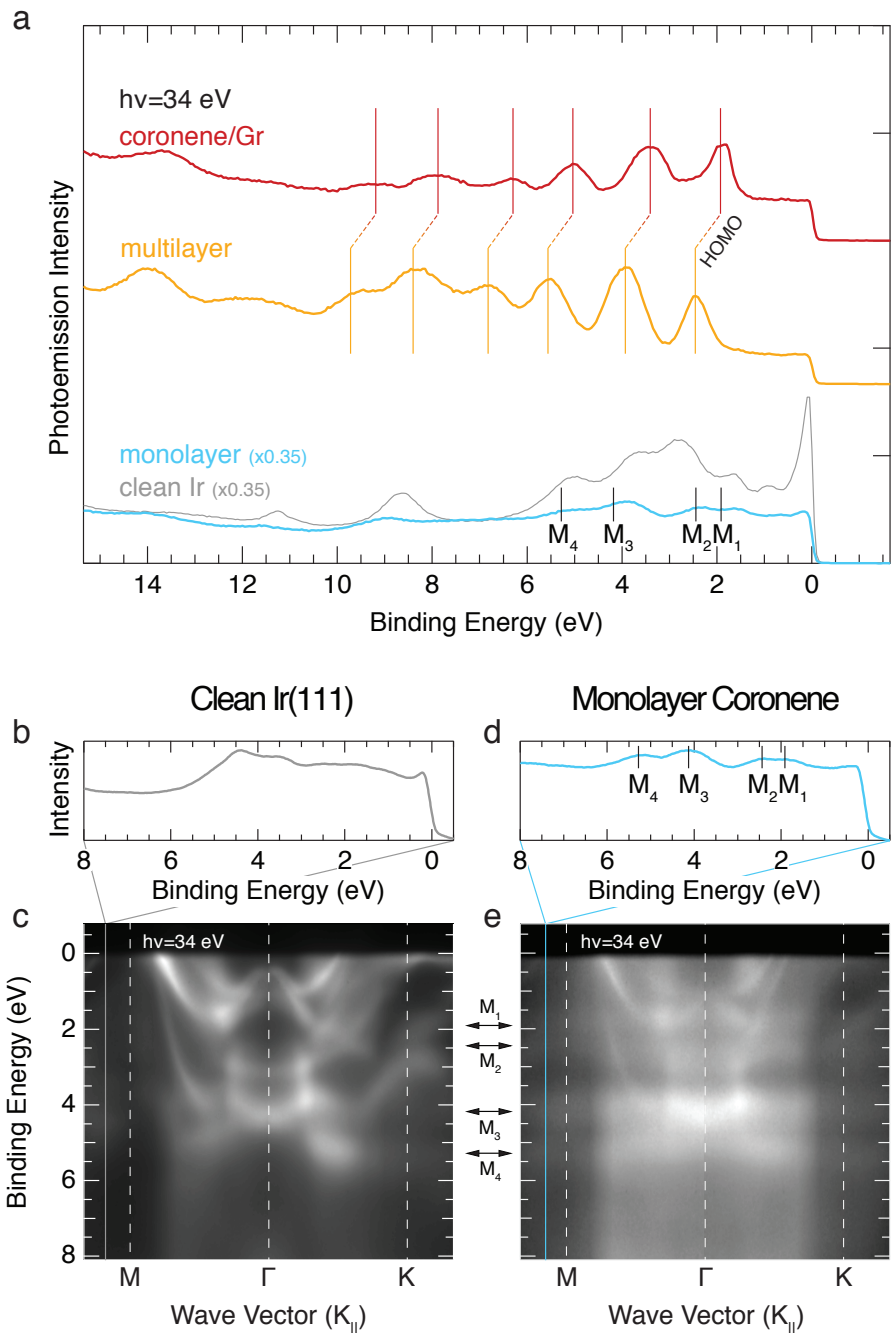

Figure 5.2: (a) Valence band spectra acquired at 34 eV photon energy for the clean Ir(111) surface (grey curve), monolayer coronene on Ir(111) (light blue curve), multilayer coronene on Ir(111) (yellow curve), and monolayer coronene on Gr/Ir(111) (red curve). (b) Energy Dispersion Curve (EDC) for the clean Ir(111) obtained by selecting a vertical cut of the corresponding ARPES image at the M point. (c) ARPES map of the clean Ir(111) acquired at hv=34 eV. (d) EDC curve for a monolayer of coronene on Ir(111) obtained by selecting a vertical cut of the corresponding ARPES image at the M point. (e) ARPES map (hv=34 eV) after deposition of a monolayer of coronene on Ir(111). Coronene molecular levels ($M_{1\text{-}4}$) are shown superimposed to the spectra.

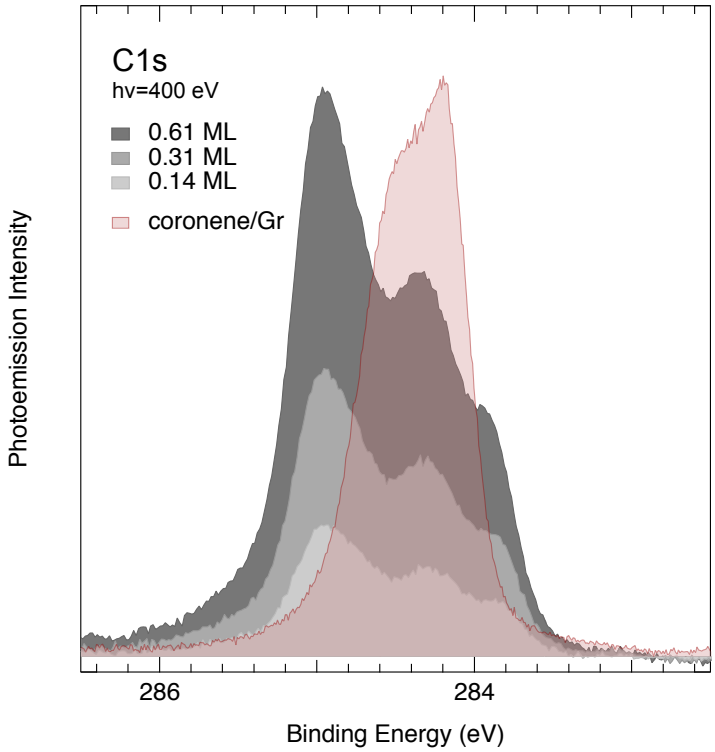

Figure 5.3: C 1s spectra acquired at hv=400 eV for different coverages of coronene on Ir(111) (shades of grey), compared with a similar coverage of coronene on Gr (red).

In order to get details on the coronene adsorption geometry, and on the origin of the different core level components, we performed DFT calculations. All the DFT calculations were performed for a single coronene molecule adsorbed on a 9×9 Ir surface. Figure 5.4 shows the different coronene configurations that were probed by our DFT calculations, including molecules with symmetry axes oriented along different directions, in different adsorption sites of the Ir(111) surface, and also in non-planar configurations. Figure 5.5 (a) shows instead the minimum energy configuration (-1.46 eV adsorption energy[1]), corresponding to coronene adsorbed with the inner C hexagon in bridge-site and the molecular axis aligned parallel to the [101] direction of Ir(111).

[1]The adsorption energy is calculated with respect to the gas phase molecule.

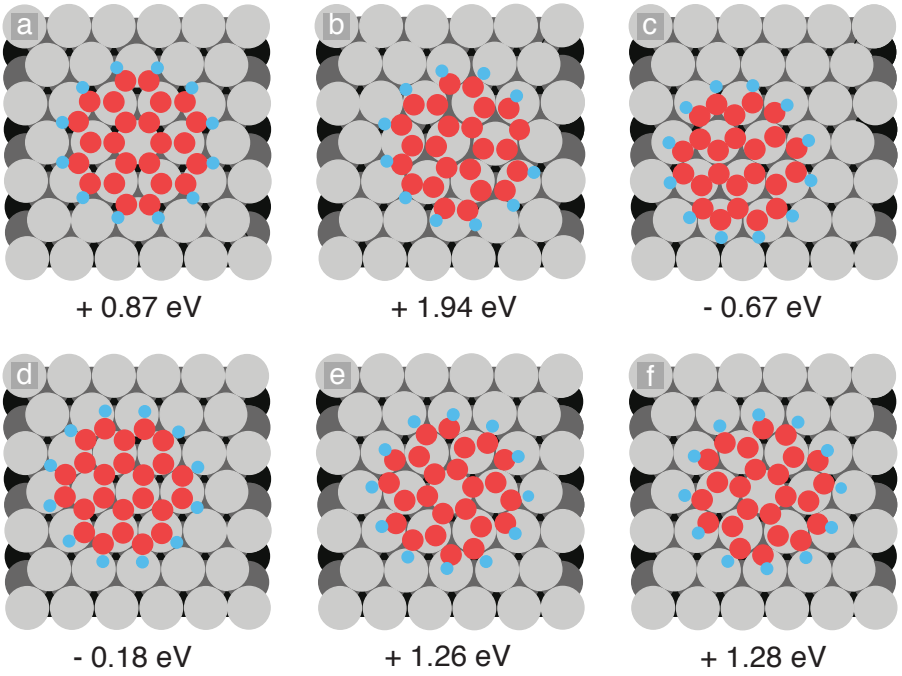

Figure 5.4: (a-f) Different coronene configurations used in DFT calculations. The adsorption energies are calculated with respect to the gas phase molecule. Positive adsorption energies correspond to non binding configuration.

Upon adsorption the molecules slightly bend to assume a bowl-like shape (side view shown in fig. 5.5), usually associated to π-conjugated compounds known as buckybowls or π-bowls [26, 27]. In our case, coronene form an upward bowl, since the C atoms belonging to the inner ring are about 0.23 Å closer to the surface with respect to C atoms in the outer ring (see fig. 5.5). The bowl-shaped geometry is enhanced by the hydrogen atoms displaying an average height of 2.74 Å, 0.7 Å farther from the surface than the inner C atoms, and a C-H bond angle ranging from 22° to 39° with respect to the Ir surface plane. To verify the consistency of the minimum energy adsorption configuration, we computed the C 1s core level BEs for each of the 24 C atoms of the molecules. The good agreement between experimental and simulated data, reported in fig. 5.6, strongly supports the DFT calculated molecular adsorption geometry. Moreover, our results suggest that the C 1s core level BEs are strongly influenced both by the C-surface distance (C atoms in the central ring showing the highest BEs), and by the position with respect to the surface Ir atoms. This is especially true when considering the C atoms forming the outer ring, whose BE is influenced by the interaction with the substrate Ir atoms.

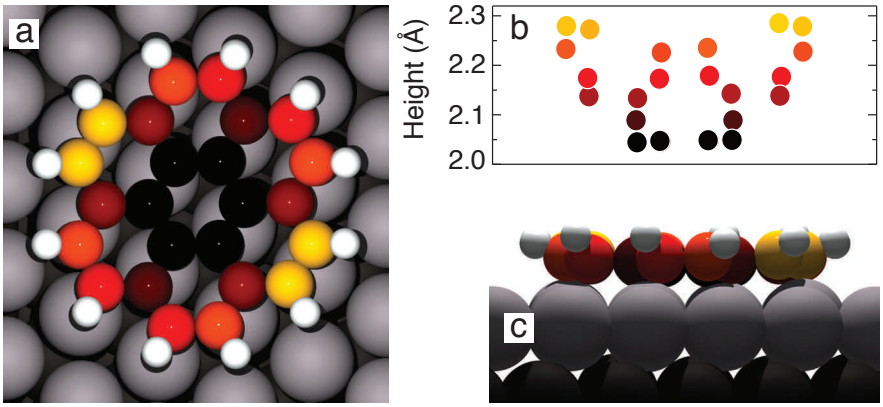

Figure 5.5: (a) Top- and (c) side-view of the minimum energy adsorption configuration of coronene on Ir(111), as obtained by DFT calculations. The color scale reflects the separation between the C atoms and the substrate beneath. (b) Computed distance from the surface for the non equivalent C atoms inside the coronene molecule.

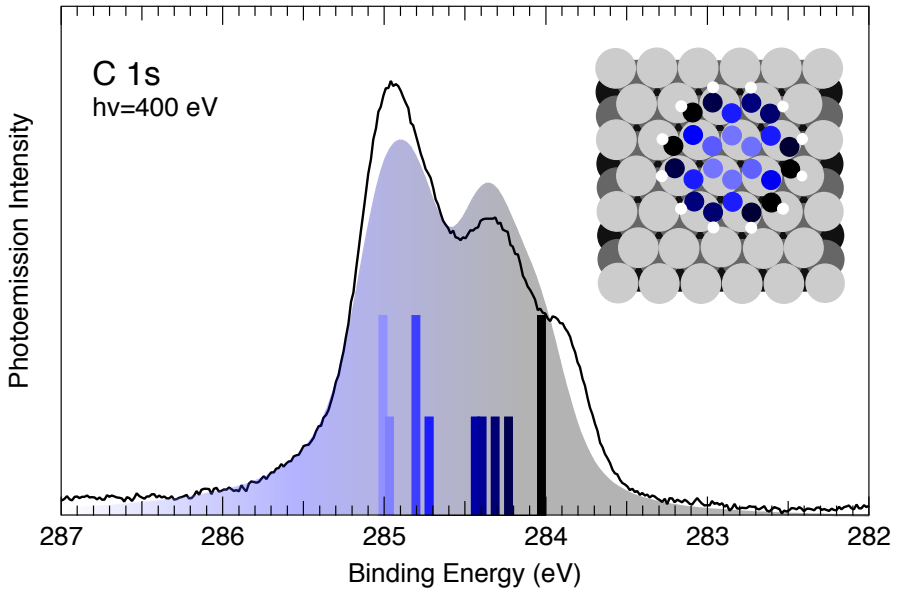

Figure 5.6: Experimental (black line) and DFT simulated (blue shades) C 1s core level spectra. An histogram of the calculated C 1s BEs is reported superimposed. The inset shows the minimum energy adsorption configuration model, with a color scale reflecting the C 1s BE of each C atom.

5.1.2 Temperature promoted coronene dehydrogenation

In order to characterize the mechanism of coronene dissociation we started from TPD measurements, in the 150-950 K range, to find the threshold of hydrogen desorption (m/z=2), which can be used a fingerprint of C-H break-up. Desorption spectra corresponding to different coronene coverages, reported in red scale in fig. 5.7(a), indicate that gas phase H_2 can be detected only above 500 K, with a maximum desorption rate around 650 K. To verify that the molecules do not undergo any dissociation already at room temperature, we compared the TPD data to a similar H_2 desorption experiment starting from hydrogen adsorbed on clean Ir(111) at 100 K (grey scale in fig. 5.7 (a)).

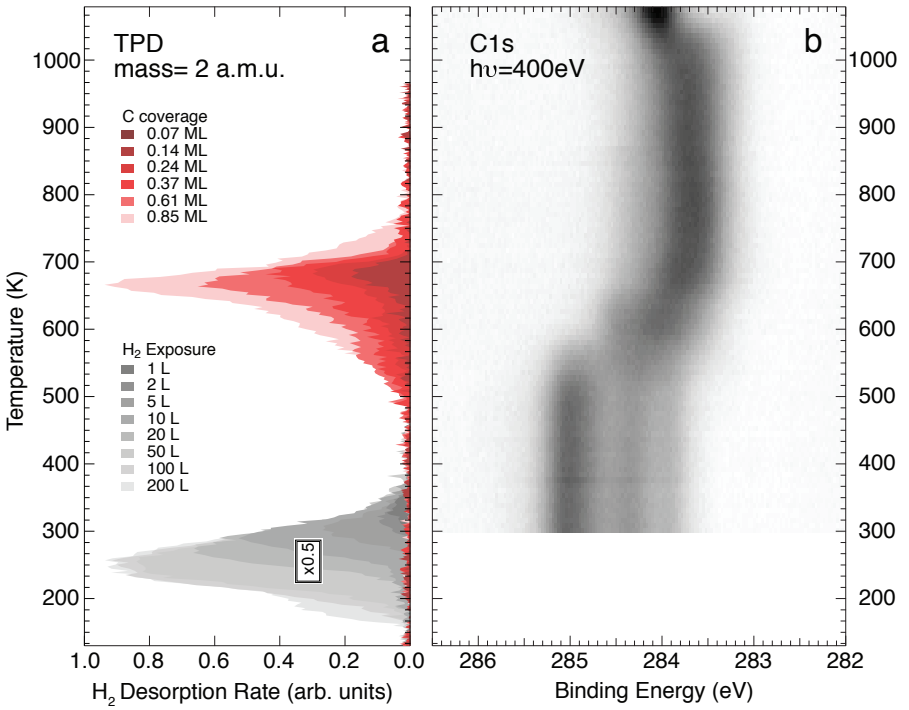

Figure 5.7: (a) Temperature programmed desorption spectra of m/z = 2 after coronene deposition at T = 300 K (red scale), and after molecular hydrogen adsorption at T = 100 K (grey scale, intensity rescaled by a factor 0.5). (b) 2D plot of the temperature dependent C 1s core level spectra (about 100 spectra). Each horizontal cut in the figures corresponds to a single photoemission spectrum acquired at a given temperature and its intensity is plotted using a grey-scale.

It is known that H_2 adsorbs dissociatively on Ir(111) [28, 29] and that the onset of desorption is indicative of the recombination of two H atoms after surface diffusion. The large difference in H_2 formation temperature, as well as the lack

of any overlap on the temperature scale of the two desorption experiments, is a clear proof that the coronene molecules do not dissociate upon adsorption, and that the first C-H breakup occurs only around 500 K.

Coronene dissociation was monitored *in-situ* by means of fast-XPS measurements. The 2D plot reported in fig. 5.7 (b) shows the evolution of the C 1s core level spectrum during a linear temperature ramp (0.25 K/s) from 300 to 1080 K. As expected from the desorption measurements, the spectrum does not change in the initial stage of the ramp, and only above 525 K, corresponding to the onset of the desorption spectra, clear modifications are observed. The spectral weight gradually shifts to lower BE, reaching a stable situation above 700 K, when the TPD results shows that all the hydrogen atoms have desorbed. Only above 1000 K the C 1s signal starts shifting back to higher BE, eventually reaching, above 1050 K, the value of 284.10 eV, which is a clear fingerprint of graphene formation [30, 31]. It is worth stressing the fact that, during the dissociation process, there is no loss in the overall C 1s intensity, suggesting that the energy barrier for C-H bond cleavage is significantly lower than that for desorption of the intact molecule or C containing species. Unambiguous chemical assignment of the experimentally observed C 1s core-level line shape is, however, not easy, due to the high number of possible configurations of the dehydrogenated transient products.

In order to classify the C 1s spectral sequence, and to gain an insight on the atomistic details of the kinetics of coronene dissociation, we resorted to DFT performing extensive calculations of the energy barriers between the computed intermediate species, using the Nudged Elastic Band (NEB) method [32]. Figure 5.8 shows the twelve intermediate configurations corresponding to the energetically most favorable reaction pathway for breaking the C-H bonds in n sequential steps (with n from 1 to 12), leaving the dehydrogenated molecules and an additional single H atom on the surface. The energy diagrams reported below each configuration are given with respect to the energy of the n-1 configuration, being n=0 the intact coronene molecule. It is worth stressing that, despite the higher final state energy of each dehydrogenation step, the reaction can easily proceeds because, at the temeperatures of our experiments, the H atoms can diffuse very rapidly on the surface and form H_2 that immediately desorbs, thus preventing the reverse reaction. Close inspection of the images shown in fig. 5.8 outlines the exotic dissociation path that the molecules undergo up to the formation of nanographene flakes. The stepwise dehydrogenation mechanism appears to be driven by the proximity of the C outer ring atom to the final adsorption position.

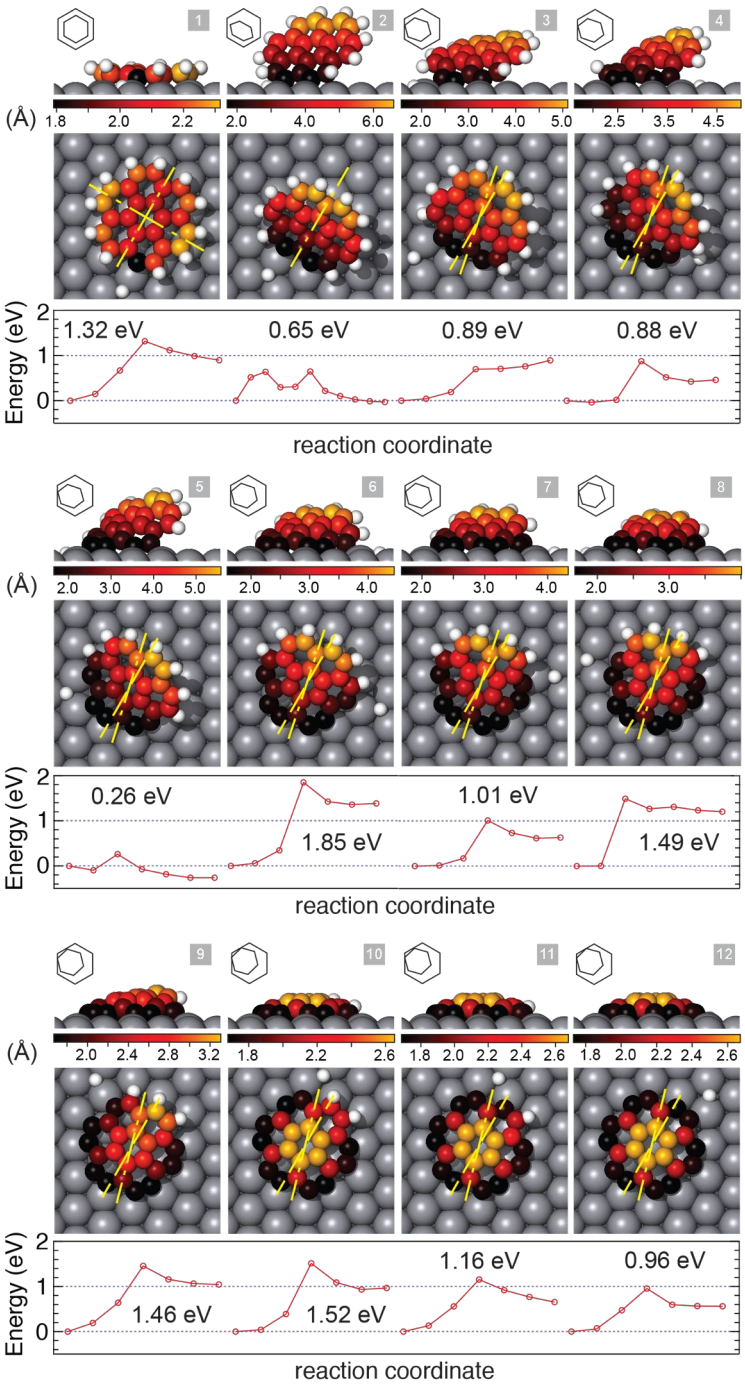

Figure 5.8: Illustration of the side and top views of the $C_{24}H_{12}$ dehydrogenation through the sequential cleavage of the $n = 12$ C-H bonds. Different colors correspond to different C-metal substrate heights. The colors have been rescaled in each step to emphasize the geometrical differences in each configuration (the height scale in Å is also reported for each step of the reaction). Above each illustration, a schematic representation of the coronene to Ir relative orientation is reported. Yellow dash-dotted lines in steps 1-2 represent the symmetry axes shared by the adsorbed coronene molecule and the Ir substrate. In steps $n = 3$-12, the dashed line represents the original coronene orientation, while the dash- dotted line represents the current one.

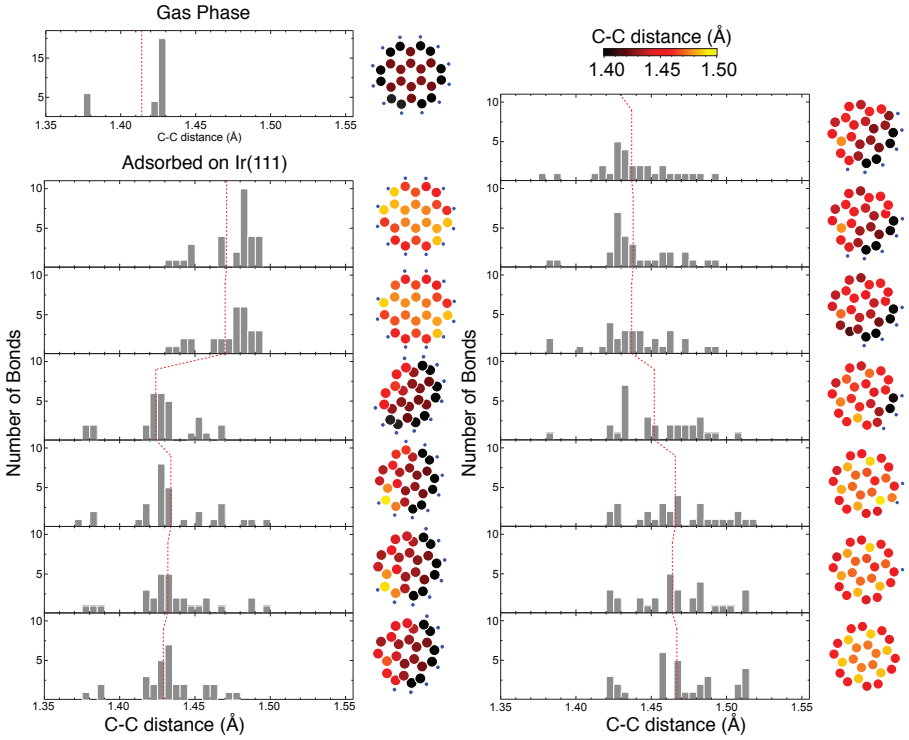

Figure 5.9: (left) C-C bond length histograms for gas phase (top), and adsorbed coronene during dehydrogenation, as obtained from DFT calculations. All the 30 C-C bonds were included. The average C-C bond length for each dissociation step is also reported (dashed red line). (right) Schematic representation of gas phase (top), and adsorbed coronene during dehydrogenation of Ir(111). The C atoms are colored according to the mean distance from the 3 (or 2) nearest neighbors. The color scale is reported on top.

Upon adsorption, the molecules have significant internal C-C strain with respect to the gas phase configuration (see fig. 5.9). The dissociation begins (see fig. 5.8, n=1) from one of the four equivalent peripheral C atoms closest to the Ir surface top position, which, after the C-H bond cleavage, binds strongly to the surface Ir atoms, approaching its preferred adsorption site, much closer to the surface. The next dissociation step causes a sudden lifting of the molecule with respect to the surface plane (fig. 5.8, n=2), resulting in an almost complete internal strain relief (see fig. 5.9). In fact, three peripheral C atoms are found in equivalently favorable sites, giving therefore three candidates C-H bonds for the next dehydrogenation. However, the lifting of the molecule, which was found to give a 0.67 eV energy gain with respect to the minimum energy flat configuration, implies the breaking of C-H bond closest to the previously dehydrogenated

one. At this point one of the two symmetry axes in the molecule with respect to the substrate is lost, while the other still remains. For the third dehydrogenation (fig. 5.8, *n*=3), keeping in mind that the driving mechanism for dehydrogenation is the proximity of the peripheral C atom to a top site, two equivalent C-H bonds candidates are found, next to to the freshly dehydrogenated peripheral C. The evolution of the system towards one of the equivalent outcomes determines a clear twist of the molecules, in order to better accommodate the newly dehydrogenated C atom in its favored bond site on the substrate. This causes the loss of the second symmetry axis, and fully determine the remaining evolution of the dissociation reaction. From this step on the molecules gradually complete the rotation to the final adsorption geometry, always losing H atoms next to dehydrogenated bonds. During the process the molecules progressively settle down towards a dome shape configuration, always keeping an end lifted till the very end, in order to allow for some strain relief, whilst the internal C-C strain of the part attached to the surface increases. The final dissociation products correspond to dome-shaped Gr nanoflakes, whose interaction with the Ir substrate takes place only at the cluster edges, similarly to what observed for early stage Gr growth on Ir(111) using ethylene [33]. With increasing temperature, the mobility of the nanodomes becomes large enough to permit the formation of larger clusters and eventually graphene.

To test the consistency of our calculations, we simulated the C 1s core level spectra for each of the intermediate species. Figure 5.10 (b) reports a series of simulated spectra together with the experimental one, showing an excellent agreement. Starting from a three component line shape, associated to $C_{24}H_{12}$ and $C_{24}H_{11}$ molecules, the C 1s spectra, above 525 K, changes shape and shifts to lower BE, as observed, for example, for $C_{24}H_{10}$ and $C_{24}H_{7}$, eventually forming the nanodomes around 765 K. At higher temperature the clusters nucleate to form larger islands and the spectral distribution becomes narrower (see simulated spectrum corresponding to the graphene flake formed by 54 C atoms - C_{54}). The single peak at 284.1 eV, fingerprint of graphene formation on Ir(111), appears only at the highest temperature (1080 K).

Even though the dissociation process described above is the most energetically favorable, we also tested other reaction path which did not include molecular lifting and curling processes. For example we considered the possibility for the molecule to remain flat on the surface after upon the second dehydrogenation. However this results in a 0.67 eV higher energy state. Moreover the evolution of the reaction following this new sequence would end up in an un-rotated C_{24} cluster presenting the same azimuthal orientation as the

original coronene molecule, which has a 2.27 eV higher energy. Notably, the reaction path involving the flat dissociation behavior results in a simulated C 1s core level with an additional lower BE component (282.9 eV), which is not experimentally observed.

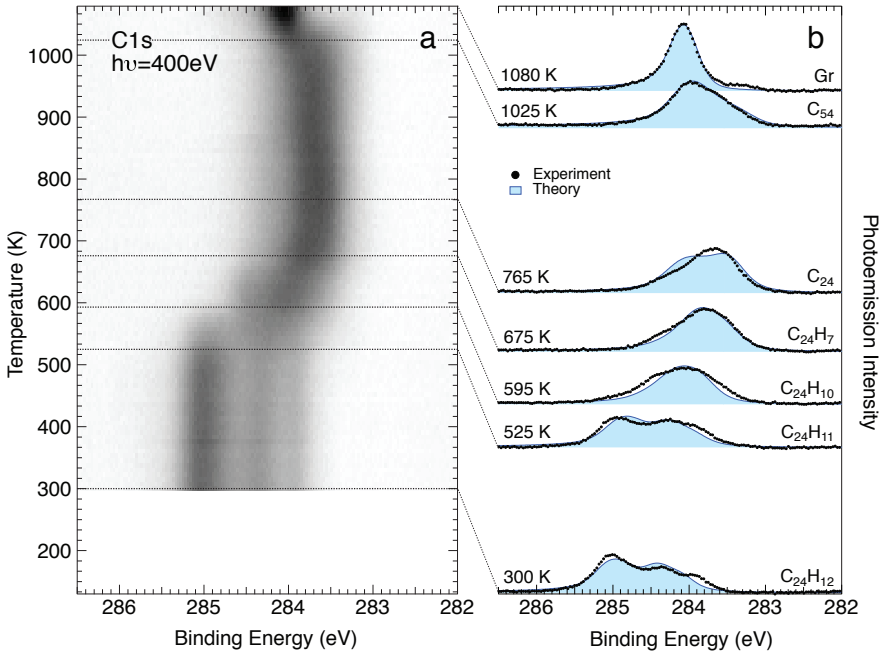

Figure 5.10: (a) 2D plot of the temperature dependent C 1s core level spectra (about 100 spectra). (b) Comparison between experimental (black) and DFT simulated (blue) selected C 1s core-level spectra.

Finally, we elaborated a microkinetic model, assuming that the reaction rate depends on the activation energy of the first dehydrogenation reaction through a first order rate equation, with the energy barrier provided by the NEB calculations. Figure 5.11 shows the experimental $C_{24}H_{12}$ population evolution together with our theoretical model. The experimental curve was deduced from the fast XPS data acquired during annealing (fig. 5.7 (b)), by looking at the highest BE peak, which is typical of just the first reaction intermediate. The temperature behavior is in good agreement with the experimentally observed decrease of the $C_{24}H_{12}$ population when the pre-exponential factor is equal to 10^{10}. This value, which could seem small if compared with the typical value of 10^{13}, is reasonable if we consider that the pre-factors for dissociation reactions are typically $1/10$ to $1/10^5$ of the pre-factors for desorption of the same molecule [34].

It is interesting to compare our results with those obtained for the simplest

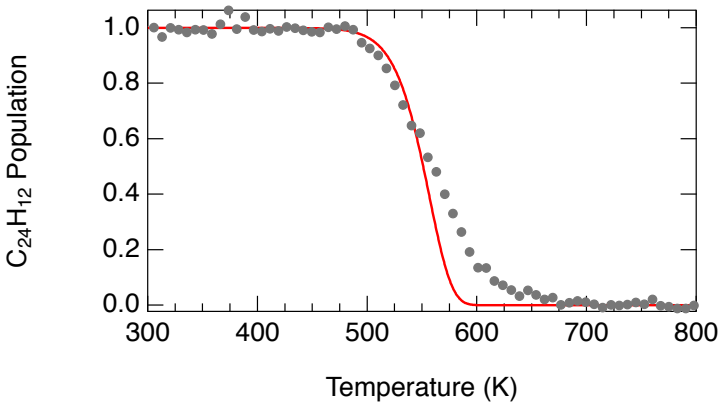

Figure 5.11: (grey dots) Experimentally deduced $C_{24}H_{12}$ population during the annealing ramp and (red curve) theoretical desorption model.

aromatic molecule, *i.e.* benzene (C_6H_6) [35]. Theoretical calculations of benzene adsorption on Cu(100) show that, starting from a flat adsorption configuration, after the first C-H bond cleavage also the phenyl radical C_6H_5 and the ortho-benzyne species C_6H_4 assume upright configurations. It is interesting to observe that instead, the dissociation of benzene on Pt(111), which is a transition metal quite similar to Ir, results in a tilted configuration with the C atoms bonded to a top site [36]. Our results therefore suggest that the process of thermally activated molecular lifting could be a more general behavior in the dissociation process of similar molecules, also for larger PAHs. We suppose that this is the case for other transition metal surfaces, where the presence of unsaturated C bonds could lead to the development of strong interactions between the partially dehydrogenated molecules and the metal substrates. The main driving force resulting in the tilt and rotation of the molecule before curling, *i.e.* the creation of new bonds with the substrate which breaks the molecular symmetries and allows for some internal strain relief, somehow mimics what happens in the case of heterocyclic aromatic adsorbates such as pyridine, pyrrole and thiopene for which, besides flat-lying configurations, also tilted geometries have been reported.

To conclude, we completely characterized the complex dehydrogenation path of coronene on Ir(111) by combining a number of experimental and theoretical techniques. During the process the molecules undergo a series of transformations, including molecular lifting, twisting, and curling, in order to accomodate, at each dissociation step, to the most favorable site on the surface,

and to minimize the internal C-C strain induced on the molecules upon adsorption. In particular, after the second C-H bond cleavage, the molecules tilt with respect to the Ir surface, while, during the next dehydrogenation steps, they rotate their symmetry axis. As the reaction proceeds, the molecules gradually settle down to form peculiar dome-shaped nanographene islands. Higher temperatures promote the surface diffusion of the nano-domes, which result in the formation of larger C islands and eventually, above 1050 K, in single layer Gr, similarly to what reported in literature [33].

The coronene dehydrogenation mechanism could be exploited to create new nanostructures with different functionalities by encapsulating single adatoms below the carbon dome, trough diffusion of the new species underneath the carbon disk just before the molecular crowding. Although this process would require an accurate control on the reaction kinetics, which is a challenging task, we believe that the lifting of the molecule could be an important step in following this strategy. In fact, intercalation of atomic species below nanographene flakes, which could lead to interesting applications in spintronics [37] and energy storage [38], is usually hindered by the strong bonds formed by the peripheral C atoms with the substrate, which prevent atomic species diffusion below the C clusters. Finally, the precise control of the molecular tilt could tailor the chemical reactivity of the system, by activating or inhibiting specific reactions that are usually catalyzed by the substrate surface. A similar behavior was reported, for example, in the case of different carbonyl compounds on Cu(111) and Ag(111) [39, 40].

5.2 Epitaxial growth of hexagonal Boron Nitride monolayer: formation of a single type rotational domain

As outlined in the introduction of the chapter, the electronic and geometrical structure of *h*-BN make it the ideal candidate for integration as a dielectric spacer in Gr-based electronics. However, this requires scalable methods for producing large-area high-quality *h*-BN layers. CVD has proved to be a successful method for producing high quality *h*-BN layers on different TMs by using borazine ($B_3N_3H_6$) as a precursor. Nevertheless, to date, it is challenging to obtain single crystalline domains because of the formation of rotated phases that give rise to grain boundaries and other 1D defects.

This section introduces a CVD method for producing large single crystal *h*-BN layers on Ir(111) by properly controlling the growth conditions. Two different procedures have been adopted to grow *h*-BN on Ir(111). The first method consists of exposing the Ir surface at T=1070 K to $5{\cdot}10^{-8}$ mbar of borazine, up to a total exposure of about 100 L. The second approach, instead, consists of repeated cycles of room temperature borazine adsorption (p=$1{\cdot}10^{-8}$ mbar) up to saturation, followed by annealing to T=1270 K, with a heating rate of 4 K/s. We will refer to the first procedure as *high temperature growth* (HTG), while the second approach will be called *temperature programmed growth* (TPG). Borazine was synthesized following the procedure described by Wideman *et al.* [41] and stored below 250 K at all times to avoid its degradation. Prior to every deposition, borazine was regularly purified by repeated freeze-thaw cycles.

Figure 5.12 shows the LEED patterns acquired for a single layer *h*-BN synthesized with the methods described above. The presence of narrow well defined diffraction spots is a clear indication of the quality and long range structural order of the *h*-BN layers obtained with both procedures. Along with the substrate and first order *h*-BN diffraction spots, we observe the presence of a six-fold arrangement of sharp moiré spots (see also the zoom in the instes) that are due to the formation of a coincidence lattice between *h*-BN and the Ir(111) surface, similarly to what observed for Gr grown on Ir(111). From the analysis of the moiré periodicity we calculate a *h*-BN(13$\times$13)/Ir(12$\times$12) superstructure.

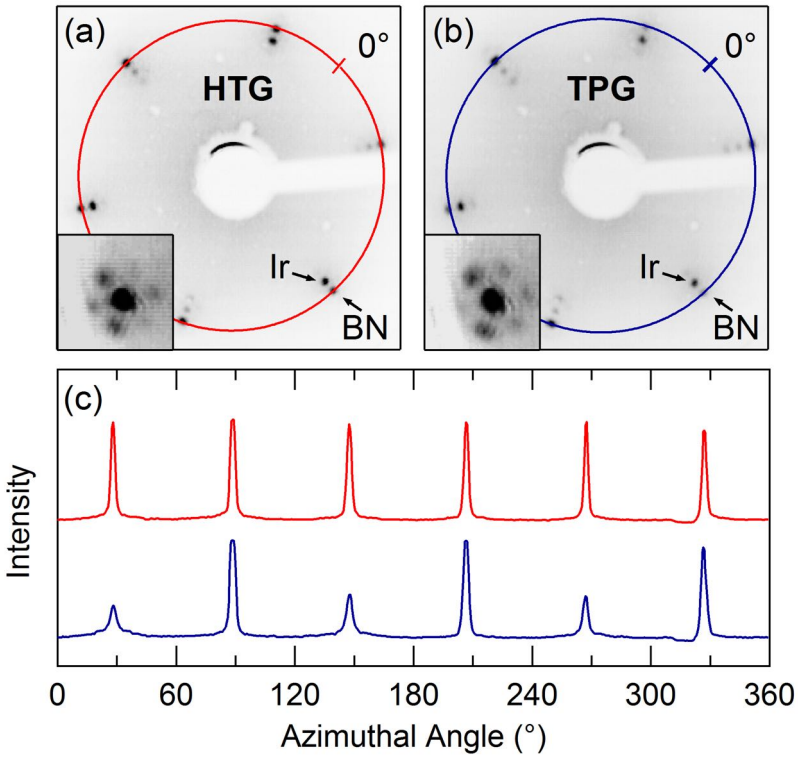

Figure 5.12: LEED patterns measured at 83 eV for h-BN synthesized according to (a) HTG and (b) TPG procedures. Insets: zoom-in of the principal spots measured at 55 eV. (c) Circular lines profiles obtained along the colored rings containing the *h*-BN spots in (a) and (b).

This result, together with the absence of additional diffraction features which would originate from rotated domains, indicates that, for both the synthesis strategies, the *h*-BN unit cell is aligned parallel to one of the main crystallographic directions of the substrate. However, a comparison of the diffraction spots intensities reveals remarkable differences for the two methods. While the substrate diffraction spots always modulate according to the expected almost 3-fold symmetry, meaning that spots 120° apart show the same intensity, while adjacent spots show significantly different intensity due to second layer effects, the first order *h*-BN diffraction spots exhibits either perfect 6-fold or almost 3-fold symmetry depending on the growth method. This is more easily appreciable by looking at the two circular line profiles reported in fig. 5.12 (c), which were calculated by looking at the diffraction intensity along a circular path centered on the (0,0) spot and passing through the first order *h*-BN spots. The red curve indicates that the *h*-BN spots associated to the HTG method do

not show appreciable intensity modulations. On the other hand, the blue curve associated to the TPG method shows a strong 3-fold modulation.

This difference can be explained by looking at the *h*-BN unit cell reported in fig. 5.13. In fact, due to the two non equivalent B and N atoms inside its unit cell, *h*-BN is not invariant under 60° rotation. This implies that two distinct orientations can be found for the same adsorption site, each generating a perfect 3-fold symmetry diffraction pattern, and rotated by 60°. When these phases are equally present on the surface, the superposition of their diffraction patterns give, on average, a 6-fold symmetry. This is the case of the *h*-BN layer obtained from the HTG method. On the other hand, following these observations, we can deduce from the blue line profile in fig. 5.12 that the TPG approach result in *h*-BN which is predominantly oriented along one of the two possible rotational phases.

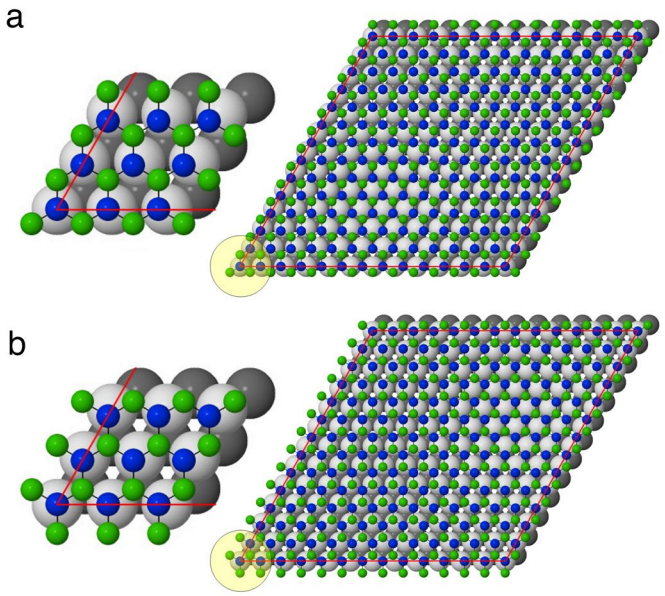

Figure 5.13: Non equivalent possible *h*-BN(13×13)/Ir(12×12) superstructures.

To gain further insight into the structural properties of the *h*-BN/Ir(111) interface, we employed XPS and XPD to characterize the chemical and geometrical configuration of the system. Figure 5.14 shows the HR-XPS B 1s, N 1s, and Ir $4f_{7/2}$ core level spectra after *h*-BN synthesis with the HTG method. The photoemission spectra do not show any significant difference for the two preparation methods. The double peak structure in the B 1s and N 1s core levels are attributed to regions of *h*-BN with a different degree of interaction with the substrate [42, 43, 44, 45]. The main peaks B0 and N0 at 189.84 and 397.52

eV, respectively, are thus associated with *h*-BN regions weakly interacting with the Ir atoms, while the minor contributions B1 and N1 at 190.61 and 398.62 eV, respectively, arise from strongly chemisorbed *h*-BN regions. Also, the Ir $4f_{7/2}$ core level displays three components: IrB and IrS, related to bulk and surface Ir atoms respectively, and a small residual adsorbate-induced component (IrS2) observed upon borazine deposition [43].

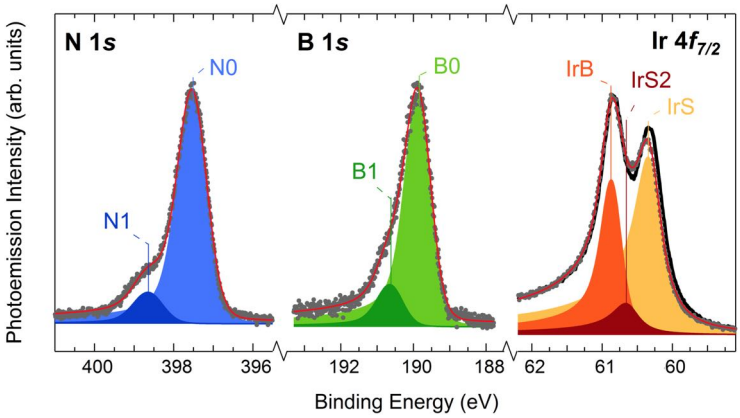

Figure 5.14: High-energy resolution N 1s, B1s, and Ir $4f_{7/2}$ core level spectra measured for *h*-BN grown on Ir(111) with the HTG approach. The fit results (red line) and fit components are shown superimposed. The Ir $4f_{7/2}$ spectrum from the clean surface (black, thick curve) is also shown for comparison.

Figure 5.15 shows the B 1s and N 1s XPD patterns for the two preparations (colored sectors), together with corresponding multiple scattering simulations (grey regions), for two different photoelectron kinetic energies (Ek, 115 and 315 eV). The simulations have been performed with the program package for Electron Diffraction in Atomic Cluster (EDAC).

We will first consider the XPD patterns corresponding to the HTG preparation (fig. 5.15 a,c,e,g). Both B 1s and N1s data exhibits similar diffraction features, with bright intensity maxima close to grazing emission angles. These patterns are 6-fold symmetric, consistently with the presence of two antiparallel *h*-BN domains as suggested by LEED measurements.

In sharp contrast with these findings, the diffraction patterns for *h*-BN obtained with the TPG preparation show a clear 3-fold intensity modulation (fig. 5.15 b,d,f,h), in good agreement with the hypothesis of the prevalence of only one type *h*-BN orientation. A close inspection of the B 1s and N 1s patterns shows that the position of their maxima are 60° apart from each other, due to the non equivalent positions of B and N inside the *h*-BN unit cell.

These results clearly indicate that the synthesis conditions strongly affect the orientation of the h-BN layer. This hypothesis is further supported by the very good agreement with the simulated diffraction pattern. We compared the experimental XPD patterns with simulations corresponding to different percentages of the two rotated domains depicted in fig. 5.13 and computed the respective R-factors. The best agreement was achieved for a 50±5% composition for the HTG growth and for a nearly 100% composition of structure (a) in fig. 5.13 for the TPG growth.

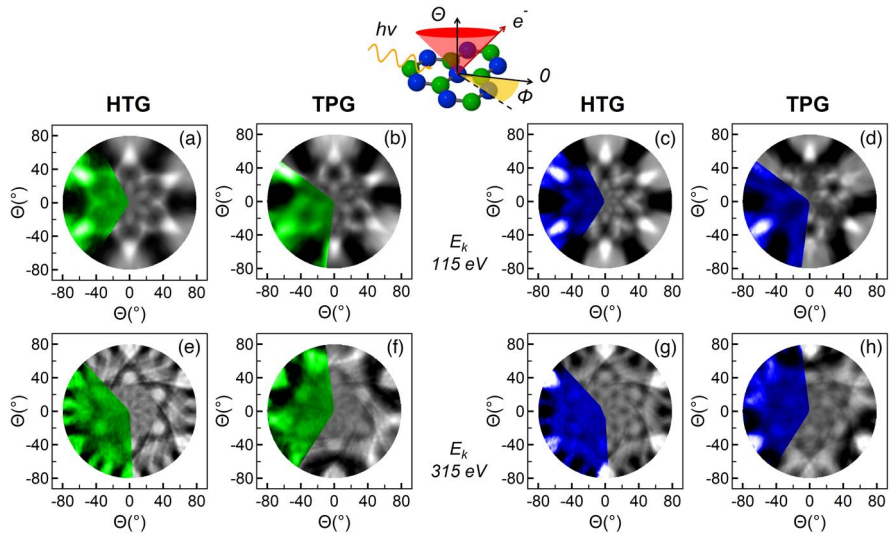

Figure 5.15: Experimental (colored) and simulated (grey) XPD difraction pattern for (a-d) the B 1s and (e-h) the N 1s core levels measured at the indicated photoelectron kinetic energies.

To measure the average domain size of the singly oriented *h*-BN layer obtained with the TPG approach, we performed SPA-LEED high resolution *k*-space measurements of the diffraction spots. Figure 5.16 (a-d) shows the high resolution two-dimensional SPA-LEED diffraction maps at two different kinetic energies. The sharp diffraction spots, as well as the presence of multiple scattering moiré spots, are a clear indication of the quality of the layer. Moreover, a strong 3-fold intensity modulation can be appreciated at both energies. Figure 5.16 (e) shows the spot profile along the [10] direction which was used to obtained qunatitative informations on the mean domain size of the *h*-BN layer. The inset shows a detail on the (1,0) *h*-BN spot together with the best fit analysis obtained using a Voigt function. The Lorentzian FWHM is below 0.008 $Å^{-1}$, corresponding to an average domain size larger than 900 Å, which is compa-

rable to the expected width of the Ir sample terraces.

The coexistence of multiple *h*-BN domains has been reported on several metal surfaces. For example, domains without preferential orientation develop on weakly interacting substrates such as Pd [17], Cu [18], and Ag [19]. On the other hand, for the strongly interacting *h*-BN/Rh(111) system, the *h*-BN domains were observed to grow with the same orientation as that of the substrate, although 180° misoriented islands have been observed [21]. Previous experimental findings [42] and theoretical predictions [46] suggest that the chemical interaction of *h*-BN on Ir(111) is slightly weaker compared to that on Rh(111), where the monolayer is strongly chemisorbed. For the commensurate *h*-BN/Ni(111) interface, the formation of two antiparallel domains has been reported, corresponding to a unit cell with N on top of nickel and B on fcc or hcp sites [20, 47]. It has been suggested that small amounts of carbon contamination may control the ratio between these domains [20]. The absence of carbon or other impurities was carefully checked by XPS (detection limit of 1% of a monolayer), thus we can safely rule out this possibility.

So, why is it possible to obtain large singly oriented *h*-BN domains with the TPG method? One possible scenario is that small h-BN patches with well-defined alignment are already established at the first stages of the growth, and that these seeds expand while keeping their initial orientation. Theoretical calculations showed that, for the commensurate h-BN/Ni(111) interface, the bonding configurations are (N_{top},B_{hcp}) and (N_{top},B_{fcc}), the latter being energetically favored [48]. The situation is only slightly different for lattice-mismatched interfaces, where periodic repetitions of different coordination sites give rise to a moiré pattern. Nonetheless, the (N_{top},B_{fcc}) configuration is predicted to be stable also for these systems, meaning that the regions where the *h*-BN sheet is closer to the substrate develop around this configuration [21, 49]. Theoretical calculations based on local-density approximation, where a 1×1 commensurate geometry has been applied, predict a weaker strength of the binding energy of *h*-BN on Ni compared to that on Ru(0001) whose bonding, instead, is comparable to that of Rh(111) and Ir(111) [46]. Moreover, the difference between the binding energy of *h*-BN/Ni(111) and *h*-BN/Ru(0001) is even larger when taking into account the lattice mismatch of the latter interface [50]. Accordingly, it is plausible to assume the (N_{top},B_{fcc}) (fig. 5.13 (a)) to be a bonding configuration also for the initial stages of h-BN growth on the Ir(111) surface.

On the basis of these considerations, we can theorize the following mechanism for *h*-BN growth on Ir with the TPG approach. When the surface is exposed to borazine at room temperature and then annealed, the nucleation

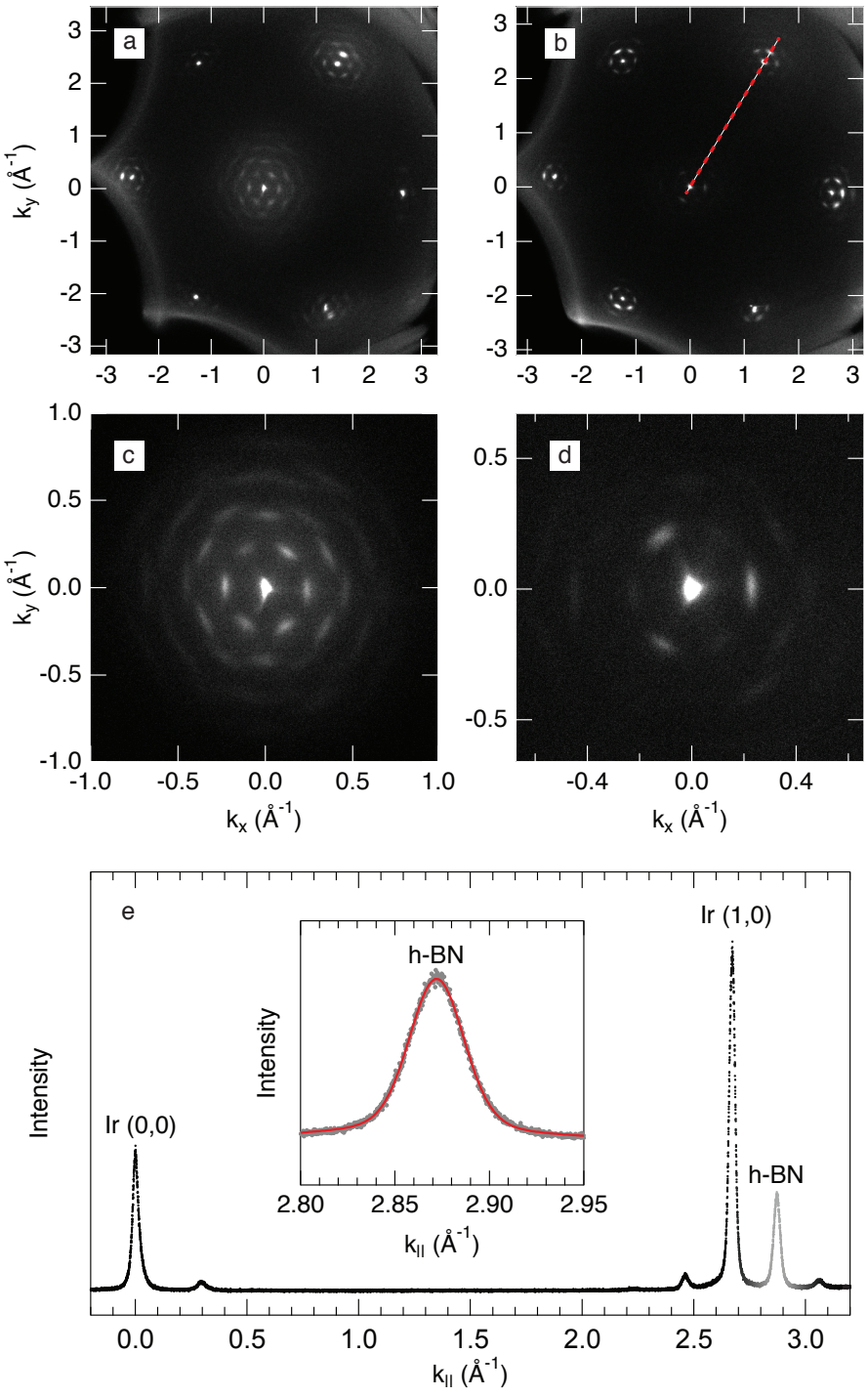

Figure 5.16: (a,b) First Brillouin Zone high resolution SPA-LEED diffraction map acquired for TPH *h*-BN on Ir(111) at 71 an 84 eV respectively. (c,d) Zoom in near the (0,0) spot of the previous images. (e) Spot profile analysis along the [10] direction (red dashed line in (b)) acquired at 84 eV. The inset displays the best fit analysis of the (1,0) *h*-BN diffraction spot.

starts in the lowest energy configuration: the small BN islands adopt a single orientation relative to the substrate, which very likely corresponds to a fcc domain. As the growth proceeds, the fcc nucleation seeds expand forming larger BN clusters which keep the initial orientation. This can be explained as due to the energy difference between the fcc and hcp configurations, in analogy to the growth of *h*-BN on Ru(0001) [50]. As the width of the BN nucleation seeds increases, the energy difference between fcc and hcp gets higher, thus allowing the growth of a single domain with the same configuration of the initial seeds. For the synthesis performed directly at high temperature, on the other hand, the thermal energy is sufficient to exceed the energy difference between the fcc and hcp adsorption configuration of the BN seeds during the initial stages of the CVD process. As a result, both nucleation seeds form, and two antiparallel h-BN domains develop. Interestingly, the STM measurements on the *h*-BN/Ru(0001) nanomesh [50] show a parallel alignment of growing islands within the same Ru terrace when the growth is performed at 700 K, while both domains appear when borazine is dosed above 950 K.

To conclude, we proved that, by using proper synthesis conditions, *h*-BN monolayer with a single orientation can be grown on Ir(111). We employed two different CVD growth methods using borazine as a precursor: (i) high temperature dose at 1070 K, and (ii) cyclic deposition at room temperature followed by annealing to 1270 K. While the first method resulted in 180° misoriented *h*-BN domains, the second preparation results in *h*-BN domains predominantly oriented along one of the two possible configurations. This behavior is related to a different interplay between the thermal energy and the binding energy difference between the two phases during the first stages of h-BN growth. This approach could be further exploited on other transition metal surfaces in order to control the orientation of the resulting h-BN films.

Bibliography

[1] M. Y. Han, B. Özyilmaz, Y. Zhang, and Ph. Kim. Energy band-gap engineering of graphene nanoribbons. *Physical Review Letters*, **98**(20):206805, 2007.

[2] L. Yang, C. H. Park, Y. W. Son, M. L. Cohen, and S. G. Louie. Quasiparticle energies and band gaps in graphene nanoribbons. *Physical Review Letters*, **99**(18):186801, 2007.

[3] Y. W. Son, M. L. Cohen, and S. G. Louie. Energy gaps in graphene nanoribbons. *Physical Review Letters*, **97**(21):216803, 2006.

[4] J. Cai, P. Ruffieux, R. Jaafar, M. Bieri, T. Braun, S. Blankenburg, M. Muoth, A. P. Seitsonen, M. Saleh, X. Feng, K. Müllen, and R. Fasel. Atomically precise bottom-up fabrication of graphene nanoribbons. *Nature*, **466**(7305):470–473, 2010.

[5] M. Treier, C. A. Pignedoli, T. Laino, R. Rieger, K. Müllen, D. Passerone, and R. Fasel. Surface-assisted cyclodehydrogenation provides a synthetic route towards easily processable and chemically tailored nanographenes. *Nature Chemistry*, **3**(1):61–67, 2011.

[6] S. Blankenburg, J. Cai, P. Ruffieux, R. Jaafar, D. Passerone, X. Feng, K. Müllen, R. Fasel, and C. A. Pignedoli. Intraribbon heterojunction formation in ultranarrow graphene nanoribbons. *ACS Nano*, **6**(3):2020–2025, 2012.

[7] P. Ruffieux, J. Cai, N. C Plumb, L. Patthey, D. Prezzi, A. Ferretti, E. Molinari, X. Feng, K. Müllen, C. A Pignedoli, and R. Fasel. Electronic structure of atomically precise graphene nanoribbons. *ACS Nano*, **6**(8):6930–6935, 2012.

[8] L. Talirz, H. Söde, J. Cai, P. Ruffieux, S. Blankenburg, R. Jafaar, R. Berger, X. Feng, K. Müllen, D. Passerone, R. Fasel, and C. A. Pignedoli. Termini of bottom-up fabricated graphene nanoribbons. *Journal of the American Chemical Society*, **135**(6):2060–2063, 2013.

[9] E. Fortin and W. M. Sears. Photovoltaic effect and optical absorption in MoS_2. *Journal of Physics and Chemistry of Solids*, **43**(9):881–884, 1982.

[10] K. Dolui, C. D. Pemmaraju, and S. Sanvito. Electric field effects on armchair MoS_2 nanoribbons. *ACS Nano*, **6**(6):4823–4834, 2012.

[11] K. Watanabe, T. Taniguchi, and H. Kanda. Direct-bandgap properties and evidence for ultraviolet lasing of hexagonal boron nitride single crystal. *Nature Materials*, **3**(6):404–409, 2004.

[12] M. Corso, W. Auwärter, M. Muntwiler, A. Tamai, T. Greber, and J. Osterwalder. Boron nitride nanomesh. *Science*, **303**(5655):217–220, 2004.

[13] A. K. Geim and I. V. Grigorieva. Van der Waals heterostructures. *Nature*, **499**(7459):419–425, 2013.

[14] K. K. Kim, A. Hsu, X. Jia, S. M. Kim, Y. Shi, M. Hofmann, D. Nezich, J. F. Rodriguez-Nieva, M. Dresselhaus, T. Palacios, and J. Kong. Synthesis of monolayer hexagonal boron nitride on Cu foil using chemical vapor deposition. *Nano Letters*, **12**(1):161–166, 2011.

[15] C. R. Dean, A. F. Young, I. Meric, C. Lee, L. Wang, S. Sorgenfrei, K. Watanabe, T. Taniguchi, P. Kim, K. L. Shepard, and J. Hone. Boron nitride substrates for high-quality graphene electronics. *Nature Nanotechnology*, **5**(10):722–726, 2010.

[16] A. L. Gibb, N. Alem, J. H. Chen, K. J. Erickson, J. Ciston, A. Gautam, M. Linck, and A. Zettl. Atomic resolution imaging of grain boundary defects in monolayer chemical vapor deposition-grown hexagonal boron nitride. *Journal of the American Chemical Society*, **135**(18):6758–6761, 2013.

[17] M. Morscher, M. Corso, T. Greber, and J. Osterwalder. Formation of single layer h-BN on Pd(111). *Surface Science*, **600**(16):3280–3284, 2006.

[18] S. Joshi, D. Ecija, R. Koitz, M. Iannuzzi, A. P. Seitsonen, J. Hutter, H. Sachdev, S. Vijayaraghavan, F. Bischoff, K. Seufert, J. V. Barth, and W. Auwärter. Boron nitride on Cu(111): an electronically corrugated monolayer. *Nano Letters*, **12**(11):5821–5828, 2012.

[19] F. Müller, S. Hüfner, H. Sachdev, R. Laskowski, P. Blaha, and K. Schwarz. Epitaxial growth of hexagonal boron nitride on Ag(111). *Physical Review B*, **82**(11):113406, 2010.

[20] W. Auwärter, M. Muntwiler, J. Osterwalder, and T. Greber. Defect lines and two-domain structure of hexagonal boron nitride films on Ni(111). *Surface Science*, **545**(1):L735–L740, 2003.

[21] G. Dong, E. B. Fourré, F. C. Tabak, and J. W. M. Frenken. How boron nitride forms a regular nanomesh on Rh(111). *Physical Review Letters*, **104**(9):096102, 2010.

[22] G. Fronzoni, O. Baseggio, M. Stener, W. Hua, G. Tian, Y. Luo, B. Apicella, M. Alfé, M. de Simone, A. Kivimäki, and M. Coreno. Vibrationally resolved high-resolution NEXAFS and XPS spectra of phenanthrene and coronene. *The Journal of Chemical Physics*, **141**(4):044313, 2014.

[23] R. Boschi, E. Clar, and W. Schmidt. Photoelectron spectra of polynuclear aromatics. III. The effect of nonplanarity in sterically overcrowded aromatic hydrocarbons. *The Journal of Chemical Physics*, **60**(11):4406–4418, 1974.

[24] P. G. Schroeder, C. B. France, B. A. Parkinson, and R. Schlaf. Orbital alignment at p-sexiphenyl and coronene/layered materials interfaces measured with photoemission spectroscopy. *Journal of Applied Physics*, **91**(11):9095–9107, 2002.

[25] K. Medjanik, D. Kutnyakhov, S. A. Nepijko, G. Schönhense, S. Naghavi, V. Alijani, C. Felser, N. Koch, R. Rieger, M. Baumgarten, and K. Mullen. Electronic structure of large disc-type donors and acceptors. *Physical Chemistry Chemical Physics*, **12**(26):7184–7193, 2010.

[26] Y. T. Wu and J. S. Siegel. Aromatic molecular-bowl hydrocarbons: synthetic derivatives, their structures, and physical properties. *Chemical Reviews*, **106**(12):4843–4867, 2006.

[27] V. M. Tsefrikas and L. T. Scott. Geodesic polyarenes by flash vacuum pyrolysis. *Chemical Reviews*, **106**(12):4868–4884, 2006.

[28] C. J. Hagedorn, M. J. Weiss, and W. H. Weinberg. Dissociative chemisorption of hydrogen on Ir(111): Evidence for terminal site adsorption. *Physical Review B*, **60**(20):R14016, 1999.

[29] K. Moritani, M. Okada, M. Nakamura, T. Kasai, and Y. Murata. Hydrogen-exchange reactions via hot hydrogen atoms produced in the dissociation process of molecular hydrogen on Ir $\{111\}$. *The Journal of Chemical Physics*, **115**(21):9947–9959, 2001.

[30] C. Busse, P. Lazić, R. Djemour, J. Coraux, T. Gerber, N. Atodiresei, V. Caciuc, R. Brako, A. T. N'Diaye, S. Blügel, J. Zegenhagen, and T. Michely. Graphene on Ir(111): physisorption with chemical modulation. *Physical Review Letters*, **107**(3):036101, 2011.

[31] I. Pletikosić, M. Kralj, P. Pervan, R. Brako, J. Coraux, A. T. N'Diaye, C. Busse, and T. Michely. Dirac cones and minigaps for graphene on Ir(111). *Physical Review Letters*, **102**(5):056808, 2009.

[32] G. Henkelman, B. P. Uberuaga, and H. Jónsson. A climbing image nudged elastic band method for finding saddle points and minimum energy paths. *The Journal of Chemical Physics*, **113**(22):9901–9904, 2000.

[33] P. Lacovig, M. Pozzo, D. Alfé, P. Vilmercati, A. Baraldi, and S. Lizzit. Growth of dome-shaped carbon nanoislands on Ir(111): the intermediate between carbidic clusters and quasi-free-standing graphene. *Physical Review Letters*, **103**(16):166101, 2009.

[34] C. T. Campbell, L. Árnadóttir, and J. R. V. Sellers. Kinetic prefactors of reactions on solid surfaces. *Zeitschrift für Physikalische Chemie*, **227**(9-11):1435–1454, 2013.

[35] H. Lesnard, M. L. Bocquet, and N. Lorente. Dehydrogenation of aromatic molecules under a scanning tunneling microscope: pathways and inelastic spectroscopy simulations. *Journal of the American Chemical Society*, **129**(14):4298–4305, 2007.

[36] W. Gao, W. T. Zheng, and Q. Jiang. Dehydrogenation of benzene on Pt(111) surface. *The Journal of Chemical Physics*, **129**(16):164705, 2008.

[37] M. Sicot, P. Leicht, A. Zusan, S. Bouvron, O. Zander, M. Weser, Y. S. Dedkov, K. Horn, and M. Fonin. Size-selected epitaxial nanoislands underneath graphene moiré on Rh(111). *ACS Nano*, **6**(1):151–158, 2012.

[38] F. Xu, Z. Tang, S. Huang, L. Chen, Y. Liang, W. Mai, H. Zhong, R. Fu, and D. Wu. Facile synthesis of ultrahigh-surface-area hollow carbon nanospheres for enhanced adsorption and energy storage. *Nature Communications*, **6**, 2015.

[39] M. E. Chiu, D. J. Watson, G. Kyriakou, M. S. Tikhov, and R. M. Lambert. Tilt the Molecule and Change the Chemistry: Mechanism of S-Promoted Chemoselective Catalytic Hydrogenation of Crotonaldehyde on Cu(111). *Angewandte Chemie*, **118**(45):7692–7696, 2006.

[40] K. Brandt, M. E. Chiu, D. J. Watson, M. S. Tikhov, and R. M. Lambert. Chemoselective catalytic hydrogenation of acrolein on Ag(111): Effect of molecular orientation on reaction selectivity. *Journal of the American Chemical Society*, **131**(47):17286–17290, 2009.

[41] T. Wideman and L. G. Sneddon. Convenient procedures for the laboratory preparation of borazine. *Inorganic Chemistry*, **34**(4):1002–1003, 1995.

[42] A. B. Preobrajenski, M. A. Nesterov, M. L. Ng, A. S. Vinogradov, and N. Mårtensson. Monolayer h-BN on lattice-mismatched metal surfaces: On the formation of the nanomesh. *Chemical Physics Letters*, **446**(1):119–123, 2007.

[43] F. Orlando, R. Larciprete, P. Lacovig, I. Boscarato, A. Baraldi, and S. Lizzit. Epitaxial growth of hexagonal boron nitride on Ir(111). *The Journal of Physical Chemistry C*, **116**(1):157–164, 2011.

[44] F. Schulz, R. Drost, S. K. Hämäläinen, T. Demonchaux, A. P. Seitsonen, and P. Liljeroth. Epitaxial hexagonal boron nitride on Ir(111): A work function template. *Physical Review B*, **89**(23):235429, 2014.

[45] F. Orlando, P. Lacovig, L. Omiciuolo, N. G. Apostol, R. Larciprete, A. Baraldi, and S. Lizzit. Epitaxial Growth of a Single-Domain Hexagonal Boron Nitride Monolayer. *ACS Nano*, **8**(12):12063–12070, 2014.

[46] R. Laskowski, P. Blaha, and K. Schwarz. Bonding of hexagonal BN to transition metal surfaces: an ab initio density-functional theory study. *Physical Review B*, **78**(4):045409, 2008.

[47] M. Muntwiler, W. Auwärter, F. Baumberger, M. Hoesch, T. Greber, and J. Osterwalder. Determining adsorbate structures from substrate emission X-ray photoelectron diffraction. *Surface Science*, **472**(1):125–132, 2001.

[48] G. B. Grad, P. Blaha, K. Schwarz, W. Auwärter, and T. Greber. Density functional theory investigation of the geometric and spintronic structure of h-BN/Ni(111) in view of photoemission and STM experiments. *Physical Review B*, **68**(8):085404, 2003.

[49] R. Laskowski and P. Blaha. Ab initio study of h- BN nanomeshes on Ru(001), Rh(111), and Pt(111). *Physical Review B*, **81**(7):075418, 2010.

[50] J. Lu, P. S. E. Yeo, Y. Zheng, H. Xu, C. K. Gan, M B. Sullivan, A. H. Castro Neto, and K. P. Loh. Step flow versus mosaic film growth in hexagonal boron nitride. *Journal of the American Chemical Society*, **135**(6):2368–2373, 2013.

6 Set up of a mass selected cluster source

A key target in nanocluster science is the controllable and reproducible synthesis of supported nanoparticles with a precise control over their size. Only in this way, in fact, it is possible to investigate their structural, physical, and chemical properties, which are known to be dramatically size-dependent [1, 2, 3, 4]. This is particularly true when using non local experimental probes. For instance, synchrotron based photoelectron spectroscopies offer a unique possibility for investigating the electronic fine structure and the chemical reactivity of nanoclusters, but lack the spatial resolution needed to detect clusters formed by only few atoms, thus providing only space averaged informations. Another limitation related to the use of non size-selective synthesis methods, is the impossibility to simultaneously probe the cluster properties as a function of the particle size and of their adsorption environment. On the other hand, if all the nanoparticles are formed by an equal number of atoms, they will most likely assume the same local configuration, perhaps exhibiting collective behaviors and uniform response to external simulations, with possible applications in catalysis and different fields of modern technology [5, 6].

For these reasons, in the last decades several new techniques have been introduced and refined for the production of mass selected nanoclusters. One example is provided by laser vaporization cluster sources, which were specifically designed for the production of nanoparticles with a well defined number of atoms and their soft-landing on the desired substrate. The original design of such machines owes to the group of Smalley [7] and Maruyama [8], although a fundamental contribution to their development was given by the group of Ulrich Heiz and coworkers [9, 10]. These sources make use of a powerful laser to ablate a high purity target and create charged nanoparticles which are then selected on the basis of their charge to mass ratio. The nanoparticle can be either characterized in gas phase or deposited on any suitable substrate in soft landing conditions, by applying a proper retarding potential. Due to their flexibility and reliability, these machines have already been used in a number of cluster

deposition experiments on TMs and TM oxides substrate [11, 12, 13, 14].

During my PhD, besides the research activity I was also involved in the design and set-up of a cluster source of this kind that is currently under development at the Surface Science Laboratory at Elettra. The design of this source in based on the scheme developed by Heiz and coworkers [9, 10] and currently implemented in most cluster sources at the Department of Physical Chemistry of the Technical University of Munich (Technische Universität München (TUM), Germany). Once operational, this machine will provide an unprecedented opportunity for surface science studies of nanoclusters in combination with state of the art synchrotron radiation based techniques, opening new opportunities to understand and exploit the peculiar quantum size effects of such nanoscale materials.

6.1 The mass selected cluster source at the Surface Science Laboratory

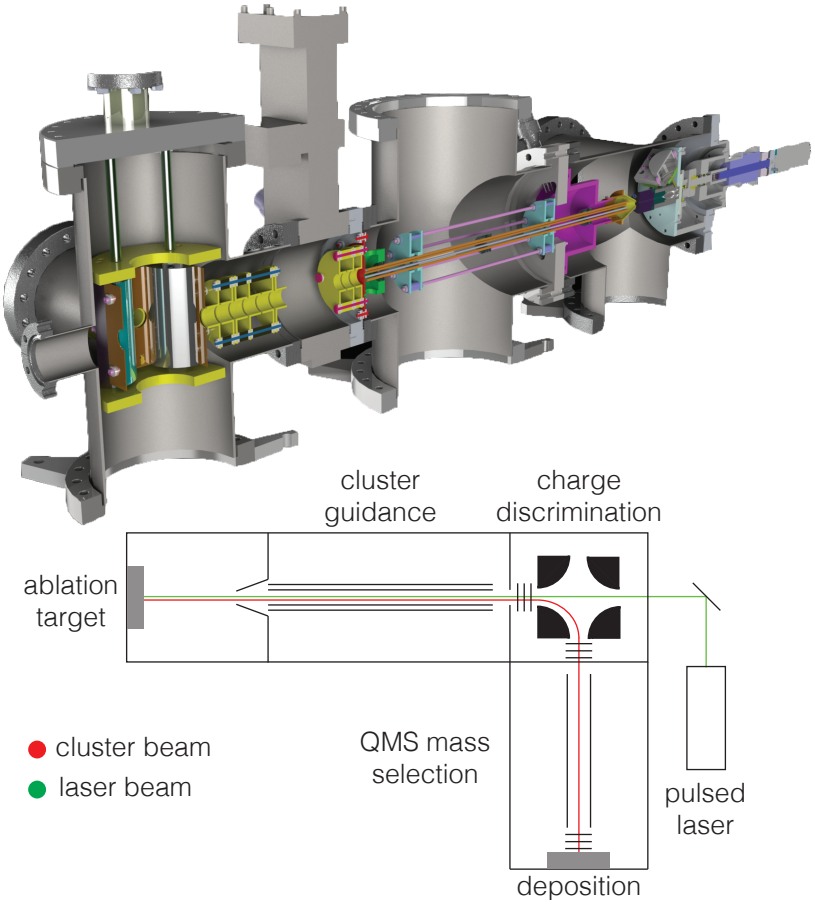

Figure 6.1: (top) Schematic overview of the experimental design of the mass selected cluster source currently under construction at the Surface Science Laboratory, and (bottom) diagram of operation of the mass selected cluster source.

A number of different cluster sources have been developed for the UHV synthesis of nanoparticles, each with specific attributes and suitable for different applications. High melting point metals clusters, for example, are typically synthesized through vaporization or sputtering techniques. On the other hand, if solvated precursors are available, clusters can be transferred and deposited in vacuum by means of electrospray ionization [15]. A solution of the cluster precursors flows through a small biased capillary and is electrosprayed through a buffer gas that undergoes supersonic beam expansion into the vacuum cham-

ber. Electrospray ionization is a cheap and reliable solution, capable of producing a large flux of clusters, however it is limited to those clusters for which stable precursors solutions can be obtained and electrosprayed. Another widely used technique for cluster formation consists of using magnetron sputtering to create a plasma that ejects atoms from a target into a rare gas, where clusterization occurs [16]. The drawback of this approach is that it presents difficulties when dealing with ferromagnetic materials.

The cluster source that we are currently developing at the Surface Science Laboratory is based on laser-induced ablation from a solid target [9, 17]. Laser vaporization is, in fact, a highly flexible and reliable method for the production of clusters of a variety of different materials that could not be thermally evaporated. Laser pulses are used to create a plasma at the point of contact with the target. Subsequently, a carrier gas is used to transport the charged particles into the vacuum system and promoting cluster formation. Fig. 6.1 shows a schematics of our experimental setup. The machine can be schematically divided in the following sections, according to their task: (1) the source chamber where cluster are generated, (2) the transport chamber where clusters are collimated and transported via a RF octupole, (3) the bender chamber where neutral, positive, and negative clusters are electrostatically separated, (4) the quadrupole mass spectrometer chamber where mass discrimination takes place, (5) the deposition and analysis chamber where clusters are deposited on the desired substrate and probed, and (6) the ablation laser. The following sections will introduce in details the whole machine.

6.1.1 Cluster generation

Target ablation is achieved using the second harmonic pulses (532 nm) of a high power Nd:YAG laser (7 ns pulse width, 120Hz repetition rate, and 140 mJ pulse energy, see fig. 6.2). The laser beam enters the setup from a small window in the bender chamber, and is focussed on a small spot (less than 1 mm) on the target in the first chamber, meaning that the laser and cluster beams travels inside the machine in the same path, but in opposite direction. The ablation target, a 40 mm diameter disk, is integrated in a motor-driven hypocycloidal gear assembly (see fig. 6.3) that consists of an inner gear, to which the sample is glued on, which rotates eccentrically inside an outer gear screwed on a stainless steel disk, which also serves as a ground plate. In this way, the laser pulses draw a hypocycloid on the target surface (as visible from fig. 6.3), which covers more than 90% of the target area. This solutions extends the sample lifetime and ensures a better time stability of the cluster

current. The sample holder is pressed against the ground plate by a spring mechanism, with a sealing teflon ring in between.

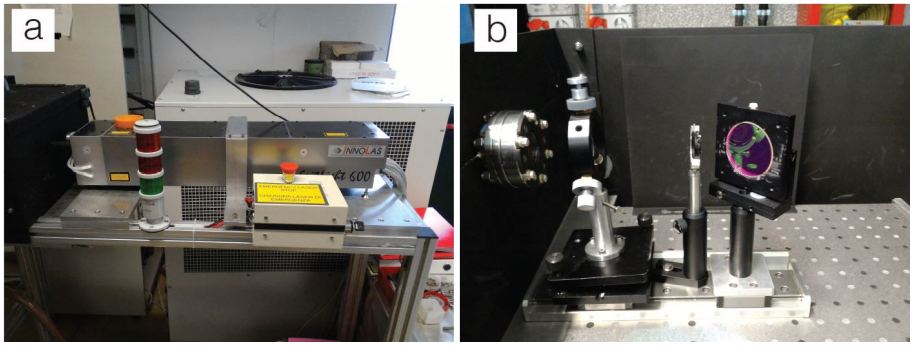

Figure 6.2: (a) The high power Innolas pulsed laser which is used for target ablation in the cluster source. (b) View of the optics used to deflect and focus the laser beam inside the vacuum chaber.

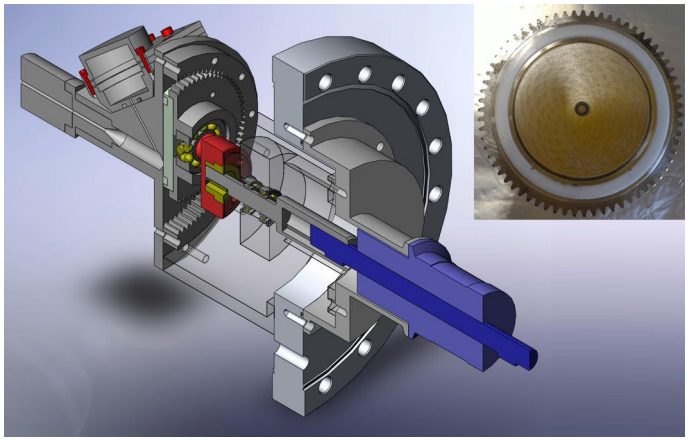

Figure 6.3: Schematic cross section of the hypocycloidal gear assembly used to move the sample during ablation. The stepper motor is visible in the right part of the image, while the system of the two eccentric gears is visible on the left. The inset shows the burning pattern caused by laser ablation on the target. The inner gear is visible glued to the sample.

The interaction of the laser beam with the target generates a hot ion plasma that expands into an expansion chamber (fig. 6.4). During the process, the atoms collides with each other forming high energy larger aggregates that are subsequently stabilized and cooled down upon collision with the molecules or atoms of the buffer gas. For this reason, a high pressure (3 to 10 bar) He jet is released into the expansion chamber, regulated by a pulsed piezoelectric valve

that is triggered by the laser. The pulsed vale (see fig. 6.5) is actuated by a piezoelectric ceramic disk, glued to a stainless steel one. When a high voltage pulse, of the order of 400 V, is applied to one of its sides, the piezo disk shrinks, causing the metal disk, which is bonded on the boundaries, to bend upwards. The bending of the metal disk induces a linear movement on a small piston, which acts like a needle valve on a small aperture between the valve and the expansion camber. A viton gasket is used to seal the valve when the metal disk relaxes to its rest position, and the piston is therefore pressed against the valve aperture. Gas pressure, as well as the voltage and width of the pulse applied to the valve and the delay between the trigger laser pulse, and the gas jet govern both the cluster current and the cluster mass distribution, and must be therefore tuned before each deposition, in order to maximize the cluster current at the desired mass.

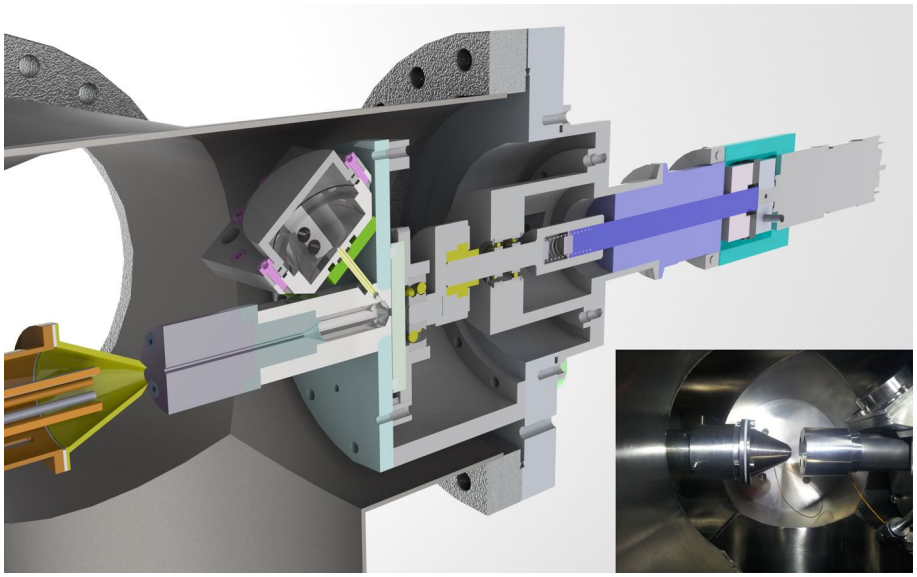

Figure 6.4: Schematic cross section of the first stage of the mass selected cluster source, corresponding to the source chamber where the clusters are formed by laser ablation and undergo adiabatic supersonic beam expansion. The pulsed piezoelectric valve and the expansion chamber are visible, as well as the nozzle separating the latter from the first stage. (inset) Photo of the actual first stage of the mass selected cluster source at the Surface Science Laboratory.

The expansion chamber is separated from the first chamber by means of a narrow cylindrical nozzle (2 mm diameter, see fig. 6.4). The small dimension of the nozzle aperture, combined with the high pressure gradient between the

expansion chamber (3 to 10 bar) and the first chamber (< 0.1 mbar) [1] causes the supersonic jet expansion of the He jets transporting the clusters. Adiabatic expansion through the nozzle cools down the ion plasma and promotes larger cluster formation by addition of new atoms to the seed cluster formed in the expansion chamber, while the excess of condensation energy is absorbed by the buffer gas atoms.

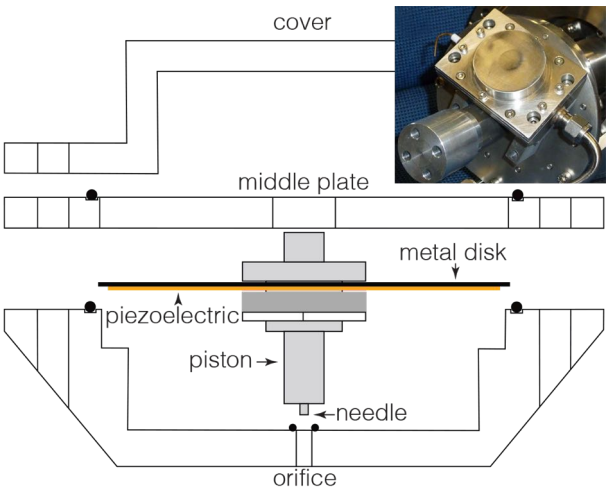

Figure 6.5: Schematic exploded cross section of the piezoelectric pulsed valve. The main components are labelled. (inset) Photo of the piezoelectric pulsed valved built for the cluster source at the Surface Science Laboratory.

To skim the expanding beam and collect only the collimated portion of it, characterized by a narrow kinetic energy distribution, a skimmer is positioned at a distance of about 20 mm from the nozzle. In our setup, the skimmer consists of a stainless steel cone terminating in a tiny orifice (5mm in diameter). The skimmer is fixed to a cylindrical support through three little screws (see fig. 6.6) that can slide on anther support directly attached to the wall of the second chamber, in order to allow adjustments to the skimmer to nozzle distance. A teflon ring is used to seal, and electrically insulate, the skimmer from the outer support, while a viton gasket allows sealing between the sliding cylinders.

6.1.2 Cluster guidance

To guide the cluster beam through the vacuum system we employ a set of different ion optics, which focus it and reduce possible current losses caused by collisions with the chamber walls. Two kinds of ion optics are used in our

[1] Details about the differential pumping system are provided in section 6.1.4.

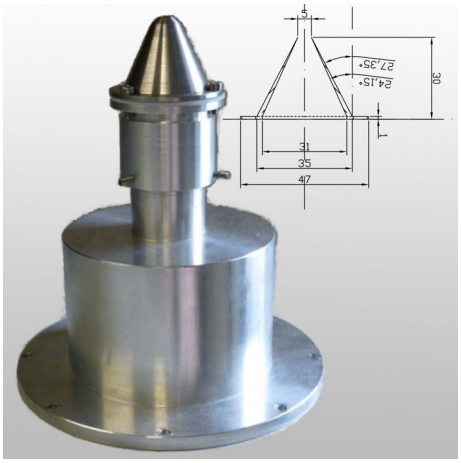

Figure 6.6: Photo and drawing of the skimmer which collect the collimated clusters in the first stage.

chamber: radio frequency octupoles and electrostatic lenses. The following section provide a brief overview of the cluster guides used in our chamber.

As reported in fig. 6.7, immediately after the skimmer orifice the cluster beam is collected by a radio frequency (RF) octupole, consisting of eight stainless steel rods of the same diameter which are mounted in an equidistant circular arrangement. Following the desing of Heiz group, the octupole ion guide is driven by a superimposed DC and RF voltage. In order to increase the RF voltage and superimpose the independent DC voltage, both potentials are applied to the octupole bars via a homemade LC resonator circuit, which basically consists of a transformer coil around a magnetic ferrite and a series of inductances and capacitors (see [10]). The resonance frequency of the coupled octupole-resonator system, given by

$$f_0 = \frac{1}{2\pi\sqrt{LC}} \tag{6.1}$$

where L and C represent the total inductance and capacity respectively, must be properly tuned to match the applied RF, in order to minimize power reflection that quickly damage the transformer. At the moment, the resonance frequency is set around 20 MHz.

To a first approximation, if the octupole diameter is much smaller than its length, the device can be modelled as eight infinitely long rods. Following this approximation, and for sufficiently high RF, the electric potential inside an octupole ion guide can be approximated by an effective potential (pseudopoten-

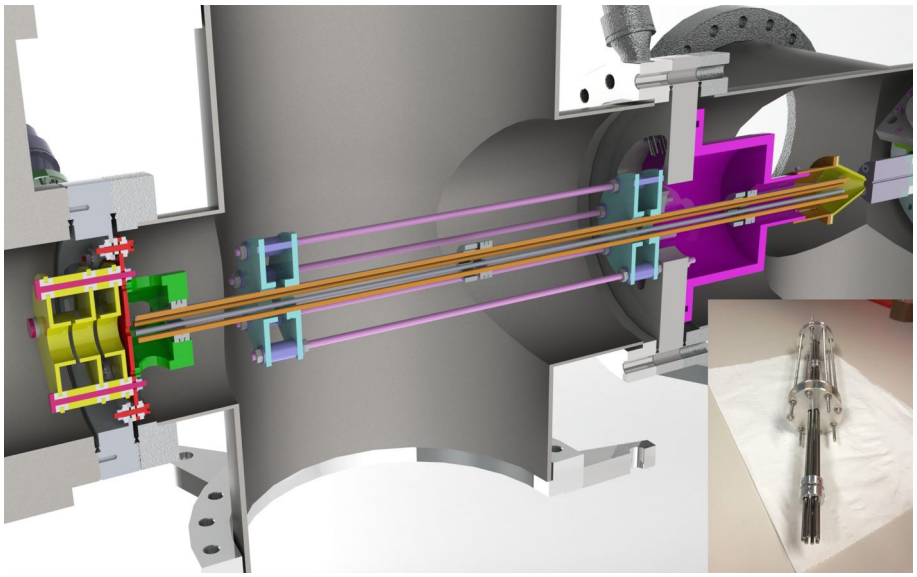

Figure 6.7: Schematic cross section of the second stage and (inset) photo of the octupole developed at the Surface Science Laboratory for the cluster soruce.

tial) expressed as [18]:

$$V_{pseudo} = \frac{4qV_0^2 r^6}{m\omega^2 r_0^8} \tag{6.2}$$

where V_0 is the RF voltage amplitude, r_0 is the inner radius of the octupole, r is the radial position of the clusters, q and m are charge and mass of the clusters respectively, and ω is the RF angular frequency. This equation contains the relevant parameters to determine the stability conditions for a given ion trajectory, and to define a mass range for the particles which are transmitted through the octupole. The RF frequency has to be tuned in order to maximize the ion throughput for a specific mass. The DC voltage superimposed, which acts by rigidly shifting the effective pseudopotential, is used to maximize the transmittance of the octupole guide for clusters with a given electrical polarity.

The clusters that leave the octupole are collected by a single pinhole electrode (entrance lens), which is used to collimate the beam. The collimated beam is then transported by a set of modified einzel lenses (fig. 6.8). A typical einzel lens consists of three cylindrical electrodes in series along the beam axis, in which the first and third electrodes are grounded, while the central one is held at an appropriate potential in such a way to focus the particle beam [19]. However, in our setup the three elements are kept at three different potentials. This changes the two focal point of the lens, in a similar way to what obtained for conventional optical lenses with different curvatures at the two sides, and

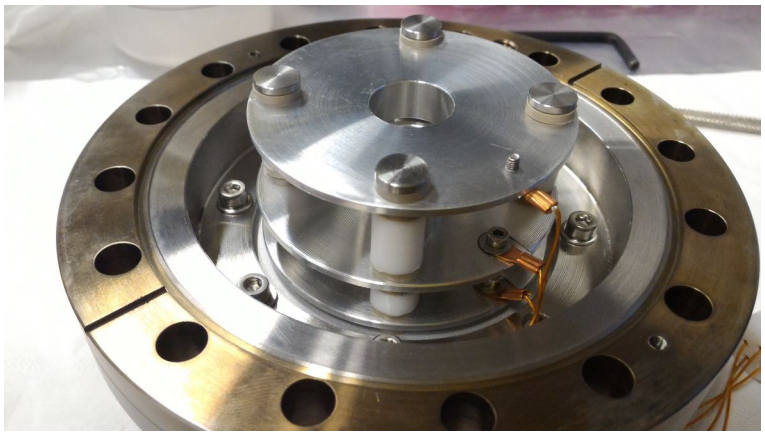

Figure 6.8: Photo of one of the einzel lenses of the cluster source.

cause a kinetic energy exchange with the beam.

6.1.3 Charge separation and mass selection

The cluster produced by means of laser ablation can be either negatively or positively charged, as well as neutral. A first charge selection is due to the DC voltage applied to the octupole, which changes the transmittance for oppositely charged clusters. On the other hand, electrostatic lenses are not charge discriminating. Moreover, neutral and axially collimated clusters are unperturbed by the ion guides. For these reasons, before the final mass selection, which is performed by a high resolution quadrupole mass spectrometer (QMS) on the basis of the mass-to-charge ratio (m/z), the clusters have to be separated according to their electrical polarity.

After leaving the second section, the cluster enter the bending chamber, shown if fig. 6.9, where an electrostatic bending quadrupole deflects the charged particles depending on their charge. The bender (fig. 6.10) consists of four quarter cylindrical electrodes, alternatively polarized with static $\pm$ voltages. The electrodes are parallel to the z axis and perpendicular to the cluster beam. The bender separates charged clusters from neutral ones, allowing the neutral particles to propagate along a straight line parallel to the laser path, while the ions with the selected polarity are deflected towards the quadrupole mass spectrometer, where the final mass selection takes place. By combining ease of operation, high selectivity, and good transmission, electrostatic quadrupole deflectors are the ideal candidate for our purposes.

In the case of a perfect hyperbolic field and of an infinitely thin beam propagating along the z axis, it can be proved that particles with charge e and kinetic

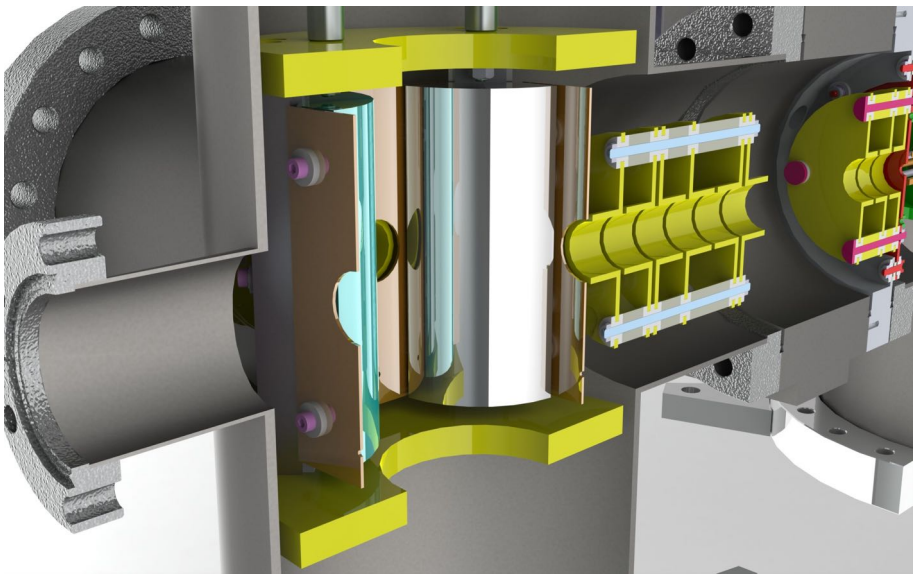

Figure 6.9: Schematical cross section of the bender chamber.

Figure 6.10: Photo of the electrostatic bender used in the mass selected cluster source at the Surface Science Laboratory.

energy $E_{kin} = eU$ are exactly deviated by 90° in opposite directions, depending on the sign of their charge [20]. We can approximate a hyperbolic field using cylindrical electrodes, provided the rod radius, r, and the distance from the center of the bender to the nearest point of any rod, r_0, satisfy the relation $r = 1.15r_0$ [21]. For this reason, the cylindrical electrodes in our design are set tangential to an ideal inscribed cylinder of radius 0.87 times the radius of the rods.

In order to minimize the beam divergence, thus maximizing the transmission inside the bender, two sets of electrostatic lenses are placed before and after the bender plates, for focussing the incoming beam inside the octupole and refocusing the outgoing beam after charge discrimination.

To date, the cluster source in the Surface Science Laboratory is fully operational up to this point, while the fourth, and final, stage including the QMS used for mass selection is still in progress.

Figure 6.11: Photo of the 16000 a.m.u. Extrel QMS which will be installed in the cluster source.

Particles coming out from the exit lens of the bender stage will be collected from the entrance lens of the QMS (see fig. 6.11), which will act as a mass filter by enabling only particle with a specific mass-to-charge ration to pass. In a typical QMS, the potential on the rods is the superposition of a DC potential U and an RF potential $V\cos(\omega t)$. Ideally, the rods are hyperbolic. Cylindrical rods with a specific ratio of rod diameter-to-spacing provide an adequate approximation to hyperbolas. The equations of motion for a charged particle inside the

QMS take the form of Mathieu's equations, as described elsewhere [22]. If we define the z-axis to be parallel to the direction of motion, it can be shown that a QMS acts like a high pass mass filter in the x-z plane and as a low pass mass filter in the y-z plane [23]. By properly selecting U and V, it is therefore possible to operate the QMS as a narrow band pass filter, with a resolution which can easily reach the atomic mass unit (a.m.u). This is related to the fact that, given a certain U and V potentials, only the particles having a certain mass-to-charge-ratio will give a stable solution to the Mathieu's equations, meaning that they will follow a non-diverging trajectory inside the QMS. Particles with a different charge-to-mass ratio will instead give a divergent solution to equation of motion, and will therefore crash against the QMS rods [23]. Our QMS, a state of the art Extrel 150QC RF-DC QMS, will select cluster with mass in the range 1-16000 a.m.u. This means that, for example, we will be able to produce clusters containing up to 81 Au atoms, 273 Ni atoms, or 1332 C atoms.

A final set of einzel lenses will be used to collect the particles after the QMS and focus them on the deposition metal substrate. Soft landing conditions will be achieved by applying a proper retarding potential to the deposition substrate, in order to reduce the cluster energy below 1 eV/atom, thus minimizing the possibility of damaging the cluster upon collision with the substrate. The deposition current will be monitored on the substrate by means of a high sensitivity Keithley picometer. We expect the cluster current to vary, after mass selection, between few tens and few hundreds of pA, depending on the composition and mass of the clusters. To understand how this is related to the deposition rate we can assume a mean cluster current of 200 pA that corresponds, for singularly ionized particles, to a deposition rate of about 10^9 cluster/s, with a 1 mm^2 beam section. Given that the typical metal atomic is about $2 \cdot 10^{13}$ atoms/mm^2, this implies that, to obtain the equivalent of 1 ML of atoms for a 10 atoms cluster, the expected deposition time is about $2 \cdot 10^3$ s, or, in other words, about half an hour.

6.1.4 Differential pumping system

In order to overcome a pressure difference of more than 10 orders of magnitudes between the expansion zone of the cluster source and the final depostion stage, a differential pumping system has to be used. The first chamber, which directly communicate with the expansion zone is pumped by an Alcatel Roots Pump with a maximum pumping speed of 1500 m^3/h. The base pressure of the first chamber is below 10^{-4} mbar and increase up to 10^{-1} mbar during operation, when the laser is switched on and the He flux is injected through

the piezoelectric valve. The second stage (octupole chamber), which is connected to the first chamber by means of the small skimmer aperture only, is pumped by a Pfeiffer turbomolecular pump pre-pumped by a scroll pump. The base pressure in this chamber is of the order of 10^{-7} mbar, and increases up to 10^{-3} during operation. The second and third stages are separated by a gate valve and communicate via the small pinhole of the entrance lens. The latter is pumped by a turbomolecular pump pre-pumped by a diaphragm pump. When the gate vale is closed, an thus the third stage in isolated from the rest of the machine, the base pressure is of the order of 10^{-8} mbar, while during operation it increases to 10^{-5} mbar. The final stage, including the QMS and the deposition chamber, will also be pumped by a turbomolecular pump. Moreover, this last stage will be backed in order to have UHV conditions. During operation we expect the pressure to increase up to 10^{-6} mbar.

6.2 Outlook and perspectives

To date, the cluster source at the Surface Science Laboratory is fully functional up to the bender stage (see fig. 6.12). In particular, the differential pumping system has been stress tested and a leak test was performed in all the three stages. The pulsed piezoelectric vale and the hypocycloidal motion system has been installed and tested in vacuum. The laser has been also installed, aligned, and focused inside the vacuum chamber. Moreover ablation tests have been successfully conducted. We are currently working on the calibration of all the potentials applied to the ion guides, which, at the moment, include 21 electrostatic lens elements and the octupole. A proper calibration of the cluster guide system is crucial in order to maximize the transmittance of the system, or, in other words, the cluster current.

The short term targets are:

- Completing the design and set up of the last stage. At present we are designing the camber that includes the support for the QMS and the last lenses. This chamber will have to be mounted normal to the cluster beam, on the right or left side of the bender stage indifferently. Moreover it will include a telescopic part in order to be able to get closer to the deposition substrate at will.

- Installing the QMS stage and starting the first trial cluster deposition. We will start from a relatively cheap Ni target in order to find the optimal parameters for the last stages.

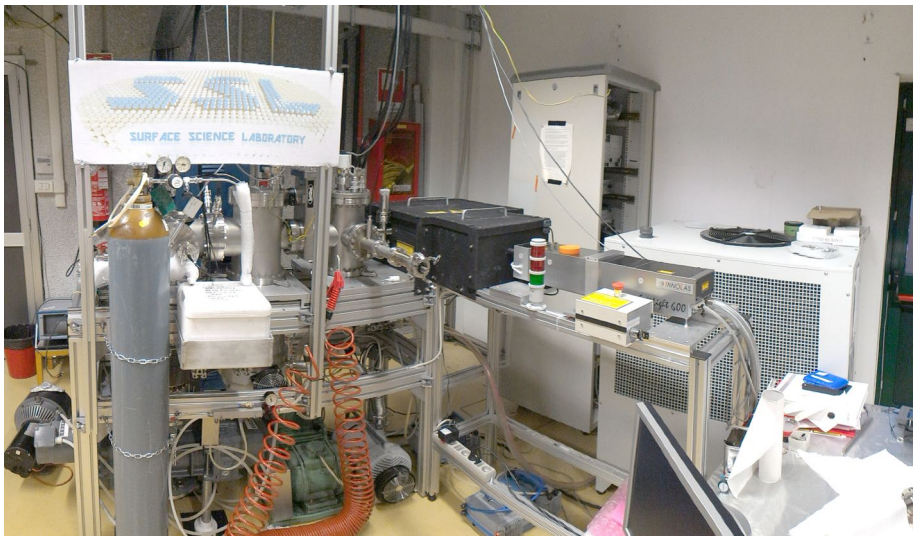

Figure 6.12: Photo of the mass selected cluster source at the Surface Science Laboratory.

Besides that, we are have planned some long term targets that include:

- Moving the cluster source from the Surface Science Laboratory to the SuperESCA beamline of the Elettra synchrotron. This will allow *in situ* analysis of the deposited clusters wit stat of the art synchrotron radiation techniques. This opportunity, which is unique in the field of surface sciences, will open new exciting possibilities for the fine characterization of cluster properties.
- Starting actual experiments on mass selected clusters. Possible experiments will include the templated cluster growth on corrugated graphene or *h*-BN for characterization and catalysis application.

Bibliography

[1] Michel Che and Carroll O Bennett. *The influence of particle size on the catalytic properties of supported metals.*, volume 36. Academic Press, 1989.

[2] W. A. De Heer. The physics of simple metal clusters: experimental aspects and simple models. *Reviews of Modern Physics*, **65**(3):611, 1993.

[3] L. V. Nosova, M. V. Stenin, Y. N. Nogin, and Y. A. Ryndin. EXAFS and XPS studies of the influence of metal particle size, nature of support and H 2 and CO adsorption on the structure and electronic properties of palladium. *Applied Surface Science*, **55**(1):43–48, 1992.

[4] E. C. Tyo and S. Vajda. Catalysis by clusters with precise numbers of atoms. *Nature Nanotechnology*, **10**(7):577–588, 2015.

[5] G. Seifert. Nanomaterials: nanocluster magic. *Nature Materials*, **3**(2):77–78, 2004.

[6] V. F. Puntes, P. Gorostiza, D. M. Aruguete, N. G. Bastus, and A. P. Alivisatos. Collective behaviour in two-dimensional cobalt nanoparticle assemblies observed by magnetic force microscopy. *Nature Materials*, **3**(4):263–268, 2004.

[7] R. E. Smalley. Laser Studies of Metal Cluster Beams. *Laser Chem.*, **2**:167–184, 1983.

[8] S. Maruyama, L R. Anderson, and R. E. Smalley. Direct injection supersonic cluster beam source for FT-ICR studies of clusters. *Review of Scientific Instruments*, **61**(12):3686–3693, 1990.

[9] U. Heiz, F. Vanolli, L. Trento, and W. D. Schneider. Chemical reactivity of size-selected supported clusters: An experimental setup. *Review of Scientific Instruments*, **68**(5):1986–1994, 1997.

[10] M. A. Röttgen, K. Judai, J.-M. Antonietti, U. Heiz, S. Rauschenbach, and K. Kern. Conical octopole ion guide: Design, focusing, and its application to the deposition of low energetic clusters. *Review of Scientific Instruments*, **77**(1):013302, 2006.

[11] U. Heiz, F. Vanolli, A. Sanchez, and W. D. Schneider. Size-dependent molecular dissociation on mass-selected, supported metal clusters. *Journal of the American Chemical Society*, **120**(37):9668–9671, 1998.

[12] U. Heiz, A. Sanchez, S. Abbet, and W. D. Schneider. Catalytic oxidation of carbon monoxide on monodispersed platinum clusters: each atom counts. *Journal of the American Chemical Society*, **121**(13):3214–3217, 1999.

[13] H. Häkkinen, S. Abbet, A. Sanchez, U. Heiz, and U. Landman. Structural, electronic, and impurity-doping effects in nanoscale chemistry: supported gold nanoclusters. *Angewandte Chemie International Edition*, **42**(11):1297–1300, 2003.

[14] B. Yoon, H. Häkkinen, U. Landman, A. S. Wörz, J. M. Antonietti, S. Abbet, K. Judai, and U. Heiz. Charging effects on bonding and catalyzed oxidation of CO on Au_8 clusters on MgO. *Science*, **307**(5708):403–407, 2005.

[15] M. Yamashita and J. B. Fenn. Electrospray ion source. Another variation on the free-jet theme. *The Journal of Physical Chemistry*, **88**(20):4451–4459, 1984.

[16] M. Schmidt, R. Kusche, B. von Issendorff, and H. Haberland. Irregular variations in the melting point of size-selected atomic clusters. *Nature*, **393**(6682):238–240, 1998.

[17] T. G Dietz, M. A. Duncan, D. E. Powers, and R. E. Smalley. Laser production of supersonic metal cluster beams. *The Journal of Chemical Physics*, **74**(11):6511–6512, 1981.

[18] Y. Huang, S. Guan, H. S. Kim, and A. G. Marshall. Ion transport through a strong magnetic field gradient by rf-only octupole ion guides. *International Journal of Mass Spectrometry and Ion Processes*, **152**(2):121–133, 1996.

[19] A. Adams and F. H. Read. Electrostatic cylinder lenses II: Three element einzel lenses. *Journal of Physics E: Scientific Instruments*, **5**(2):150, 1972.

[20] H. D. Zeman. Deflection of an ion beam in the two-dimensional electrostatic quadrupole field. *Review of Scientific Instruments*, **48**(8):1079–1085, 1977.

[21] A. P. Banford. *The transport of charged particle beams*. Spon London, 1966.

[22] M. Abramowitz and I. A. Stegun. Handbook of mathematical functions. *Applied Mathematics Series*, **55**:62, 1966.

[23] P. E. Miller and M. B. Denton. The quadrupole mass filter: basic operating concepts. *Journal of Chemical Education*, **63**(7):617, 1986.

Publications

1. **L. Omiciuolo**, E. R. Hernandéz, E. Miniussi, F. Orlando, P. Lacovig, S. Lizzit, T. O. Menteş, A. Locatelli, R. Larciprete, M. Bianchi, S. Ulstrup, Ph. Hofmann, D. Alfè, and A. Baraldi. Bottom-up approach for the low-cost synthesis of graphene-alumina nanosheet interfaces using bimetallic alloys. *Nature Communications* **5**, 5062 (2014)

2. F. Orlando, P. Lacovig, **L. Omiciuolo**, N. G. Apostol, R. Larciprete, A. Baraldi, and S. Lizzit. Epitaxial Growth of a Single-Domain Hexagonal Boron Nitride Monolayer. *ACS Nano* **8**, 12063 (2014).

3. F. Presel, N. Jabeen, M. Pozzo, D. Curcio, **L. Omiciuolo**, P. Lacovig, S. Lizzit, D. Alfè, and A. Baraldi. Unravelling the roles of surface chemical composition and geometry for the graphene-metal interaction through C1s core-level spectroscopy. *Carbon* **93**, 187 (2015).

4. R. Larciprete, P. Lacovig, F. Orlando, M. Dalmiglio, **L. Omiciuolo**, A. Baraldi, and S. Lizzit. Chemical gating of epitaxial graphene through ultrathin oxide layers. *Nanoscale* **7**, 12650 (2015).

5. D. Curcio*, **L. Omiciuolo***, M. Pozzo, P. Lacovig, S. Lizzit, N. Jabeen, L. Petaccia, D. Alfè, and A. Baraldi. Molecular lifting, twisting, and curling during metal-assisted polycyclic hydrocarbon dehydrogenation. *The Journal of the American Chemical Society* , (2016). DOI: http://dx.doi.org/10.1021/jacs.5b12504.

   * D. Curcio and L. Omiciuolo contributed equally to this work.

Submitted works:

- H. Tetlow, J. P. de Boer, I. J. Ford, D. D. Vvedensky, D. Curcio, **L. Omiciuolo**, S. Lizzit, A. Baraldi, and L. Kantorovich. Ethylene decomposition on Ir(111): Initial path to graphene formation. *submitted*.

Other publications:

- **L. Omiciuolo**, E. R. Hernandéz, E. Miniussi, F. Orlando, P. Lacovig, S. Lizzit, T. O. Menteş, A. Locatelli, R. Larciprete, M. Bianchi, S. Ulstrup, Ph. Hofmann, D. Alfè, and A. Baraldi. Bottom-up approach for the low-cost synthesis of graphene-alumina nanosheet interfaces using bimetallic alloys. Elettra Highlights 2013-2014, 54.
- R. Larciprete, P. Lacovig, F. Orlando, M. Dalmiglio, **L. Omiciuolo**, A. Baraldi, and S. Lizzit. Chemical gating of epitaxial graphene through ultrathin oxide layers. Elettra Highlights 2014-2015, 26.

List of the Acronyms

AES	Auger Electron Spectroscopy
ARPES	Angle Resolved PhotoEmission Spectroscopy
BE	Binding Energy
CLS	Core Level Shift
CVD	Chemical Vapor Deposition
DFT	Density Functional Theory
D-S	Doniach-Šunjic
EDAC	Electron Diffraction in Atomic Clusters
EDC	Energy Dispersion Curve
EELS	Electron Energy Loss Spectroscopy
ESCA	Electron Spectroscopy for Chemical Analysis
EXAFS	Extended X-ray Absorption Fine Structure
HOPG	Highly Oriented Pyrolitic Graphite
HR-XPS	High Resolution XPS
LEED	Low Energy Electron Diffraction
LEEM	Low Energy Electron Microscopy
MDC	Momentum Dispersion Curve
NEB	Nudge Elastic Band
NEXAFS	Near Edge X-ray Absorption Fine Structure
QMS	Quadrupole Mass Spectrometer
RF	Radio Frequency
RGA	Residual Gas Analyzer
SCLS	Surface Core Level Shift
SPA-LEED	Spot Profile Analysis LEED
STM	Scanning Tunneling Microscopy

TM	Transition Metal
TPD	Temperature Programmed Desorption
TPG	Temperature Programmed Growth
TP-XPS	Temperature Programmed XPS
VB	Valence Band
UHV	Ultra-High Vacuum
XAS	X-Ray Absorption Spectroscopy
XPD	X-ray Photoelectron Diffraction
XPS	X-ray Photoelectron Spectroscopy

Acknowledgements

This PhD thesis puts and end to an incredible scientific and human experience that started long ago, during the master degree at the University. Therefore, I must spend few words for all the people that have contributed to this period of my life.

My first heartfelt thanks goes to my supervisor Alessandro. He picked me up four years ago, when I was an undergraduate student, and guided me to the completion of this PhD project. He has been an excellent boss, always stimulating me to do my best, and, most importantly, a good friend. I profoundly respect him both as a scientist and as human being, and I owe him most of my scientific growth during these years. Thank you for everything.

I am also deeply thankful to my co-supervisor Silvano, for all the useful teachings, for the stimulating discussions, and for the time spent together. Thank you so much Silvano.

Furthermore, I would like to thank all the current and former members of the Surface Science Laboratory and of the SuperESCA beamline that have contributed making this experience beautiful. Thank you Andrea, Carlo, Crisitian, Dario, Elisa, Elisabetta, Fabrizio, Francesco, Harsh, Luca, Matteo, Naila, and Paolo.

A special thanks goes to Davide for all the time together in the lab, for all the fruitful discussions, and for being a good friend. We spent so much time working together that I can hardly figure my future professional life without him.

A further thanks goes to all the people with whom I have collaborated during my research activity, including Rosanna, the group of Prof. Dario Alfè, the Nanospectroscopy beamline group, the BaDElPh beamline staff, the SGM3 beamline scientists, and Eugenio from the sample preparation laboratory, for the essential support in the set up of the cluster source.

Finally, I would like to thank my family for their love, patience, and care during these years. I would have never reached this important goal without their help.

And Sara, for her love, for the unconditional support in every decision I have made, and because I am sure that, whatever challenges await us, we will face them together.